NTNU – Trondheim
Norwegian University of
Science and Technology

Bayesian Inversion of Time-lapse Seismic Data using Bimodal Prior Models

Ingvild Amaliksen

Master of Science in Physics and Mathematics
Submission date: February 2014
Supervisor: Karl Henning Omre, MATH

Norwegian University of Science and Technology
Department of Mathematical Sciences

Preface

This study has been carried out at the Department of Mathematical Sciences at the Norwegian University of Science and Technology, Trondheim, Norway, during the fall of 2013. The thesis concludes the 5-year Industrial Mathematics program at NTNU and leads to the degree Master of Science.

I would like to express my sincere gratitude to my supervisor Professor Henning Omre for all the support he has given me both on my master thesis and on my project. His inputs and feedback have ensured my progress and his knowledge and interest in the topic at study have been a source of constant motivation. Thank you for meeting the students with patience and a big smile and for always having a pencil and a blank piece of paper ready for us when we need some guidance.

I also want to thank Harry Brandsen at Statoil for providing me with well log data which was used in the synthetic study. Finally, I would like to thank Geir for letting me discuss my project with him, for proofreading my thesis and for making both the good and the hard days better.

Ingvild Amaliksen
January 2014
Trondheim

Abstract

The objective of the current study is to make inference about reservoir properties from seismic reflection data. The inversion problem is cast in a Bayesian framework, and we compare and contrast three prior model settings; a Gaussian prior, a mixture Gaussian prior and a generalized Gaussian prior. A Gauss-linear likelihood model is developed and by the convenient properties of the family of Gaussian distributions, we obtain the explicit expressions for the posterior models. The posterior models define computationally efficient inversion methods that can be used to make predictions of the reservoir variables while providing an uncertainty assessment. The inversion methodologies are tested on synthetic seismic data with respect to porosity, water saturation, and change in water saturation between two time steps. The mixture Gaussian and generalized Gaussian posterior models show encouraging results under realistic signal-noise ratios.

Sammendrag

Målet med denne studien er å bruke Bayesiansk inversjon til å predikere reservoaregenskaper fra seismiske refleksjonsdata. Vi introduserer en lineær likelihood modell og evaluerer egenskapene til posteriori fordelingen under henholdsvis en Gaussisk, en mix Gaussisk og en generalisert Gaussisk priormodell. Egenskapene til den Gaussiske familien av fordelinger sikrer at vi kan finne eksplisitte utrykk for posteriorimodellene. Posteriorimodellene definerer raske inversjonmetodikker som kan brukes til å predikere reservoaregenskapene og til å tallfeste usikkerheten i dem. Vi tester metodikken på syntetiske seismiske data hvor vi predikerer porositet, vannmetning og endring i vannmetning mellom to tidssteg. Inversjonsresultatene for den mix Gaussiske og generaliserte Gaussiske modellen gir oppmuntrende resultater, selv under realistiske signal-støyforhold.

Contents

Chapter 1

Introduction

Reservoir characterization and modeling are important tools in the development and production of oil and gas from hydrocarbon reservoirs. The purpose of reservoir modeling is to map the reservoir, and predict reservoir behavior during production. A robust and accurate reservoir model will provide crucial information that may increase recovery and extend production. The average global hydrocarbon recovery rate is approximately 30%, which is what can be produced without introducing expensive enhanced oil recovery methods. In the past, production from oil fields was normally completed without application of enhanced oil recovery methods, as oil could be produced at a lower cost elsewhere. However, during the last decades the world's energy demand has increased to a level where the traditional cheaper methods are no longer sufficient, and the oil price has risen from a level of 20 USD/BBL in the nineties to its current level at around 100 USD/BBL. As a consequence, investment in enhanced oil recovery is crucial. With the current high oil price, the value of every extra percent recovered from the Norwegian Shelf amounts to approximately 200 billion NOK. It is therefore a good investment to ensure higher recovery rates by collecting and utilizing as much information as possible from the reservoirs prior to and during production.

The input in a reservoir model includes the structural details of the container and the reservoir and rock properties which include porosity, permeability, saturations and pressure. The reservoir in an oil field is located deep beneath the surface of the Earth. The only available samples and measurements are log and core data taken at certain locations which may, or may not, be representative for the whole field. We therefore have to rely on indirect measurements such as seismic data. This is particularly important in offshore areas where wells are extremely expensive while seismic data are relatively easy to acquire. Subsurface geometries are resolvable from seismic data, and since the rock properties determine the velocity of the reflected P- and S-waves, the seismic survey will indirectly give information about the properties and the constituents of the reservoir rock.

Recent developments in acquisition and processing techniques have drastically improved the quality of seismic data. Seismic surveys are now playing an increasingly important role in reservoir management as it is possible to extract quantitative rock and fluid properties from the reflection data. The introduction of time-lapse seismic has introduced an option for the industry to investigate changes in water saturation and pressure over time in producing fields. The drainage efficiency and the effect of injected fluids into the reservoir can therefore be evaluated while production is still ongoing. However, interpretation of rock properties from seismic data is still associated with uncertainty since the recorded effect may not have a unique cause. Variables like porosity, compaction, pressure, water saturation, clay content and lithology are all important factors, and calibration to adjacent wells is very important to optimize the robustness of any predictions.

The problem at hand can be formulated as an inverse problem where we want to make inference about the cause of an effect based on observations of the effect only. Because the observations are subject to uncertainty due to random and systematic errors, the problem should be evaluated in a probabilistic setting.

During the last decade, innovative new seismic inversion techniques have been presented. In Landrø (2001), expressions for the change in AVO data as a function of the change in saturation and pressure is developed. A follow-up to this article is given in Landrø (2002), where a deterministic uncertainty analysis is presented based on the Delta method. In Landrø (2002) it is assumed that all the variables are independent, which is a major simplification.

Another approach is to evaluate the inverse problem in a Bayesian setting. This provides a framework where we can impose a correlation structure and incorporate prior knowledge about the reservoir variables. In Bachrach (2006) an MCMC algorithm is used to evaluate the posterior model for the water saturation and porosity. A Bayesian approach for saturation-pressure discrimination is also studied in Veire et al. (2006) and Veire et al. (2007) where a Gauss-linear likelihood together with a Gaussian prior gives an analytically tractable solution to the inverse problem. The most thoughtful study of the subject is perhaps found in Grana (2013) which introduces several methodologies for seismic reservoir characterization.

In the current thesis the inverse problem is cast in a Bayesian framework. The objective is to obtain the posterior distribution for the reservoir variables from the time-lapse AVO data. The current thesis draws inspiration from the prior model setup in Grana (2013), but we want to avoid using sampling methods when evaluating the posterior model, which restrains the form of our likelihood model. Since the seismic data sets are very large, the computational efficiency of the methodology is crucial. We therefore seek prior-likelihood model couples that will keep the posterior analytically tractable. We evaluate the inverse problem with a Gaussian, a mixture Gaussian and a generalized Gaussian prior. The inspiration for modeling the problem with the respective priors comes from Grana et al. (2012) and Rimstad and Omre (2012). In order to keep the posterior analytically tractable we impose a Gauss-linear likelihood inspired by Buland and Omre (2003), where well known rock physics models are linearized in order to find a linear expression for the forward model. We then use the convenient mathematical properties of the Gaussian assumption to obtain the posterior models.

The thesis proceeds as follows: In Chapter 2 the background theory needed to develop the forward model between the reservoir variables and the seismic variables is presented. In Chapter 3 the linear likelihood model and the three prior models are derived, and we develop the corresponding posterior models. In Chapter 4, the methodology is tested and evaluated on a synthetic data set and in Chapter 5 we draw conclusions and make some recommendations for further work.

Chapter 2
Theory

In this chapter the background theory used to develop the forward model between the reservoir variables and the seismic variables is presented. This includes a summary of rock-fluid physics and geophysics (Section 2.1-2.2) and a brief introduction to Bayesian inversion (Section 2.3-2.4).
All attributes considered in Section 2.1 are pseudo point processes where the property is defined around a small volume surrounding the point. The attribute is dependent on the horizontal direction x, the vertical direction τ and time of observation t.

2.1 Rock and fluid physics

A wave is a disturbance that travels through a medium by inducing local changes in stress and strain. Inside the medium, the wave actuate either a compressional or a shear force. These two types of waves are called P-waves and S-waves respectively. The P-wave travels through all types of material since any media is subject to compression. The S-wave on the other hand depends upon a resistance to shear force, which is not present in liquids and gasses. The propagation speed of a wave is determined by the density and elasticity of the medium. The elastic moduli is given by the bulk modulus k which measure resistance to uniform compression, and shear modulus g which describe responds to shearing forces. The velocities in a saturated, porous medium are expressed as

$$v_p = \sqrt{\frac{k_s + \frac{4}{3}g_s}{\rho}}, \tag{2.1}$$

$$v_s = \sqrt{\frac{g_s}{\rho}}. \tag{2.2}$$

In this expression k_s and g_s denote the saturated bulk and shear modulus

and ρ denotes bulk density. If the medium consists of a porous matrix where the voids are filled with brine and oil, the density is found by a weighted average of the porosity ϕ and water saturation s_w,

$$\rho = \phi\left(\rho_w s_w + \rho_o(1 - s_w)\right) + (1 - \phi)\rho_m, \tag{2.3}$$

where ρ_w is the density of brine and ρ_o is the density of oil. From this expression it is apparent that the porosity gives the fraction of fluid in the rock, and the water saturation gives the fluid composition. A simplistic display of the composites in a water saturated reservoir is shown in Figure 2.1.

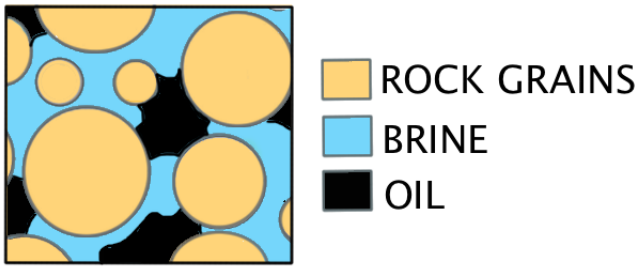

Figure 2.1: Composition in a water saturated reservoir

In order to estimate the wave velocities we need to quantify the saturated moduli. This is often difficult in practice. The pore space of a rock is typically occupied by several fluid phases and the moduli depend on the geometric details, the volume fractions and the individual elastic moduli of the constituents. The estimation of elastic properties are at study in rock physics model theory, which in Avseth et al. (2010, p. 32) is described as "continuum-mechanics approximations of the elastic, viscoelastic and porelastic properties of the rock". The assumptions and constraints of the models presented in the following are found in Mavko et al. (2003) and Avseth et al. (2010).

An expression for the saturated bulk and shear modulus is provided by the Gassmann model, which relates the bulk modulus of a rock to its matrix and fluid properties by

$$k_s = k_d + \frac{\left(1 - \frac{k_d}{k_m}\right)^2}{\frac{1-\phi}{k_m} + \frac{\phi}{k_f} - \frac{k_d}{k_m^2}}. \tag{2.4}$$

Here, k_d denotes the bulk modulus of the dry porous rock, k_m is the is the bulk modulus of the solid mineral grain and k_f is the bulk modulus of the pore fluid. In the Gassmann model it is assumed that the bulk modulus is sensitive to pore fluid composition, while the shear modulus is not. The saturated shear modulus g_s is in other words unchanged during fluid substitution

$$g_s = g_d, \tag{2.5}$$

where g_d is the dry shear modulus. This is one of the fundamental concepts in the application of the Gassmann model. From Expression 2.4 we deduce that the saturated media is stiffer under compression compared to the dry media. This is because the addition of pressure in the pore fluid resists volumetric strain.

In order to find the saturated moduli from the Gassmann model we need to quantify k_f, k_d, k_m and g_d. If we know the constituents and the corresponding volume fractions in a reservoir rock, then according to Mavko et al. (2003), we can find an upper and lower bound for any effective modulus by noting that it is impossible to have a mixture of constitutes that is elastically stiffer than the arithmetic average of the constituent moduli, and likewise, that it is impossible to have a mixture of constitutes that is elastically softer than the harmonic average of the constituent moduli. These two principles define the Voigt–Reuss–Hill bounds for an arbitrary modulus m.

Voigt upper bound:

$$m^v = \sum_{i=1}^{n} \alpha_i m_i. \tag{2.6}$$

Reuss lower bound:

$$(m^r)^{-1} = \sum_{i=1}^{n} \alpha_i m_i^{-1}. \tag{2.7}$$

Voigt–Reuss–Hill average :

$$m^{vrh} = \frac{1}{2}(m^v + m^r). \tag{2.8}$$

Here, α_i is the volume fraction of the i'th constituent and m_i is the modulus of the i'th constituent.

If the reservoir is only filled with brine and oil, the Reuss lower bound can be used to approximate k_f in the Gassmann model as described in Dvorkin et al. (2007)

$$k_f^{-1} = s_w k_w^{-1} + (1 - s_w)k_o^{-1}, \tag{2.9}$$

were k_w and k_o is the bulk modulus for water and oil respectively.

In this study we are concerned with a reservoir that consists of well-sorted clean sand which we assume act as a porous isotropic elastic medium. At the time of deposition, the porosity of well-sorted sand is approximately 40%. This value is often referred to as the critical porosity of the sediments. A model for the elastic moduli of dry, well sorted sand at critical porosity is given by the Hertz–Mindlin model for unconsolidated sediments,

$$k_0 = \left(\frac{q^2(1-\phi_0)^2 g_m^2 p}{18\pi^2(1-\nu)^2} \right)^n, \tag{2.10}$$

$$g_0 = \frac{5-4\nu}{5(2-\nu)} \left(\frac{3q^2(1-\phi_0)^2 g_m^2 p}{2\pi^2(1-\nu)^2} \right)^n. \tag{2.11}$$

Here ϕ_0 is the critical porosity, g_m is shear modulus of the mineral, p is the effective pressure, q is the average number of contacts per sphere and ν is the ratio between the horizontal and vertical strains (Poisson ratio) which is calculated from

$$\nu = \frac{3k_m - 2g_m}{2(3k_m - g_m)}. \tag{2.12}$$

The coefficient n in the Hertz–Mindlin model is dependent on the types of sediments in the reservoir. It is usually set to a constant in the range $(\frac{1}{5.6}, \frac{1}{3})$. We use $\frac{1}{5}$ as suggested in Veire et al. (2006).

During millions of years with gradually deeper burial, the sand will compact and the pore space will be filled with cement, which decreases the porosity from ϕ_0 to ϕ. The compaction of the sand will also increase the effective elastic moduli of the sandstone. The principle is illustrated in Figure 2.2. In order to calculate the new dry bulk and shear moduli we use the friable-sand model presented in Avseth et al. (2010). At porosity ϕ the fraction of the

original packing is $\frac{\phi}{\phi_0}$. The dry bulk and shear moduli are then,

$$k_d = \left(\frac{\frac{\phi}{\phi_0}}{k_0 + \frac{4}{3}g_0} + \frac{1 - \frac{\phi}{\phi_0}}{k_m + \frac{4}{3}g_0} \right)^{-1} - \frac{4}{3}g_0, \tag{2.13}$$

$$g_d = \left(\frac{\frac{\phi}{\phi_0}}{g_0 + \zeta} + \frac{1 - \frac{\phi}{\phi_0}}{g_m + \zeta} \right)^{-1} - \zeta, \tag{2.14}$$

$$\zeta = \frac{g_0}{6} \left(\frac{9k_0 - 8g_0}{k_0 + 2g_0} \right). \tag{2.15}$$

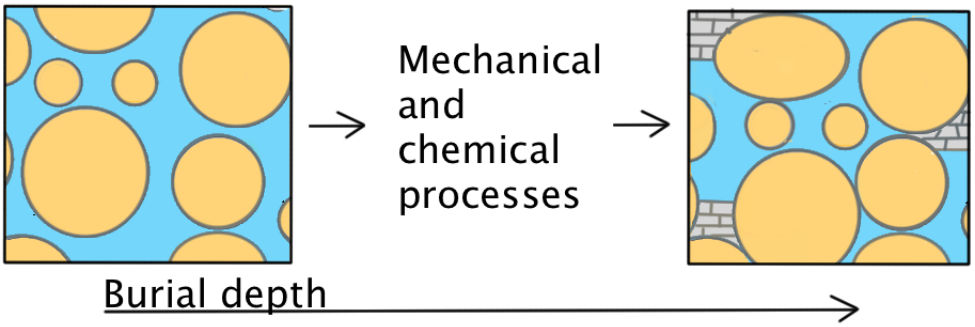

Figure 2.2: Reduction in porosity caused by burial and cementation

Now, the only unknowns in the Gassmann model are the mineral moduli k_m and g_m. The Voigt–Reuss–Hill average in Expression 2.8 provides a simple way to estimate these. The fraction of solid mineral in the rock is given by $1 - \phi$. If c denotes the percentage of clay in the rock, then for a simple mineralogy of sand and shale the fractions of these two components are $\frac{1-c}{1-\phi}$ and $\frac{c}{1-\phi}$ in the solid mineral. Expressions 2.8 is then expressed as

$$k_m = \frac{1}{2} \left(\frac{c}{1-\phi} k_c + \frac{1-c}{1-\phi} k_{sand} + \left(\frac{c}{1-\phi} \frac{1}{k_c} + \frac{1-c}{1-\phi} \frac{1}{k_{sand}} \right)^{-1} \right), \tag{2.16}$$

$$g_m = \frac{1}{2} \left(\frac{c}{1-\phi} g_c + \frac{1-c}{1-\phi} g_{sand} + \left(\frac{c}{1-\phi} \frac{1}{g_c} + \frac{1-c}{1-\phi} \frac{1}{g_{sand}} \right)^{-1} \right), \tag{2.17}$$

where k_c, g_c, k_{sand} and g_{sand} are the moduli of sand and clay, which are assumed to be known.

We divide the reservoir variables discussed in this section into two major groups; static and dynamic variables. Dynamic variables are influenced by movement of fluid in the reservoir and include saturation, fluid bulk modulus, pressure and temperature. These are variables that will change during the course of production. Static variables are not related to movement of fluid in the reservoir and include geological data, shear moduli and porosity.
The variables of interest in this study is the porosity ϕ and the water saturation s_w. We develop the relationships between the reservoir variables ϕ and s_w and the elastic variables v_s, v_p and ρ from the rock and fluid physics models listed in this section. In the current study we make the assumption that the relative change in water saturation is much greater in magnitude than the relative change in the pressure. This simplification will not be valid for all reservoirs, but in this introductory study we omit the pressure since we do not have a pressure profile from the well used in the simulation study. The statistical methodology developed in the following chapter can easily be extended to any rock physics variables at interest.

2.2 Seismic acquisition and processing

The purpose of a seismic survey is to acquire information about the Earths subsurface. In the simplest case, an energy source fires at regular intervals as a vessel moves along a survey line. Energy from the shot is reflected from horizons beneath the sea floor and is detected by hydrophones on the surface. After the shot is recorded, the geophysicist needs to process the data and make it into a readable image of the subsurface. In this process the data is subject to stacking, multiple removal and migration steps. Seismic surveys in the same location acquired at different times can be used to detect changes in the fluid content of the rock formations. This type of survey is known as a time-lapse seismic survey. In Figure 2.3 we display a subsurface horizon together with the corresponding seismic signal and in Figure 2.4 we show a simplistic illustration of marine seismic acquisition.

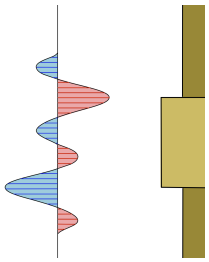

Figure 2.3: Layered model with corresponding seismic response.

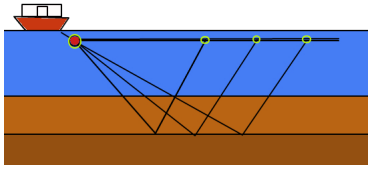

Figure 2.4: A seismic wave pulse is reflected at a horizon below sea bottom and recorded by the hydrophones.

We consider a 1D vertical profile in the τ direction for two seismic surveys collected at times t_0 and t_1. Since the seismic data is given as a discrete set at a given location we discretize the profile into $\boldsymbol{\tau} = (\tau_1, \tau_2, ..., \tau_T)$, such that $\tau_1 < \tau_2 <, \ldots, < \tau_T$. We have seismic observations available for (τ_j, t_k) for $j = 1, \ldots, T$, $k = 0, 1$ which is represented as:

$$\mathbf{d_k} = \begin{bmatrix} d_{k,1} \\ \cdot \\ \cdot \\ d_{k,T} \end{bmatrix} ; \; k = 0, 1.$$

If we also have data available from different offset angles $(\theta_1, \ldots, \theta_m)$ in a

gather, the seismic observation vector is given by

$$\mathbf{d}_{\mathbf{k}}^{\theta} = \begin{bmatrix} d_{k,1}^{\theta} \\ \cdot \\ \cdot \\ d_{k,T\times m}^{\theta} \end{bmatrix}; \; k = 0, 1.$$

Since the mathematical results deduced for the seismic observation vectors are identical at both time increments we will refer to $\{\mathbf{d_k}; k = 0, 1\}$ and $\{\mathbf{d}_{\mathbf{k}}^{\theta}; k = 0, 1\}$, as $\mathbf{d}$ and $\mathbf{d}^{\theta}$ respectively in the following.

2.2.1 Convolution and wavelets

Convolution is a mathematical operation on two functions c and w, which produces a third function that can be interpreted as a modified version of c. In this interpretation w is called the filter. In a seismic experiment the pulse generated from the source is altered in shape as it passes through the underground since the earth causes dispersion. Therefore the signal recorded will be significantly different from the original seismic pulse. To model the original signal we set up a convolution model.
We assume that the attributes are continuous which mean that they are defined for all values in the domain of interest $\mathcal{D}$. The value of a given attribute ξ at an arbitrary point $y \in \mathcal{D}$ is then denoted by $\xi(y)$.
Now, suppose we have an unconvoluted reflectivity sequence $c(\tau, \theta)$ and a localized wavelet $w(u, \theta)$ that act as a filter. The wavelet is allowed to be angle dependent and is assumed to be stationary within a small time window. The total value of a trace at τ is the sum of all possible times within the wavelet,

$$d(\tau, \theta) = \int_{-\infty}^{\infty} w(u, \theta) c(\tau - u, \theta) du + e(\tau, \theta).$$

The seismic signal recorded by the convolution model is represented by

$$d(\tau, \theta) = w(u, \theta) * c(\tau, \theta) + e(\tau, \theta),$$

where $e(\tau, \theta)$ is the error term.
To represent this in a discrete matrix form we write

$$\mathbf{d}^{\theta} = \mathbf{W}\mathbf{c} + \boldsymbol{\epsilon}, \tag{2.18}$$

where $\mathbf{c}$ is the reflectivity signal vector and $\mathbf{W}$ is a block diagonal convolution matrix with diagonal submatrices $\mathbf{w}(\theta_i)$ representing the wavelet for angle θ_i,

$$\mathbf{W} = \begin{bmatrix} \mathbf{w}(\theta_1) & & & \\ & \cdot & & \\ & & \cdot & \\ & & & \cdot \\ & & & & \mathbf{w}(\theta_m) \end{bmatrix}.$$

It is common to use the Ricker wavelet in the seismic convolution model. With its peak and two symmetric side lobes, it bears resemblance to an actual physical seismic wavelet. The Ricker wavelet is defined as the second derivative of a Gaussian function,

$$w(u;\nu) = 2\pi^{\frac{5}{2}}\nu^3(1 - 2\pi^2\nu^2u^2)\exp(-\pi^2\nu^2u^2), \tag{2.19}$$

with ν being the frequency.
A Ricker wavelet with frequency 25 is depicted in Figure 2.5. A real seismic wavelet is time and angle variant and have a more complex shape than the Ricker wavelet. To use a linearized convolution matrix with a discrete Ricker wavelet in the convolution model is therefore simplistic, but still often adequate for modeling.

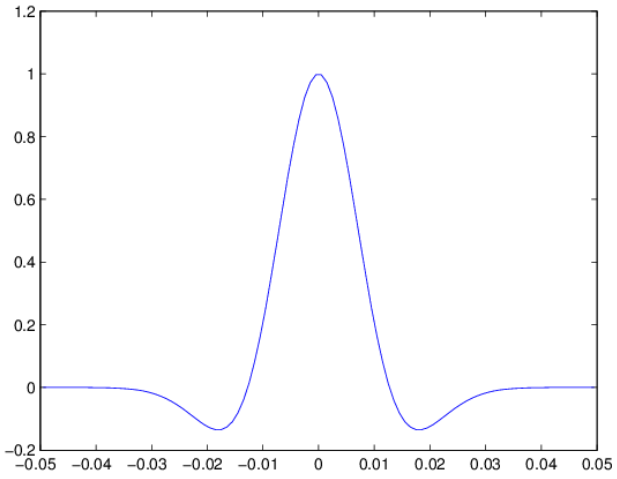

Figure 2.5: Ricker wavelet, $w(u;25)$

2.2.2 Amplitude versus offset (AVO)

AVO analysis is a technique that relates seismic reflection and transmission amplitudes to offset distances. The most important application of AVO is the detection of hydrocarbons and lithology identification. This analysis is based on the fact that seismic amplitudes at the boundaries are affected by the difference in the physical properties above and below the boundary. The Zoeppritz equations is a set of matrix equations which captures the dependence between reflection coefficients, incidence angle and the elastic variables. These equations includes several unknowns and require large computation times. It is therefore often more convenient to work with an approximation to the Zoeppritz equations. In this study the Aki and Richards approximation is used. In Aki and Richards (1980) the reflectivity coefficients are given by

$$c(\tau,\theta) = a_\alpha(\tau,\theta)\frac{\partial}{\partial\tau}\ln v_p(\tau) + a_\beta(\tau,\theta)\frac{\partial}{\partial\tau}\ln v_s(\tau) + a_\rho(\tau,\theta)\frac{\partial}{\partial\tau}\ln\rho(\tau), \quad (2.20)$$

with

$$\begin{aligned} a_\alpha(\tau,\theta) &= \frac{1}{2}\left(1+\tan^2(\theta)\right), \\ a_\beta(\tau,\theta) &= -4\frac{\bar{v}_s(\tau)^2}{\bar{v}_p(\tau)^2}\sin^2(\theta), \\ a_\rho(\tau,\theta) &= \frac{1}{2}\left(1-4\frac{\bar{v}_s(\tau)^2}{\bar{v}_p(\tau)^2}\sin^2(\theta)\right). \end{aligned}$$

Here $\bar{v}_p(\tau)$ and $\bar{v}_s(\tau)$ are defined as local averages of $v_p(\tau)$ and $v_s(\tau)$ in a window along the seismic trace.

Like in Buland and Omre (2003), we will assume that

$$\frac{\bar{v}_s(\tau)}{\bar{v}_p(\tau)} = \frac{1}{2}. \quad (2.21)$$

This is a decent approximation for many sandstone reservoirs.

A discrete version of the continuous function in Expression 2.20 in a time interval and for a set of reflection angels is then

$$\mathbf{c} = \mathbf{ADm}, \tag{2.22}$$

where $\mathbf{D}$ is the difference operator with respect to the τ direction, defined as

$$\mathbf{D} = \begin{bmatrix} 1 & -1 & & & & \\ & 1 & -1 & & & \\ & & . & . & & \\ & & & . & . & \\ & & & & 1 & -1 \end{bmatrix}, \tag{2.23}$$

and

$$\mathbf{A} = \begin{bmatrix} \mathbf{A}_\alpha(\theta_\mathbf{1}) & \mathbf{A}_\beta(\theta_\mathbf{1}) & \mathbf{A}_\rho(\theta_\mathbf{1}) \\ . & . & . \\ . & . & . \\ \mathbf{A}_\alpha(\theta_\mathbf{m}) & \mathbf{A}_\beta(\theta_\mathbf{m}) & \mathbf{A}_\rho(\theta_\mathbf{m}) \end{bmatrix}, \tag{2.24}$$

$$\mathbf{m} = [\ln(\mathbf{v_p}), \ln(\mathbf{v_s}), \ln(\boldsymbol{\rho})]^\mathsf{T}. \tag{2.25}$$

Here $\mathbf{A}_\alpha$, $\mathbf{A}_\beta$ and $\mathbf{A}_\rho$ are diagonal $T \times T$ matrices that contains discrete time samples of $a_\alpha(\tau, \theta_i)$, $a_\beta(\tau, \theta_i)$ and $a_\rho(\tau, \theta_i)$ respectively.

2.3 Bayesian inversion

A forward model gives the effect of a cause, while an inverse model describes the cause of an observed effect. The observed effect is represented by the response vector $\mathbf{d} \in \mathbb{R}^q$ and the unknown model variable is represented by the vector $\mathbf{r} \in \mathbb{R}^T$. The relationship between them is given by the forward operator $G : \mathbb{R}^T \to \mathbb{R}^q$ plus an additive independent error term $\boldsymbol{\epsilon} \in \mathbb{R}^q$, including both random and systematic error. It is common to express the forward model as

$$\mathbf{d} = \mathbf{G}(\mathbf{r}) + \boldsymbol{\epsilon}. \tag{2.26}$$

The problem at hand is to determine $\mathbf{r}$ given $\mathbf{d}$. The Bayesian framework provides a robust solution to the inverse problem. In Bayesian inversion we introduce a likelihood model on the observed data and impose a prior model on the variables we want to determine. The problem is cast in a probabilistic setting where $(\mathbf{d}, \mathbf{r})$ are random variables. For an observation $\mathbf{d}$ the likelihood of $\mathbf{r}$ given the observations is equal to

$$[\mathbf{d}|\mathbf{r}] \sim p(\mathbf{d}|\mathbf{r}).$$

Here we have used the notation $\mathbf{x} \sim p(\mathbf{x})$ for the probability density function of a random variable $\mathbf{x}$. In addition, a prior model for $\mathbf{r}$ is defined on the form

$$\mathbf{r} \sim p(\mathbf{r}).$$

Bayes formula combines measured data and a priori information, and the posterior model is defined by

$$[\mathbf{r}|\mathbf{d}] \sim p(\mathbf{r}|\mathbf{d}) = \frac{p(\mathbf{d}|\mathbf{r})p(\mathbf{r})}{p(\mathbf{d})} = const \times p(\mathbf{d}|\mathbf{r})p(\mathbf{r}). \tag{2.27}$$

The Bayesian setting is a suitable choice for geophysical inverse problems. In this framework it is possible to combine available prior knowledge about the area of interest with actual observations from seismic surveys and log data. For most prior-likelihood model couples the normalizing constant in Expression 2.27 is hard to assess. If the solution is not analytically tractable, MCMC methods are commonly used to evaluate the posterior model.

By specifying a Gaussian prior model and a Gauss-linear likelihood model we ensure that the posterior distribution is Gaussian by the following:

If we have a joint distribution of two multivariate Gaussian random vectors

$$\begin{bmatrix}\mathbf{r}\\ \mathbf{d}\end{bmatrix} \sim N_{T+q}\left(\begin{bmatrix}\boldsymbol{\mu}_{\mathbf{r}}\\ \boldsymbol{\mu}_{\mathbf{d}}\end{bmatrix}, \begin{bmatrix}\boldsymbol{\Sigma}_{\mathbf{r}} & \boldsymbol{\Gamma}_{\mathbf{rd}}\\ \boldsymbol{\Gamma}_{\mathbf{dr}} & \boldsymbol{\Sigma}_{\mathbf{d}}\end{bmatrix}\right), \tag{2.28}$$

then the posterior distribution is found from the general formula for conditional multivariate Gaussian variables by

$$\begin{aligned}[\mathbf{r}|\mathbf{d}] \sim & p(\mathbf{r}|\mathbf{d}) = N_T(\boldsymbol{\mu}_{\mathbf{r}|\mathbf{d}}, \boldsymbol{\Sigma}_{\mathbf{r}|\mathbf{d}}),\\ & \text{with}\\ \boldsymbol{\mu}_{\mathbf{r}|\mathbf{d}} = & \boldsymbol{\mu}_{\mathbf{r}} + \boldsymbol{\Gamma}_{\mathbf{rd}}{\boldsymbol{\Sigma}_{\mathbf{d}}}^{-1}(\mathbf{d} - \boldsymbol{\mu}_{\mathbf{d}}),\\ \boldsymbol{\Sigma}_{\mathbf{r}|\mathbf{d}} = & \boldsymbol{\Sigma}_{\mathbf{r}} - \boldsymbol{\Gamma}_{\mathbf{rd}}{\boldsymbol{\Sigma}_{\mathbf{d}}}^{-1}\boldsymbol{\Gamma}_{\mathbf{dr}}.\end{aligned} \tag{2.29}$$

Hence the conditional distribution is also Gaussian.

2.4 Spatial random Field

Spatial data contain information about both an attribute of interest as well as its location. In order to analyze spatial data we need to have a suitable mathematical framework. This is provided by the spatial random field, which is denoted by

$$\{r(\mathbf{x}); \mathbf{x} \in \mathcal{D} \subset \mathbb{R}^m\}, \tag{2.30}$$

where $\mathcal{D}$ is the domain of $\mathbf{x}$. The random field is specified by the probability density function

$$\mathbf{r} = \begin{bmatrix} r(\mathbf{x_1}) \\ . \\ . \\ r(\mathbf{x_T}) \end{bmatrix} \sim p(\mathbf{r}), \tag{2.31}$$
$$\forall \text{ configurations } [\mathbf{x_1}, \ldots, \mathbf{x_T}] \in \mathcal{D}^T, \ \forall \ T \geq 1.$$

The most common spatial random field model is the Gaussian random field. The Gaussian random field shares the convenient mathematical properties of the Gaussian distribution and many problems can be solved analytically under a Gaussian assumption. A field is Gaussian if

$$p(\mathbf{r}) \sim N_T(\mathbf{r}; \boldsymbol{\mu}_\mathbf{r}, \boldsymbol{\Sigma}_\mathbf{r}).$$

In other words, all finite dimensional distributions of a Gaussian random field are multivariate Gaussian. A multivariate Gaussian distribution is fully specified by its expectation $\boldsymbol{\mu}_\mathbf{r}$ and covariance matrix $\boldsymbol{\Sigma}_\mathbf{r}$. In geostatistical applications it is common to assume that the random field is second order stationary and isotropic which means that:

$$\begin{aligned} E\left[r(\mathbf{x})\right] &= \mu, \\ Var\left[r(\mathbf{x})\right] &= \sigma^2, \\ Corr\left[r(\mathbf{x}'), r(\mathbf{x}'')\right] &= \nu(\Delta), \text{ where } \Delta = |\mathbf{x}' - \mathbf{x}''|. \end{aligned} \tag{2.32}$$

Hence, the mean and variance is constant over the field and the correlation between any two locations depends only on the distance between them. From this it follows that a (second order) stationary and isotropic Gaussian random field has a probability distribution that is invariant under translation and rotation.
In the following chapter we are concerned with a spatial random field

$$\{r(\boldsymbol{\tau}); \boldsymbol{\tau} \in \mathcal{D} \subset \mathbb{R}^1\}.$$

Chapter 3

Bayesian model setup

The observed variable in this inversion problem is a seismic AVO gather with n_θ angles on a regularly discretized vertical profile $\boldsymbol{\tau} = \{\tau_1, .., \tau_T\}$, denoted by $\mathbf{d} \in \mathbb{R}^{T \times n_\theta}$. We want to estimate the reservoir variables $\mathbf{r} \in \mathbb{R}^{T \times 2}$, which represent the porosity $\boldsymbol{\phi}$ and the water saturation $\mathbf{s_w}$. In Bayesian inversion we solve the inverse problem by evaluating the posterior distribution $p(\mathbf{r}|\mathbf{d})$. According to Section 2.3, the posterior model is defined by the likelihood model $p(\mathbf{d}|\mathbf{r})$ and the prior model $p(\mathbf{r})$. Computational efficiency is crucial when inverting large seismic data sets, as a seismic survey may contain millions of observations. We therefore confine ourselves to models where the posterior model is analytically tractable, although numerical methods may be required to obtain numerical values. We evaluate the posterior model by imposing three different prior models. The reason for testing different prior models on $\mathbf{r}$ is that the distribution of $\mathbf{r}$ may not be adequately represented by the unimodal, symmetrical and light tailed multivariate Gaussian prior, which is the traditional choice when evaluating spatial data. In Figure 3.1 we display histograms of a typical porosity and water saturation log, which indicate non-Gaussian behavior.

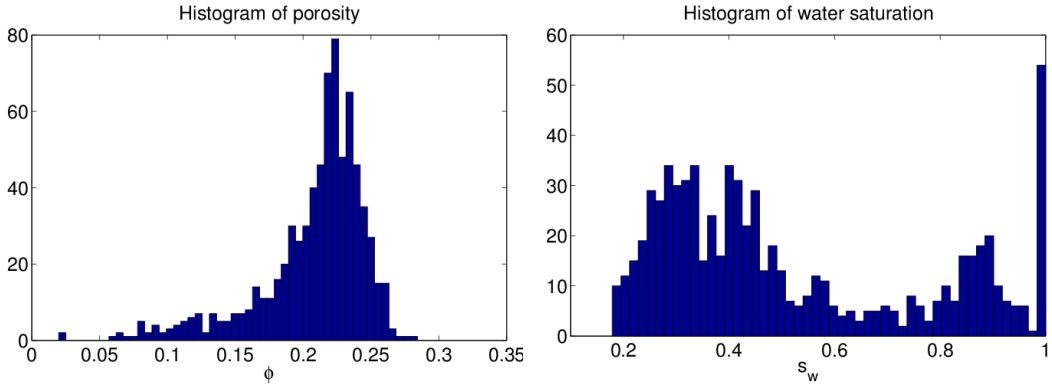

Figure 3.1: Typical histogram of ϕ and s_w.

We therefore examine prior models that exhibit multi-modality and skewness and compare them with the inversion result under the multivariate Gaussian prior model.

In order to simplify the notation in the following chapter, we deduce the mathematical results for $\mathbf{d} \in \mathbb{R}^T$ and $\mathbf{r} \in \mathbb{R}^T$. The results are trivially generalized to higher dimensions. The seismic gather $\mathbf{d}$ and reservoir variable $\mathbf{r}$ is discretized over $\boldsymbol{\tau}$ such that $\mathbf{d} = (d_1, \ldots, d_T)$ and $\mathbf{r} = (r_1, \ldots, r_T)$. We define $\mu_r = \mathrm{E}(r_j)$ for $j = 1, \ldots, T$, such that

$$\mathbf{r} = \mu_r \mathbf{i}_T + \boldsymbol{\epsilon}_{\mathbf{r}}, \tag{3.1}$$

where $\boldsymbol{\epsilon}_{\mathbf{r}} = (\epsilon_1, \ldots, \epsilon_T)$ is some additive error and we use the notation

$$\mathbf{i}_m = \begin{bmatrix} 1 \\ \vdots \\ 1 \end{bmatrix}_{m \times 1}, \tag{3.2}$$

for $m \times 1$ dimensional vector of ones, and

$$\mathbf{I}_m = \begin{bmatrix} 1 & & & 0 \\ & \cdot & & \\ & & \cdot & \\ & & & \cdot \\ 0 & & & 1 \end{bmatrix}_{m \times m}, \tag{3.3}$$

for a $m \times m$ identity matrix.

The reservoir variables only take real values in the range of $[0, 1]$. It is therefore convenient to introduce a logit transformation on $\mathbf{r}$ such that

$$r_j = \frac{e^{r_j^*}}{1 + e^{r_j^*}}, \quad j = 1, \ldots, T, \tag{3.4}$$

where $r_j^* \in \mathbb{R}^1$. The transformation ensures that the elements of $\mathbf{r}$ is confined to $[0, 1]$. The support of r_j^* is $\mathbb{R}^1$, hence $\mathbf{r}^*$ can be modeled as realizations from a continuous probability distribution defined over $\mathbb{R}^T$.

We start by developing the common observation likelihood model in Section 3.1. Then, in Section 3.2 we find the posterior model in a multivariate Gaussian prior setting. In Section 3.3 we develop the mixture Gaussian posterior model and in Section 3.4 we find the posterior model in the generalized Gaussian prior setting.

3.1 Rock physics likelihood model

In Landrø (2001) a second order regression formula is used to approximate the relationship between the change in the elastic variables and the reservoir variables. We use a similar idea, but in order to keep the rock physics likelihood linear, we use a first order approximation

$$[\mathbf{m}|\mathbf{r}] = \mathbf{B}\mathbf{r} + \boldsymbol{\epsilon}_{\mathbf{m}|\mathbf{r}}. \tag{3.5}$$

Here, $\mathbf{B}$ is a matrix containing the regression coefficients and $\boldsymbol{\epsilon}_{\mathbf{m}|\mathbf{r}}$ is an additive error term which contain both the error in the approximation and random error. We assume that the error term follows a Gaussian distribution such that $\boldsymbol{\epsilon}_{\mathbf{m}|\mathbf{r}} \sim N_T(0\mathbf{i}_T, \sigma^2_{m|r}\mathbf{I}_T)$. The coefficients in $\mathbf{B}$ are obtained by curve fitting the rock physics models listed in Section 2.1. By nesting the expressions in Expression 2.1 to 2.17, we obtain a model for the elastic variables that depends on the reservoir variables. We then find the best linear fit by applying least squares.

In Figure 3.2 to 3.7 the rock physics models are displayed together with the estimated linear fit over the range of the variable values. The linear assumption between the logit transformed reservoir variables and the logarithm of the elastic variables is a plausible assumption as the regression line is very coherent with the rock physic models in the given ranges. We observe that the slope of the regression lines are much steeper in the plots depicting porosity compared to in the water saturation plots. In fact, the relative size of the regression coefficients of ϕ and s_w range from 5 in the plots depicting v_p to 70 in the v_s plots. This means that the magnitude of the elastic variables relies heavily on the porosity in the reservoir.

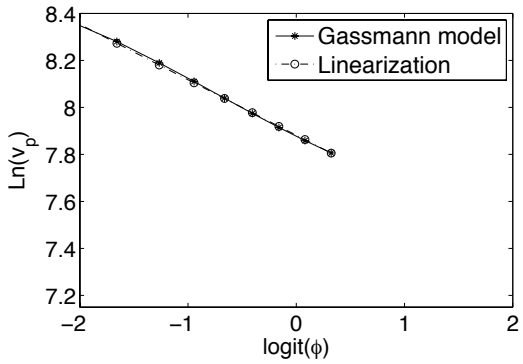

Figure 3.2: v_p as a function of logit(ϕ).

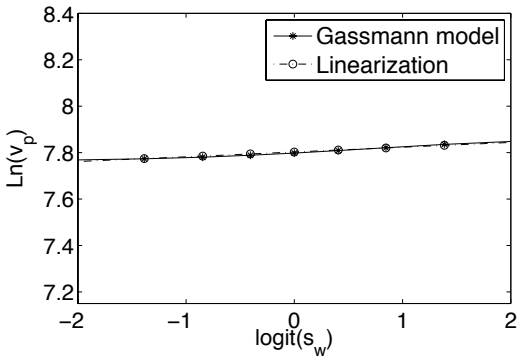

Figure 3.3: v_p as a function of logit(s_w).

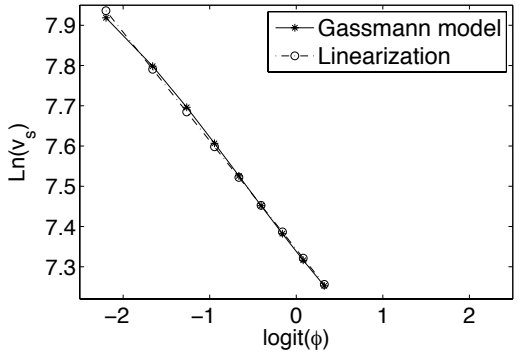

Figure 3.4: v_s as a function of logit(ϕ).

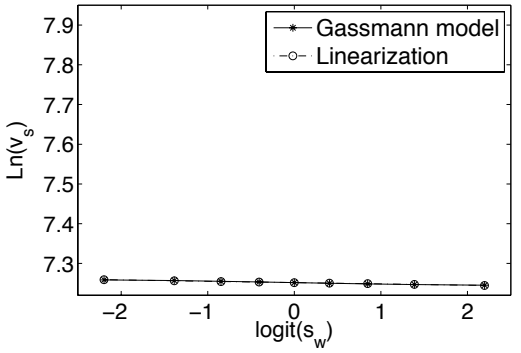

Figure 3.5: v_s as a function of logit(s_w).

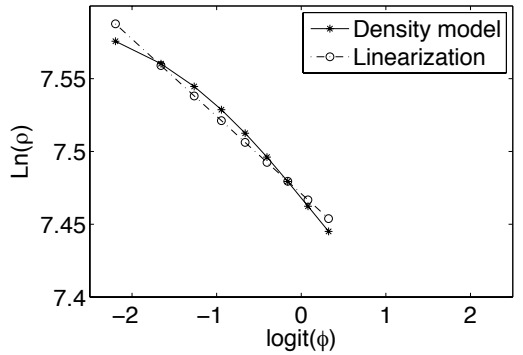

Figure 3.6: ρ as a function of logit(ϕ).

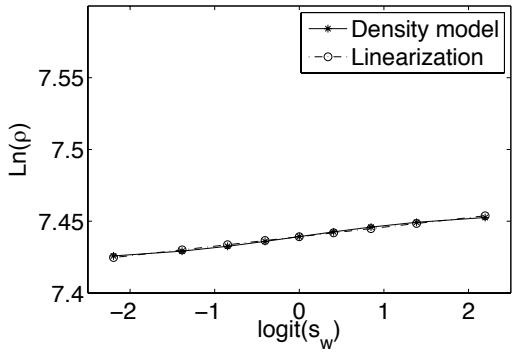

Figure 3.7: ρ as a function of logit(s_w).

3.1.1 Seismic likelihood model

The seismic likelihood model describes the relation between the change in seismic data and the elastic variables. In order to keep the problem on an analytical form, the Aki and Richards equations in Expression 2.20 is represented as a linear model with an additive Gaussian error term

$$[\mathbf{c}|\mathbf{m}] = \mathbf{ADm} + \boldsymbol{\epsilon}_{\boldsymbol{c|m}}, \tag{3.6}$$

where $\boldsymbol{\epsilon}_{\boldsymbol{c|m}} \sim N_T(0\mathbf{i}_T, \sigma^2_{c|m}\mathbf{I}_T)$. The seismic likelihood model is based on the seismic forward model defined in Buland and Omre (2003). The seismic traces are modeled by the convolution model in Expression 2.18 with model error and random error included in the error term which is assumed to be Gaussian, $\boldsymbol{\epsilon}_{\mathbf{d|r}} \sim N_T(0\mathbf{i}_T, \sigma^2_{d|r}\mathbf{I}_T)$. The discrete matrix form of the likelihood model is then

$$[\mathbf{d}|\mathbf{r}] = \mathbf{Wc} + \boldsymbol{\epsilon}_{\mathbf{d|r}}. \tag{3.7}$$

By inserting Expression 3.5 and 3.6 into Expression 3.7, we obtain the full likelihood model which defines the relationship between the reservoir variables and the seismic variables,

$$\begin{aligned}[\mathbf{d}|\mathbf{r}] &= \mathbf{WAD}(\mathbf{Br} + \boldsymbol{\epsilon}_{\mathbf{m|r}}) + \mathbf{W}\boldsymbol{\epsilon}_{\mathbf{c|m}} + \boldsymbol{\epsilon}_{\mathbf{d|r}} \\ &= \mathbf{Gr} + \boldsymbol{\varepsilon}_{\mathbf{d|r}},\end{aligned} \tag{3.8}$$

with

$$\boldsymbol{\varepsilon}_{\mathbf{d|r}} = \mathbf{WAD}\boldsymbol{\epsilon}_{\mathbf{m|r}} + \mathbf{W}\boldsymbol{\epsilon}_{\mathbf{c|m}} + \boldsymbol{\epsilon}_{\mathbf{d|r}}. \tag{3.9}$$

The additive error term $\boldsymbol{\varepsilon}_{\mathbf{d|r}}$ is a mixture of white and colored error. The colored error model both the error in the linear fit as well as uncertainty in the recording procedure of the seismic data. It may be hard to quantify the magnitude of the error in a likelihood model. However, the variance parameters should be chosen with great care as underspecification may lead to unrealistic predictions and overspecification causes information loss. This will be further discussed in Section 4.5. We now proceed by defining the prior models for the reservoir variable $\mathbf{r}$.

3.2 Gaussian prior model

Under the Gaussian prior assumption

$$\mathbf{r} \sim N_T(\boldsymbol{\mu}_\mathbf{r}, \boldsymbol{\Sigma}_\mathbf{r}), \tag{3.10}$$

where $\boldsymbol{\mu}_\mathbf{r} = \mu_r \mathbf{i}_T$ and $\boldsymbol{\Sigma}_\mathbf{r} = \sigma_r^2 \boldsymbol{\Sigma}_{\boldsymbol{r}}^{\boldsymbol{\nu}}$ are the expectation vector and variance matrix of $\mathbf{r}$. In this expression, σ_r^2 is the variance of r_j, $j = 1, \ldots, T$ and $\boldsymbol{\Sigma}_{\boldsymbol{r}}^{\boldsymbol{\nu}}$ is a spatial correlation matrix defined through a spatial correlation function $\nu(\cdot)$, which has the property

$$\nu(r_{j'}, r_{j''}) = \nu(|\tau_{j'} - \tau_{j''}|); \qquad \tau_{j'}, \tau_{j''} \in \boldsymbol{\tau}, \tag{3.11}$$

such that

$$\boldsymbol{\Sigma}_{\boldsymbol{r}}^{\boldsymbol{\nu}} = \begin{bmatrix} 1 & \nu(1) & . & . & \nu(T-1) \\ \nu(1) & 1 & & & \\ . & & . & & \\ . & & & . & \\ \nu(T-1) & & & & 1 \end{bmatrix}. \tag{3.12}$$

By marginalizing the likelihood in Expression 3.8 under the Gaussian prior assumption, we attain the joint distribution of $\mathbf{r}$ and $\mathbf{d}$,

$$\begin{bmatrix} \mathbf{r} \\ \mathbf{d} \end{bmatrix} \sim N_{2T}\left(\begin{bmatrix} \boldsymbol{\mu}_\mathbf{r} \\ \boldsymbol{\mu}_\mathbf{d} \end{bmatrix}, \begin{bmatrix} \boldsymbol{\Sigma}_\mathbf{r} & (\mathbf{G}\boldsymbol{\Sigma}_\mathbf{r})^\mathsf{T} \\ \mathbf{G}\boldsymbol{\Sigma}_\mathbf{r} & \boldsymbol{\Sigma}_\mathbf{d} \end{bmatrix} \right), \tag{3.13}$$

with

$$\begin{aligned} \boldsymbol{\mu}_\mathbf{d} &= \mathbf{G}\boldsymbol{\mu}_\mathbf{r}, \\ \boldsymbol{\Sigma}_\mathbf{d} &= \mathbf{G}\boldsymbol{\Sigma}_\mathbf{r}\mathbf{G}^\mathsf{T} + \mathbf{WAD}\sigma_{m|r}^2(\mathbf{WAD})^\mathsf{T} + \mathbf{W}\sigma_{c|m}^2\mathbf{W}^\mathsf{T} + \sigma_{d|r}^2\mathbf{I_T}. \end{aligned}$$

The posterior model is then obtained by using the general formula for conditional multivariate Gaussian variables given in Expression 2.29:

$$[\mathbf{r}|\mathbf{d}] \sim N_T(\boldsymbol{\mu}_{\mathbf{r}|\mathbf{d}}, \boldsymbol{\Sigma}_{\mathbf{r}|\mathbf{d}}), \tag{3.14}$$

with

$$\begin{aligned} \boldsymbol{\mu}_{\mathbf{r}|\mathbf{d}} &= \boldsymbol{\mu}_\mathbf{r} + \mathbf{G}\boldsymbol{\Sigma}_\mathbf{r}{\boldsymbol{\Sigma}_\mathbf{d}}^{-1}(\mathbf{d} - \boldsymbol{\mu}_\mathbf{d}), \\ \boldsymbol{\Sigma}_{\mathbf{r}|\mathbf{d}} &= \boldsymbol{\Sigma}_\mathbf{r} - \mathbf{G}\boldsymbol{\Sigma}_\mathbf{r}{\boldsymbol{\Sigma}_\mathbf{d}}^{-1}(\mathbf{G}\boldsymbol{\Sigma}_\mathbf{r})^\mathsf{T}. \end{aligned}$$

We use the posterior expectation as the predictor $\widehat{[\mathbf{r}|\mathbf{d}]}$ which coincide with both the median and the mode in the Gaussian framework. A $(1-\alpha)\%$ confidence interval is defined by $\left(\widehat{[\mathbf{r}|\mathbf{d}]} + \Phi^{-1}\left(\frac{\alpha}{2}\right)\hat{\boldsymbol{\sigma}}, \widehat{[\mathbf{r}|\mathbf{d}]} + \Phi^{-1}\left(1-\frac{\alpha}{2}\right)\hat{\boldsymbol{\sigma}}\right)$, where $\Phi^{-1}(\cdot)$ is the inverse of the Gaussian cumulative distribution function and $\hat{\boldsymbol{\sigma}}$ is a $T \times 1$ vector constructed by the square root of the diagonal elements in the $\boldsymbol{\Sigma}_{\mathbf{r}|\mathbf{d}}$ matrix.

In Figure 3.8 and 3.9 we show two examples of the symmetric and light tailed univariate Gaussian density function.

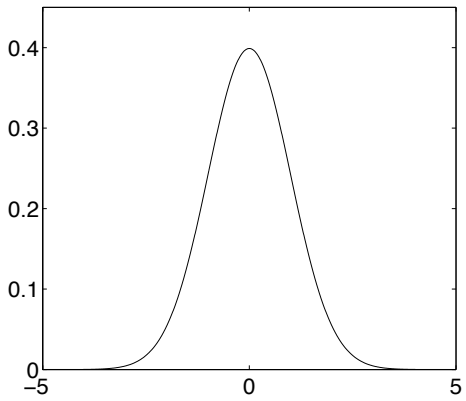

Figure 3.8: $\mu = 0$, $\sigma^2 = 1$

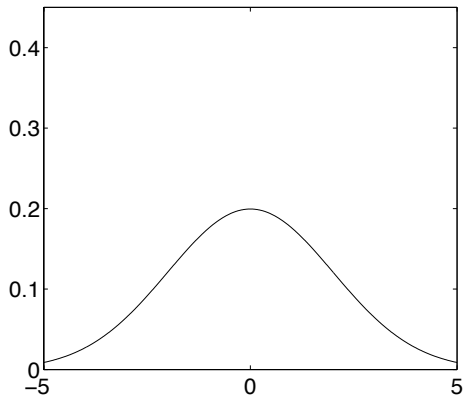

Figure 3.9: $\mu = 0$, $\sigma^2 = 4$

3.3 Mixture Gaussian prior model

Under the mixture Gaussian prior assumption, we have a latent categorical variable $\boldsymbol{\pi} = [\pi_1, ..., \pi_T]$, which takes values from a discrete state space such that $\pi_j \in \Omega_\pi : \{1, ..., L\}$ and $\boldsymbol{\pi} \in \Omega_\pi^T$. The prior for $\mathbf{r}$ is defined as

$$p(\mathbf{r}) = \sum_{\boldsymbol{\pi} \in \Omega_\pi^T} p(\mathbf{r}|\boldsymbol{\pi}) p(\boldsymbol{\pi}), \tag{3.15}$$

with

$$p(\mathbf{r}|\boldsymbol{\pi}) = N_T \left(\boldsymbol{\mu}_{\boldsymbol{r}|\boldsymbol{\pi}}, \boldsymbol{\Sigma}^{\boldsymbol{\sigma}}_{\boldsymbol{r}|\boldsymbol{\pi}} \boldsymbol{\Sigma}^{\boldsymbol{\nu}}_{\boldsymbol{r}} \boldsymbol{\Sigma}^{\boldsymbol{\sigma}}_{\boldsymbol{r}|\boldsymbol{\pi}} \right), \tag{3.16}$$

and

$$\boldsymbol{\mu}_{\boldsymbol{r}|\boldsymbol{\pi}} = \begin{bmatrix} \mu_{r|\pi_1} \\ . \\ . \\ . \\ \mu_{r|\pi_T} \end{bmatrix}, \qquad \boldsymbol{\Sigma}^{\boldsymbol{\sigma}}_{\boldsymbol{r}|\boldsymbol{\pi}} = \begin{bmatrix} \sigma_{r|\pi_1} & & & 0 \\ & . & & \\ & & . & \\ & & & . \\ 0 & & & \sigma_{r|\pi_T} \end{bmatrix}.$$

Here $\boldsymbol{\mu}_{\boldsymbol{r}|\boldsymbol{\pi}}$ is the conditional expectation vector of $\mathbf{r}$ given $\boldsymbol{\pi}$ and $\boldsymbol{\Sigma}^{\boldsymbol{\sigma}}_{\boldsymbol{r}|\boldsymbol{\pi}}$ is the conditional variance matrix. We assume that $\mu_{r|\pi}$ and $\sigma^2_{r|\pi}$ are known and only dependent of $\pi \in \Omega_\pi$. The spatial correlation matrix $\boldsymbol{\Sigma}^{\boldsymbol{\nu}}_{\boldsymbol{r}}$ is independent of π and defined in Expression 3.12. It follows that the marginal distributions are also mixture Gaussian,

$$p(r_j) = \sum_{\pi \in \Omega_\pi} p(r_j|\pi) p(\pi), \qquad j = 1, .., T \tag{3.17}$$

with

$$p(r_j|\pi) = N_1(\mu_{r|\pi}, \sigma^2_{r|\pi}).$$

Further, it is assumed that the latent categorical variable π is spatially independent, such that

$$p(\boldsymbol{\pi}) = \prod_{j=1}^{T} p(\pi_j). \tag{3.18}$$

A graph of the model is displayed in Figure 3.10. A possible extension of this model would be to apply a Markov chain model, but in this study we do

not explore this possibility.

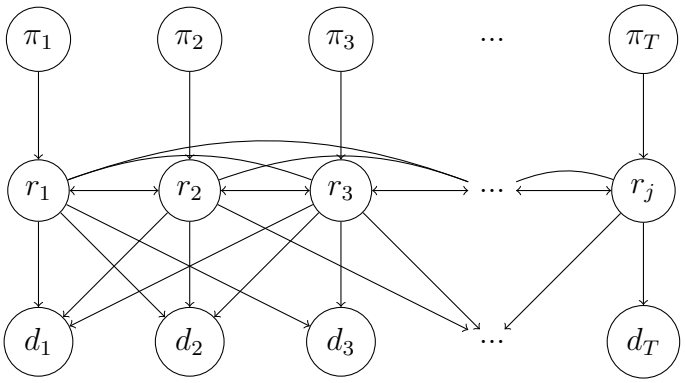

Figure 3.10: Graph of the model

By combining the mixture Gaussian prior model and the likelihood model given in Expression 3.8, the posterior model is obtained,

$$\begin{aligned} p(\mathbf{r}|\mathbf{d}) &= const \times p(\mathbf{d}|\mathbf{r})p(\mathbf{r}) \\ &= const \times p(\mathbf{d}|\mathbf{r}) \sum_{\boldsymbol{\pi} \in \Omega_\pi^T} p(\mathbf{r}|\boldsymbol{\pi}) \prod_{j=1}^{T} p(\pi_j), \end{aligned} \tag{3.19}$$

with

$$const = \left[\int p(\mathbf{d}|\mathbf{r}) \sum_{\boldsymbol{\pi} \in \Omega_\pi^T} p(\mathbf{r}|\boldsymbol{\pi}) d\mathbf{r} \prod_{j=1}^{T} p(\pi_j) \right]^{-1}.$$

The posterior model contains a sum over L^T terms so the model on its current form is inconvenient. To get around this problem, we want to find an approximate likelihood model such that the posterior model is found for each $[r_j|\mathbf{d}]$, $j = 1, \ldots, T$ separately. The full approximate posterior model is then found from

$$p^*(\mathbf{r}|\mathbf{d}) = \prod_{j=1}^{T} p^*(r_j|\mathbf{d}), \tag{3.20}$$

with

$$p^*(r_j|\mathbf{d}) = \frac{p^*(\mathbf{d}|r_j)p(r_j)}{p^*(\mathbf{d})}, \tag{3.21}$$

where $p(r_j)$ is given by the marginal distribution in Expression 3.17 and $p^*(\mathbf{r}|\mathbf{d})$ is some approximate posterior model. Note that this will not be the same as assuming no spatial dependency in the model as we will incorporate the spatial dependency into the approximation of $p^*(\mathbf{d}|r_j)$.

In order to evaluate the approximate posterior model we seek an approximate likelihood model on the form

$$p^*(\mathbf{d}|r_j) = \frac{1}{p(r_j)} \int \mathbf{p}(\mathbf{d}|\mathbf{r})\mathbf{p}^*(\mathbf{r})d\mathbf{r}_{-\mathbf{j}} = \frac{p^*(\mathbf{d}, r_j)}{p(r_j)}, \tag{3.22}$$

where $\mathbf{r}_{-\mathbf{j}} = (r_1, \ldots, r_{j-1}, r_{j+1}, \ldots, r_T)$.

We find the approximate likelihood model by assuming a Gaussian approximation prior

$$\mathbf{r} \overset{approx.}{\sim} p^*(\mathbf{r}), \tag{3.23}$$

with

$$p^*(\mathbf{r}) = N_T(\boldsymbol{\mu}^*_{\mathbf{r}}, \boldsymbol{\Sigma}^*_{\mathbf{r}}),$$

and

$$\boldsymbol{\mu_r}^* = E(\mathbf{r}) = \sum_{\pi \in \Omega_\pi} \boldsymbol{\mu}_{\mathbf{r}|\pi\mathbf{i}_T} p(\pi), \tag{3.24}$$

$$\boldsymbol{\Sigma}^*_{\boldsymbol{r}} = Var(\mathbf{r}) = \sum_{\pi \in \Omega_\pi} \boldsymbol{\Sigma}_{\mathbf{r}|\pi\mathbf{i}_T} p(\pi) + \sum_{\pi \in \Omega_\pi} \left[\boldsymbol{\mu}_{\mathbf{r}|\pi\mathbf{i}_T} - \boldsymbol{\mu_r}^*\right] \left[\boldsymbol{\mu}_{\mathbf{r}|\pi\mathbf{i}_T} - \boldsymbol{\mu_r}^*\right]^{\mathsf{T}} p(\pi). \tag{3.25}$$

In the approximation of the variance we assume that $\boldsymbol{\pi} = \pi\mathbf{i}_T$ in Expression 3.15, such that $p(\mathbf{r}|\pi\mathbf{i}_T) = N_T\left(\boldsymbol{\mu}_{\mathbf{r}|\pi\mathbf{i}_T}, \boldsymbol{\Sigma}^{\sigma}_{\mathbf{r}|\pi\mathbf{i}_T} \boldsymbol{\Sigma}^{\nu}_{\boldsymbol{r}} \boldsymbol{\Sigma}^{\sigma}_{\mathbf{r}|\pi\mathbf{i}_T}\right)$. Note that this is not the most accurate Gaussian approximation to the mixture Gaussian prior as the current approximation enforces higher correlation between the nodes. Our experience is that when the resulting method is tested on observations with error, this approximation provides more reliable results.

The joint distribution between $\mathbf{d}$ and $\mathbf{r}$ under the Gaussian approximation prior $p^*(\mathbf{r})$ is thereby

$$\begin{bmatrix}\mathbf{d}\\ \mathbf{r}\end{bmatrix} \sim p^*(\mathbf{d}, \mathbf{r}) = N_{2T}\left(\begin{bmatrix}\mathbf{G}\boldsymbol{\mu}^*_{\mathbf{r}}\\ \boldsymbol{\mu}^*_{\mathbf{r}}\end{bmatrix}, \begin{bmatrix}\boldsymbol{\Sigma}_{\mathbf{d}} & \mathbf{G}\boldsymbol{\Sigma}^*_{\mathbf{r}}\\ \boldsymbol{\Sigma}^*_{\mathbf{r}}\mathbf{G}^{\mathbf{T}} & \boldsymbol{\Sigma}^*_{\mathbf{r}}\end{bmatrix}\right). \tag{3.26}$$

By marginalizing Expression 3.26 with respect to r_j for $j = 1, .., T$, we obtain

$$\begin{bmatrix} \mathbf{d} \\ r_j \end{bmatrix} \sim p^*(\mathbf{d}, r_j) = N_{T+1}\left(\begin{bmatrix} \mathbf{G}\boldsymbol{\mu}_{\mathbf{r}}^* \\ \mu_{r_j}^* \end{bmatrix}, \begin{bmatrix} \boldsymbol{\Sigma}_{\mathbf{d}} & \boldsymbol{\gamma}_{\mathbf{d}r_j}^* \\ \boldsymbol{\gamma}_{\mathbf{d}r_j}^{*\mathsf{T}} & \sigma_{r_j}^{2*} \end{bmatrix} \right). \tag{3.27}$$

Here $\sigma_r^{2*} = Diag(\boldsymbol{\Sigma}_{\mathbf{r}}^*) = \left[\sigma_{r_1}^{2*}, \ldots, \sigma_{r_T}^{2*}\right]$ and $\boldsymbol{\gamma}_{\mathbf{d}r_j}^*$ is defined as the j'th row in $\mathbf{G}\boldsymbol{\Sigma}_{\mathbf{r}}^*$.

The approximate likelihood is now found by applying the formula for conditional Gaussian variables given in Expression 2.29

$$p^*(\mathbf{d}|r_j) = N_T(\boldsymbol{\mu}_{\mathbf{d}|r_j}^*, \boldsymbol{\Sigma}_{\mathbf{d}|r_j}^*), \quad j = 1, \ldots, T, \tag{3.28}$$

with

$$\begin{aligned} \boldsymbol{\mu}_{\mathbf{d}|r_j}^* &= \mathbf{G}\boldsymbol{\mu}_{\mathbf{r}}^* + \frac{1}{\sigma_{r_j}^{2*}}\boldsymbol{\gamma}_{\mathbf{d}r_j}(r_j - \mu_{r_j}^*), \\ \boldsymbol{\Sigma}_{\mathbf{d}|r_j}^* &= \boldsymbol{\Sigma}_{\mathbf{d}} - \frac{1}{\sigma_{r_j}^{2*}}\boldsymbol{\gamma}_{\mathbf{d}r_j}\boldsymbol{\gamma}_{\mathbf{d}r_j}^{*\mathsf{T}}, \end{aligned}$$

and we see that the approximate likelihood is Gauss-linear.

By combining the approximate likelihood with the mixture Gaussian marginal prior model, the approximate posterior model is established. We rewrite Expression 3.21 such that

$$\begin{aligned} p^*(r_j|\mathbf{d}) &= \sum_{\pi} \left[\frac{p^*(\mathbf{d}|r_j, \pi)p(r_j|\pi)p(\pi)}{p(\mathbf{d})} \times \frac{p^*(\mathbf{d}|\pi)}{p^*(\mathbf{d}|\pi)} \right] && (3.29) \\ &= p^*(r_j|\mathbf{d}, \pi)\frac{p^*(\mathbf{d}|\pi)p(\pi)}{\sum p^*(\mathbf{d}|\pi)p(\pi)} && (3.30) \\ &= p^*(r_j|\mathbf{d}, \pi)p^*(\pi|\mathbf{d}), && (3.31) \end{aligned}$$

and we see that the posterior model is also a mixture Gaussian model.

The posterior probabilities for $\pi \in \Omega_\pi$ is assessed by the likelihood

$$p^*(\mathbf{d}|\pi) = \int p^*(\mathbf{d}|r_j)p(r_j|\pi)dr_j = \int p^*(\mathbf{d}, r_j|\pi)dr_j, \tag{3.32}$$

which is easily evaluated as $p(\mathbf{d}|r_j)$ and $p(r_j|\pi)$ are both Gaussian densities

$$p^*(\mathbf{d}|\pi) = N_T\left(\boldsymbol{\mu}^*_{\mathbf{d}|\pi}, \boldsymbol{\Sigma}^*_{\mathbf{d}|\pi}\right), \tag{3.33}$$

with

$$\boldsymbol{\mu}^*_{\mathbf{d}|\pi} = \mathbf{G}\boldsymbol{\mu}^*_{\mathbf{r}} + \frac{1}{\sigma^{2*}_{r_j}}\boldsymbol{\gamma}_{\mathbf{d}r_j}(\mu_{r|\pi} - \mu^*_{r_j}),$$
$$\boldsymbol{\Sigma}^*_{\mathbf{d}|\pi} = \boldsymbol{\Sigma}^*_{\mathbf{d}|r_j} + \frac{\boldsymbol{\gamma}_{\mathbf{d}r_j}}{\sigma^{2*}_{r_j}}\sigma^2_{r|\pi}\frac{\boldsymbol{\gamma}^{*\mathsf{T}}_{\mathbf{d}r_j}}{\sigma^{2*}_{r_j}}.$$

Since the mixture Gaussian distribution is multimodal, the expectation and median are not good predictors for $[r_j|\mathbf{d}]$ as they usually will be located in low-probability regions of the posterior pdf. We choose the mode as our predictor for $[r_j|\mathbf{d}]$ in the mixture Gaussian setting. Hence we use the marginal MAP predictor for $[\mathbf{r}|\mathbf{d}]$:

$$\hat{\mathbf{r}} = \{\widehat{[r_j|\mathbf{d}]} = \arg\max_{r_j} p(r_j|\mathbf{d}); j = 1, \ldots, T\}. \tag{3.34}$$

In order to get an estimate of the uncertainty in the predictor, we find a $100(1-\alpha)\%$ confidence interval $\left[Q_{j,1-\frac{\alpha}{2}}, Q_{j,\frac{\alpha}{2}}\right]$ such that

$$p\left(Q_{j,1-\frac{\alpha}{2}} \leq r_j \leq Q_{j,\frac{\alpha}{2}}|\mathbf{d}\right) = 1-\alpha, \qquad j = 1, \ldots, T, \tag{3.35}$$

where $Q_{j,1-\frac{\alpha}{2}}$ and $Q_{j,\frac{\alpha}{2}}$ are found by a root finding function in MATLAB.

In Figure 3.11 we display four different parameter choices in the univariate mixture Gaussian model, see Table 3.1 for the setups.

	p($\pi=0$)	p($\pi=1$)	$\mu_{\pi=0}$	$\mu_{\pi=1}$	$\sigma^2_{\pi=0}$	$\sigma^2_{\pi=1}$
Setup 1	0.3	0.7	-2	2	1	1
Setup 2	0.6	0.4	-2	3	5	5
Setup 3	0.5	0.5	-1	1	1	1
Setup 4	0.5	0.5	-2	2	1	1

Table 3.1: Parameters in the mixture Gaussian model setups

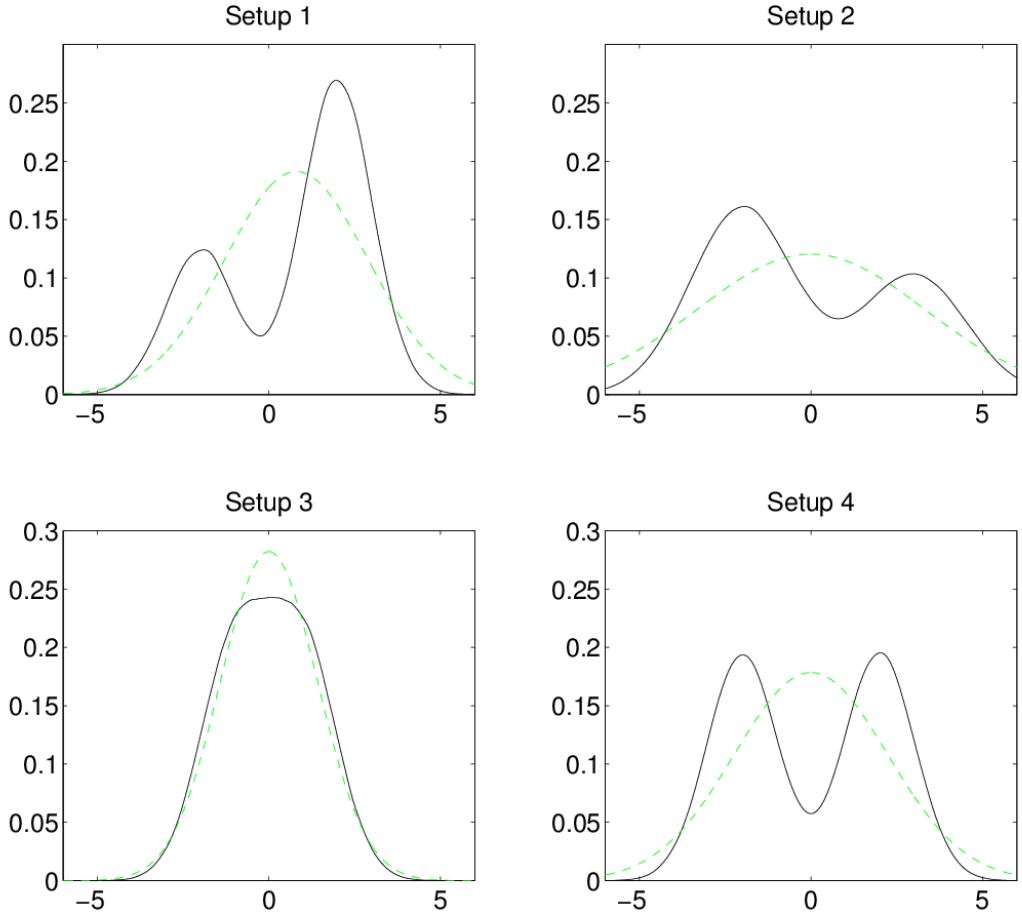

Figure 3.11: The univariate mixture Gaussian density $p(\mathbf{r})$ is illustrated by the black solid line together with the corresponding univariate approximate distribution $p^*(\mathbf{r})$ given by the green stippled line.

3.4 Generalized Gaussian prior model

In order to capture the skewed and bi-modal nature of $\mathbf{r}$, the random variable is modeled by a generalized Gaussian distribution. The generalized Gaussian distribution provides a unification of the multivariate and various selection normal distributions. The distribution allows modeling of skewness and multi-modality while retaining some of the convenient properties of the Gaussian distribution such as being closed under marginalization, linear transformation and conditioning. In Rimstad and Omre (2012), the generalized Gaussian random field on a regularly discretized vertical profile $\boldsymbol{\tau} = \{\tau_1, \ldots, \tau_T\}$ is defined as follows:

Consider a vector $\tilde{\mathbf{r}} \in \mathbb{R}^T$ and $\mathbf{u} \in \mathbb{R}^T$ which are jointly a Gaussian random variable

$$\begin{bmatrix} \tilde{\mathbf{r}} \\ \mathbf{u} \end{bmatrix} \sim N_{2T}(\boldsymbol{\mu}, \boldsymbol{\Sigma}), \tag{3.36}$$

where

$$\begin{aligned} \boldsymbol{\mu} &= \begin{bmatrix} \boldsymbol{\mu}_{\tilde{\mathbf{r}}} \\ \boldsymbol{\mu}_{\mathbf{u}} \end{bmatrix}, \\ \boldsymbol{\Sigma} &= \begin{bmatrix} \boldsymbol{\Sigma}_{\tilde{\mathbf{r}}} & \boldsymbol{\Gamma}_{\tilde{\mathbf{r}}\mathbf{u}} \\ \boldsymbol{\Gamma}_{\mathbf{u}\tilde{\mathbf{r}}} & \boldsymbol{\Sigma}_{\mathbf{u}} \end{bmatrix}, \end{aligned}$$

and

$$\begin{aligned} \boldsymbol{\mu}_{\tilde{\mathbf{r}}} &= \mu_{\tilde{r}} \mathbf{i}_T, \\ \boldsymbol{\mu}_{\mathbf{u}} &= 0 \mathbf{i}_T, \\ \boldsymbol{\Sigma}_{\tilde{\mathbf{r}}} &= \sigma^2_{\tilde{r}} \boldsymbol{\Sigma}^{\boldsymbol{\nu}}_{\tilde{\boldsymbol{r}}}, \\ \boldsymbol{\Gamma}_{\mathbf{u}\tilde{\mathbf{r}}} &= \gamma \sigma_{\tilde{r}} \boldsymbol{\Sigma}^{\boldsymbol{\nu}}_{\tilde{\boldsymbol{r}}}, \\ \boldsymbol{\Sigma}_{\mathbf{u}} &= (1 - \gamma^2) \mathbf{I}_T + \gamma^2 \sigma^2_{\tilde{r}} \boldsymbol{\Sigma}^{\boldsymbol{\nu}}_{\tilde{\boldsymbol{r}}}. \end{aligned}$$

Here, $\mu_{\tilde{r}}$ and $\sigma^2_{\tilde{r}}$ are the expectation and covariance of $\tilde{r}_t \in \tilde{\mathbf{r}}$, $\boldsymbol{\Sigma}^{\boldsymbol{\nu}}_{\tilde{\boldsymbol{r}}}$ is the spatial correlation matrix as defined in Expression 3.12 and γ defines the coupling structure, with $|\gamma| \leq 1$.

The random field of interest is then

$$\mathbf{r} = [\tilde{\mathbf{r}} | \mathbf{u} \in \mathbf{A}] \in \mathbb{R}^T, \tag{3.37}$$

where $\mathbf{A}$ is the selection set. There are many possible parameterizations of the selection set $\mathbf{A}$. In the current study we consider the family of distributions where $A_j \in \mathbf{A}$ is constructed by two line segments $A_j = (l_j^1, u_j^1) \cup (l_j^2, u_j^2)$, $j = 1, \ldots, T$, where l_j^1 and l_j^2 gives the lower bounds and u_j^1 and u_j^2 gives the upper bounds for the two line segments. This parameterization of $\mathbf{A}$ can define a bimodal distribution for $\mathbf{u}$. If we let $\phi_T(\cdot)$ denote the Gaussian probability density function and $\Phi_T(\mathbf{A}; \boldsymbol{\mu}, \boldsymbol{\Sigma}) = \int_{\mathbf{y} \in \mathbf{A}} \phi_T(\mathbf{y}; \boldsymbol{\mu}, \boldsymbol{\Sigma}) d\mathbf{y}$, then the pdf of $\mathbf{r}$ is specified by

$$\begin{aligned} p(\mathbf{r}) = p(\tilde{\mathbf{r}} | \mathbf{u} \in \mathbf{A}) &= \frac{p(\mathbf{u} \in \mathbf{A} | \tilde{\mathbf{r}}) p(\tilde{\mathbf{r}})}{p(\mathbf{u} \in \mathbf{A})} \\ &= \frac{\Phi_T(\mathbf{A}; \boldsymbol{\mu}_{\mathbf{u}|\tilde{\mathbf{r}}}, \boldsymbol{\Sigma}_{\mathbf{u}|\tilde{\mathbf{r}}}) \phi_T(\mathbf{r}; \boldsymbol{\mu}_{\tilde{\mathbf{r}}}, \boldsymbol{\Sigma}_{\tilde{\mathbf{r}}})}{\Phi_T(\mathbf{A}; \boldsymbol{\mu}_{\mathbf{u}}, \boldsymbol{\Sigma}_{\mathbf{u}})}, \end{aligned} \tag{3.38}$$

where

$$\begin{aligned} \boldsymbol{\mu}_{\mathbf{u}|\tilde{\mathbf{r}}} &= \boldsymbol{\mu}_{\mathbf{u}} + \boldsymbol{\Gamma}_{\mathbf{u}\tilde{\mathbf{r}}} \boldsymbol{\Sigma}_{\tilde{\mathbf{r}}}^{-\mathbf{1}} (\mathbf{r} - \boldsymbol{\mu}_{\tilde{\mathbf{r}}}), \\ \boldsymbol{\Sigma}_{\mathbf{u}|\tilde{\mathbf{r}}} &= \boldsymbol{\Sigma}_{\mathbf{u}} - \boldsymbol{\Gamma}_{\mathbf{u}\tilde{\mathbf{r}}} \boldsymbol{\Sigma}_{\tilde{\mathbf{r}}}^{-\mathbf{1}} \boldsymbol{\Gamma}_{\tilde{\mathbf{r}}\mathbf{u}}. \end{aligned}$$

Now, $\mathbf{r}$ is distributed as a multivariate generalized Gaussian distribution with respect to an arbitrary set $\mathbf{A} \in \mathbb{R}^T$ and the prior model is denoted by

$$\mathbf{r} \sim GenGauss_{T,T}(\boldsymbol{\mu}_{\tilde{\mathbf{r}}}, \boldsymbol{\mu}_{\mathbf{u}}, \boldsymbol{\Sigma}_{\tilde{\mathbf{r}}}, \boldsymbol{\Sigma}_{\mathbf{u}}, \boldsymbol{\Gamma}_{\tilde{\mathbf{r}}\mathbf{u}}, \mathbf{A}). \tag{3.39}$$

The model flexibility lies in the choice of model parameters $\boldsymbol{\mu}$, $\boldsymbol{\Sigma}$ and the selection set $\mathbf{A} \in \mathbb{R}^T$.

In the generalized Gaussian case, we define the likelihood model for $\mathbf{d}$ as

$$\mathbf{d} = \mathbf{G}\tilde{\mathbf{r}} + \boldsymbol{\varepsilon}_{\mathbf{d}|\tilde{\mathbf{r}}}, \tag{3.40}$$

where $\boldsymbol{\varepsilon}_{\mathbf{d}|\tilde{\mathbf{r}}}$ is an additive error term

$$\boldsymbol{\varepsilon}_{\mathbf{d}|\tilde{\mathbf{r}}} = \mathbf{WAD}\boldsymbol{\epsilon}_{\mathbf{m}|\tilde{\mathbf{r}}} + \mathbf{W}\boldsymbol{\epsilon}_{\mathbf{c}|\mathbf{m}} + \boldsymbol{\epsilon}_{\mathbf{d}|\tilde{\mathbf{r}}}. \tag{3.41}$$

with

$$\begin{gathered} \boldsymbol{\epsilon}_{\mathbf{m}|\tilde{\mathbf{r}}} \sim N_T(0\mathbf{i}_T, \sigma^2_{m|\tilde{r}}\mathbf{I}_T), \qquad \boldsymbol{\epsilon}_{\mathbf{d}|\tilde{\mathbf{r}}} \sim N_T\left(0\mathbf{i}_T, \sigma^2_{d|\tilde{r}}\mathbf{I}_T\right), \\ \boldsymbol{\epsilon}_{\boldsymbol{c}|\boldsymbol{m}} \sim N_T\left(0\mathbf{i}_T, \sigma^2_{c|m}\mathbf{I}_T\right). \end{gathered}$$

By marginalizing the likelihood model under the generalized Gaussian prior assumption we get

$$\mathbf{d} \sim N_T(\mathbf{G}\boldsymbol{\mu}_{\tilde{\mathbf{r}}}, \boldsymbol{\Sigma}_{\mathbf{d}}), \tag{3.42}$$

with

$$\boldsymbol{\Sigma}_{\mathbf{d}} = \mathbf{G}\boldsymbol{\Sigma}_{\tilde{\mathbf{r}}}\mathbf{G}^{\mathsf{T}} + \mathbf{WAD}\sigma^2_{m|\tilde{r}}(\mathbf{WAD})^{\mathsf{T}} + \mathbf{W}\sigma^2_{c|m}\mathbf{W}^{\mathsf{T}} + \sigma^2_{d|\tilde{r}}\mathbf{I}_T.$$

By combining Expression 3.36 and 3.42, the joint distribution of $\tilde{\mathbf{r}}, \mathbf{d}$ and $\mathbf{u}$ is available to us

$$\begin{bmatrix} \tilde{\mathbf{r}} \\ \mathbf{d} \\ \mathbf{u} \end{bmatrix} \sim N_{3T}\left(\begin{bmatrix} \boldsymbol{\mu}_{\tilde{\mathbf{r}}} \\ \mathbf{G}\boldsymbol{\mu}_{\tilde{\mathbf{r}}} \\ \boldsymbol{\mu}_{\mathbf{u}} \end{bmatrix}, \begin{bmatrix} \boldsymbol{\Sigma}_{\tilde{\mathbf{r}}} & \boldsymbol{\Gamma}_{\tilde{\mathbf{r}}\mathbf{d}} & \boldsymbol{\Gamma}_{\tilde{\mathbf{r}}\mathbf{u}} \\ \boldsymbol{\Gamma}_{\mathbf{d}\tilde{\mathbf{r}}} & \boldsymbol{\Sigma}_{\mathbf{d}} & \boldsymbol{\Gamma}_{\mathbf{du}} \\ \boldsymbol{\Gamma}_{\mathbf{u}\tilde{\mathbf{r}}} & \boldsymbol{\Gamma}_{\mathbf{ud}} & \boldsymbol{\Sigma}_{\mathbf{u}} \end{bmatrix} \right), \tag{3.43}$$

where $\boldsymbol{\Gamma}_{\mathbf{du}} = \mathbf{G}\boldsymbol{\Gamma}_{\tilde{\mathbf{r}}\mathbf{u}}$ and $\boldsymbol{\Gamma}_{\tilde{\mathbf{r}}\mathbf{d}} = \mathbf{G}\boldsymbol{\Sigma}_{\tilde{\mathbf{r}}}$.

Now, we condition on $\mathbf{d}$, such that

$$\begin{bmatrix} \tilde{\mathbf{r}}|\mathbf{d} \\ \mathbf{u}|\mathbf{d} \end{bmatrix} \sim N_{2T}\left(\begin{bmatrix} \boldsymbol{\mu}_{\tilde{\mathbf{r}}|\mathbf{d}} \\ \boldsymbol{\mu}_{\mathbf{u}|\mathbf{d}} \end{bmatrix}, \begin{bmatrix} \boldsymbol{\Sigma}_{\tilde{\mathbf{r}}|\mathbf{d}} & \boldsymbol{\Gamma}_{\tilde{\mathbf{r}}\mathbf{u}|\mathbf{d}} \\ \boldsymbol{\Gamma}_{\mathbf{u}\tilde{\mathbf{r}}|\mathbf{d}} & \boldsymbol{\Sigma}_{\mathbf{u}|\mathbf{d}} \end{bmatrix} \right), \tag{3.44}$$

with

$$\begin{aligned} \boldsymbol{\mu}_{\tilde{\mathbf{r}}|\mathbf{d}} &= \boldsymbol{\mu}_{\tilde{\mathbf{r}}} + \boldsymbol{\Gamma}_{\tilde{\mathbf{r}}\mathbf{d}}{\boldsymbol{\Sigma}_{\mathbf{d}}}^{-1}(\mathbf{G}\tilde{\mathbf{r}} - \mathbf{G}\boldsymbol{\mu}_{\tilde{\mathbf{r}}}), \\ \boldsymbol{\mu}_{\mathbf{u}|\mathbf{d}} &= \boldsymbol{\Gamma}_{\mathbf{ud}}{\boldsymbol{\Sigma}_{\mathbf{d}}}^{-1}(\mathbf{G}\tilde{\mathbf{r}} - \mathbf{G}\boldsymbol{\mu}_{\tilde{\mathbf{r}}}), \\ \boldsymbol{\Sigma}_{\tilde{\mathbf{r}}|\mathbf{d}} &= \boldsymbol{\Sigma}_{\tilde{\mathbf{r}}} - \boldsymbol{\Gamma}_{\tilde{\mathbf{r}}\mathbf{d}}{\boldsymbol{\Sigma}_{\mathbf{d}}}^{-1}{\boldsymbol{\Gamma}_{\tilde{\mathbf{r}}\mathbf{d}}}^{\mathsf{T}}, \\ \boldsymbol{\Sigma}_{\mathbf{u}|\mathbf{d}} &= \boldsymbol{\Sigma}_{\mathbf{u}} - \boldsymbol{\Gamma}_{\mathbf{ud}}{\boldsymbol{\Sigma}_{\mathbf{d}}}^{-1}{\boldsymbol{\Gamma}_{\mathbf{ud}}}^{\mathsf{T}}, \\ \boldsymbol{\Gamma}_{\tilde{\mathbf{r}}\mathbf{u}|\mathbf{d}} &= \boldsymbol{\Gamma}_{\tilde{\mathbf{r}}\mathbf{u}} - \boldsymbol{\Gamma}_{\tilde{\mathbf{r}}\mathbf{d}}{\boldsymbol{\Sigma}_{\mathbf{d}}}^{-1}{\boldsymbol{\Gamma}_{\mathbf{ud}}}^{\mathsf{T}}. \end{aligned}$$

Following the reasoning leading up to Expression 3.36-3.39, it is apparent that the posterior model is also generalized Gaussian distributed with

$$[\mathbf{r}|\mathbf{d}] \equiv [\tilde{\mathbf{r}}|\mathbf{d}, \mathbf{u} \in \mathbf{A}] \sim GenGauss_{T,T}(\boldsymbol{\mu}_{\tilde{\mathbf{r}}|\mathbf{d}}, \boldsymbol{\mu}_{\mathbf{u}|\mathbf{d}}, \boldsymbol{\Sigma}_{\tilde{\mathbf{r}}|\mathbf{d}}, \boldsymbol{\Gamma}_{\tilde{\mathbf{r}}\mathbf{u}|\mathbf{d}}, \boldsymbol{\Sigma}_{\mathbf{u}|\mathbf{d}}, \mathbf{A}). \tag{3.45}$$

The marginal MAP solution is used as the predictor of $[\mathbf{r}|\mathbf{d}]$ in the generalized Gaussian setting.

$$\hat{\mathbf{r}} = \{\widehat{[r_j|\mathbf{d}]} = \arg\max_{r_j} p(r_j|\mathbf{d}); j = 1, \ldots, T\}. \tag{3.46}$$

The posterior marginal MAP predictor is easily obtainable by numerical optimization as the expression for the posterior marginal density is known. The general form for the generalized Gaussian density function is given in Expression 3.38, and by inserting the parameters in Expression 3.45, we obtain the density function for the posterior distribution. A confidence interval for the predictor is found by solving for $\left[Q_{j,1-\frac{\alpha}{2}}, Q_{j,\frac{\alpha}{2}}\right]$ in Expression 3.35. The numerical values for the bounds are found by using the trapezoidal method on the posterior density function.

In Figure 3.12 we display four different parameter choices in the univariate generalized Gaussian model $p(\mathbf{r})$, see Table 3.2.

	l_j^1	u_j^1	l_j^2	u_j^2	$\mu_{\tilde{r}}$	$\sigma_{\tilde{r}}^2$	γ
Setup 1	$-\infty$	-1	1	∞	0	1	0.5
Setup 2	$-\infty$	-1	0.5	∞	0	1	0.6
Setup 4	$-\infty$	-1	0.5	∞	0	3	0.5
Setup 3	-1.1	-1	1	∞	0	1	0.4

Table 3.2: Parameters in the generalized Gaussian model setups

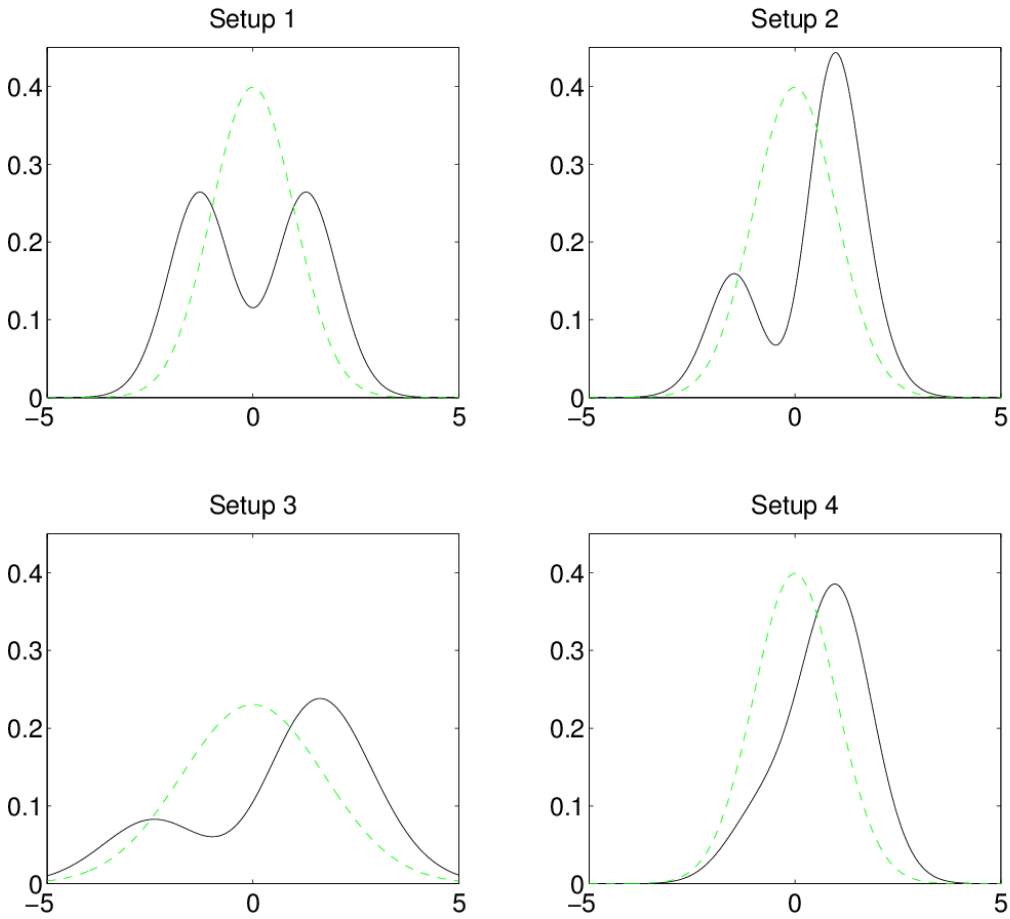

Figure 3.12: The univariate generalized Gaussian density $p(\mathbf{r})$ is illustrated by the black solid line together with the univariate Gaussian density $p(\tilde{\mathbf{r}})$ given by the green stippled line.

Chapter 4

Synthetic data study

In this chapter, the inversion methodology is tested on synthetic seismic data. We start by defining the common model design for the inversion problem at hand. Then in Section 4.2-4.6 we display and discuss the inversion results for the different prior model cases. In Appendix A we have included more test runs where we over- and underspecify the error in the inversion model.

4.1 Synthetic model design

The synthetic data is created by the forward model and a reference reservoir variable profile. The reference profile at t_0 consists of porosity $\boldsymbol{\phi}$ and water saturation $\mathbf{s_{w,0}}$. The profiles are segments from actual reservoir log data. We let t_0 be a time step prior to production and let t_1 represent a time step post production start. A reservoir that has been in production for some time will have a higher oil-water contact than at original reservoir conditions. The synthetic data for the water saturation at t_1 is therefore created by lifting the oil water contact. The porosity is assumed to be the same at the two time steps. The reference profiles are shown in Figure 4.1.
The variable of interest is

$$\mathbf{r} = \begin{bmatrix} \mathbf{r_0} \\ \mathbf{\Delta r} \end{bmatrix} = \begin{bmatrix} \boldsymbol{\phi} \\ \mathbf{s_{w,0}} \\ \mathbf{\Delta s_w} \end{bmatrix} \in \mathbb{R}^{3T}, \tag{4.1}$$

discretized over a 1D vertical profile $\boldsymbol{\tau} = (\tau_1, \ldots, \tau_T)$. We use a logit transformation on $s_{w,0}$ and a modified logit transformation on ϕ which confines the porosity to $[0, 0.5]$.

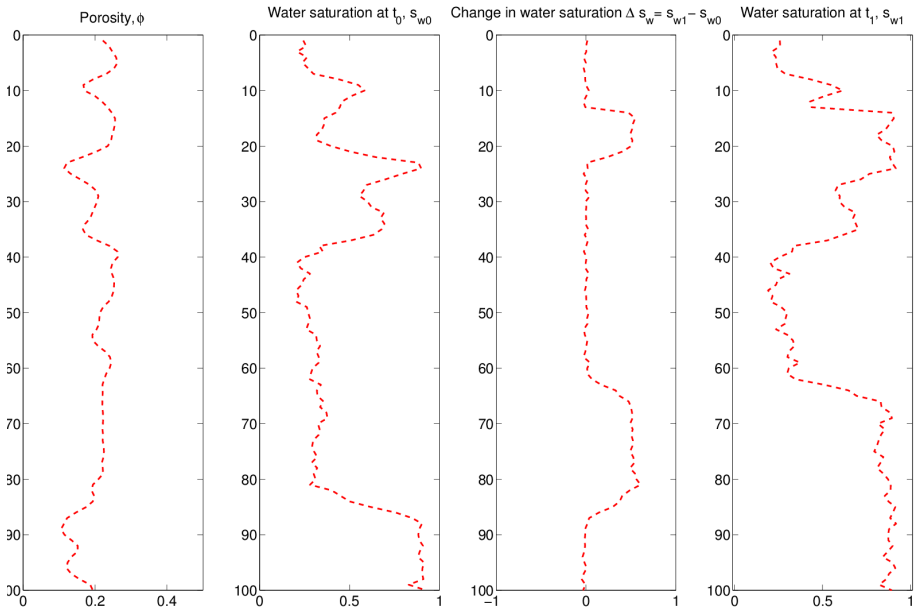

Figure 4.1: Reference reservoir variable profile

The expectation and variance of $\mathbf{r}$ is given by

$$\mathrm{E}\begin{bmatrix}\boldsymbol{\phi}\\ \mathbf{s_{w,0}}\\ \boldsymbol{\Delta}\mathbf{s_w}\end{bmatrix} = \begin{bmatrix}0.2\mathbf{i}_T\\ 0.5\mathbf{i}_T\\ 0.25\mathbf{i}_T\end{bmatrix},$$

and

$$\mathrm{Var}\begin{bmatrix}\boldsymbol{\phi}\\ \mathbf{s_{w,0}}\\ \boldsymbol{\Delta}\mathbf{s_w}\end{bmatrix} = \begin{bmatrix}\sigma_\phi^2\boldsymbol{\Sigma}_{\boldsymbol{r}}^{\boldsymbol{\nu}} & \gamma_{s_w,\phi}\sigma_{s_w}\sigma_\phi\boldsymbol{\Sigma}_{\boldsymbol{r}}^{\boldsymbol{\nu}} & 0\mathbf{I}_T\\ \gamma_{s_w,\phi}\sigma_{s_w}\sigma_\phi\boldsymbol{\Sigma}_{\boldsymbol{r}}^{\boldsymbol{\nu}} & \sigma_{s_w}^2\boldsymbol{\Sigma}_{\boldsymbol{r}}^{\boldsymbol{\nu}} & 0\mathbf{I}_T\\ 0\mathbf{I}_T & 0\mathbf{I}_T & \sigma_{\Delta s_w}^2\boldsymbol{\Sigma}_{\boldsymbol{r}}^{\boldsymbol{\nu}}\end{bmatrix}. \tag{4.2}$$

Here, $\sigma_\phi^2, \sigma_{s_w}^2$ and $\sigma_{\Delta s_w}^2$ are the variances of the porosity, water saturation and change in water saturation respectively. The correlation between s_w and ϕ at t_0 is denoted by $\gamma_{s_w,\phi} = -0.3$ and $\boldsymbol{\Sigma}_{\boldsymbol{r}}^{\boldsymbol{\nu}}$ is defined through Expression 3.12, where we have used a Gaussian correlation function with $\delta = 4$,

$$\nu(r_{j'}, r_{j''}) = \exp\left(\frac{|\tau_{j'} - \tau_{j''}|^2}{\delta^2}\right), \qquad \tau_{j'}, \tau_{j''} \in \boldsymbol{\tau}.$$

Further, all the change in the synthetic seismogram from t_0 to t_1 is contributed to the change the water saturation, so we model $\mathbf{\Delta r}$ by $\mathbf{\Delta s_w}$ only. The water saturation at time step t_1 can be expressed as

$$\mathbf{s_{w,1}} = \mathbf{s_{w,0}} + \mathbf{\Delta s_w}, \tag{4.3}$$

with

$$\begin{aligned} \mathrm{E}\left(\mathbf{s_{w,1}}\right) &= \mathrm{E}\left(\mathbf{s_{w,0}}\right) + \mathrm{E}\left(\mathbf{\Delta s_w}\right), \\ \mathrm{Var}\left(\mathbf{s_{w,1}}\right) &= \mathrm{Var}\left(\mathbf{s_{w,0}}\right) + \mathrm{Var}\left(\mathbf{\Delta s_w}\right). \end{aligned}$$

We apply a logit transformation on $\widehat{\mathbf{s}}_{\mathbf{w,1}} = \widehat{\mathbf{s}}_{\mathbf{w,0}} + \mathbf{\Delta}\widehat{\mathbf{s}}_{\mathbf{w}}$ to ensure that the predictor is in the interval $[0, 1]$.

The synthetic seismograms are computed by the forward model in Expression 3.8. The seismic signal is modeled with three angle stacks $\theta = (0, 15, 30)^\circ$ and a 25 Hz Ricker wavelet in the convolution model. The synthetic model for $\mathbf{d}^\theta$ is on the form

$$\begin{aligned} \mathbf{d}^\theta &= \mathbf{WADBr} + \boldsymbol{\varepsilon}_{\mathbf{d|r}}, \\ \boldsymbol{\varepsilon}_{\mathbf{d|r}} &= \mathbf{W}\boldsymbol{\epsilon}_{\mathbf{c|m}} + \boldsymbol{\epsilon}_{\mathbf{d|r}}. \end{aligned} \tag{4.4}$$

This is the likelihood model in Expression 3.8 with $\sigma^2_{m|r} = 0$. The corresponding synthetic seismograms with $\boldsymbol{\varepsilon}_{\mathbf{d|r}} = 0$ are displayed in Figure 4.2.

The error term $\boldsymbol{\varepsilon}_{\mathbf{d|r}}$ is specified through the signal-noise ratio (SNR) which gives the fraction of signal to error. There are different definitions of the signal-noise ratio in the literature, we define

$$\mathrm{SNR} = \frac{\mathrm{Tr}\left[\mathrm{Var}(\mathbf{WADBr})\right]}{\mathrm{Tr}\left[\mathrm{Var}(\boldsymbol{\varepsilon}_{\mathbf{d|r}})\right]}. \tag{4.5}$$

In the current experiment we make synthetic AVO data sets with additive error corresponding to a signal-noise ratio of 10^4, 5 and 2 (Case I, II and III respectively). The synthetic seismic survey with SNR=2 represent poor quality seismic and the survey with SNR=5 mimic good quality seismic. A synthetic data set with SNR=10^4 is also made in order to examine the model performance when the error approaches zero. In a seismic survey the signal-noise ratio is unknown and should be estimated by an educated guess in the

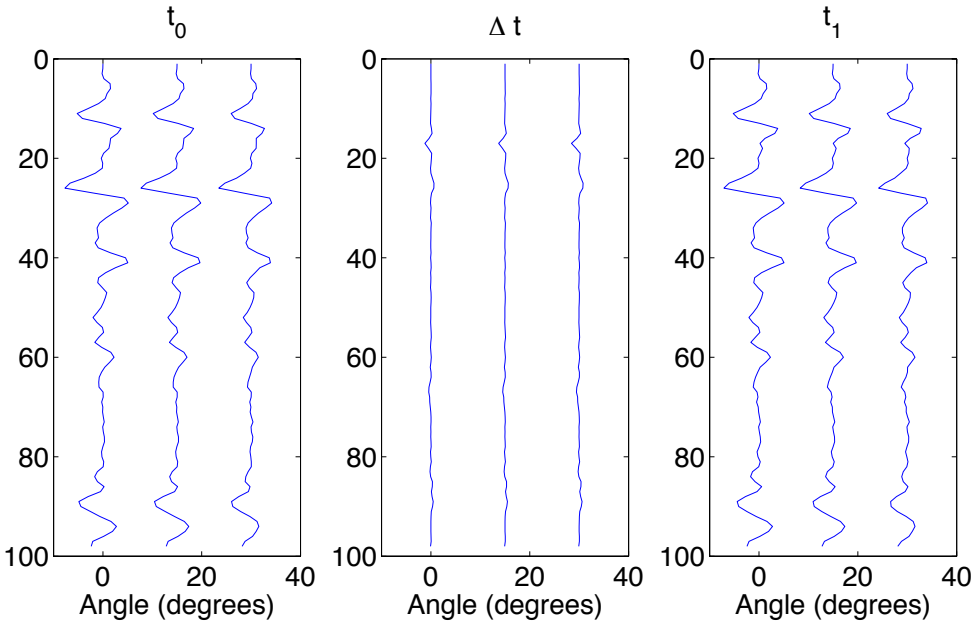

Figure 4.2: AVO signal

inversion model. In Subsection 4.5.1 we examine to what extent the posterior model is influenced by an underspecification of the error in the seismic gather. In Appendix A we have included more test runs where we over and under specify the error in the inversion model. An overview of the different model setups tested is listed in Table 4.1.

		Inversion Model			
	SNR	2	5	20	10^4
Synthetic Model	2	x	A	A	
	5	A	x	A	
	20	A	A	A	
	10^4				x

Table 4.1: An x indicate that the model is displayed and discussed in this chapter. The model setups that are marked with an A are displayed in Appendix A.

The complete solution is given by the posterior distribution developed for the individual priors in Section 3.2, 3.3 and 3.4. In the following the inversion results are represented graphically by the posterior predictor $[\widehat{\mathbf{r}|\mathbf{d}^{\theta}}]$ together with the 95% confidence interval and the synthetic earth profile that we are trying to restore, see for example Figure 4.3. We also list the root-mean-square error for the different model setups, which is a measure of the difference between the predictor and the reference profile.

$$\text{RMSE} = \sqrt{\frac{1}{T}\sum_{i=1}^{T}\left[\left(\hat{r}_j - \frac{1}{T}\sum_{k=1}^{T}\hat{r}_k\right) - \left(r_j - \frac{1}{T}\sum_{k=1}^{T}r_k\right)\right]^2}. \tag{4.6}$$

It is important to note that since the forward operator $\mathbf{G} = \mathbf{WADB}$ contains the difference operator $\mathbf{D}$, all constant terms in the underlying profile $\mathbf{r}$ are unidentifiable. Hence, we will not be able to estimate the level of the reservoir variables, only its variation and change in magnitude. The predictor will therefore always replicate the mean level in the prior. This should be taken into consideration when evaluating the inversion result.

4.2 Gaussian prior case

In the Gaussian prior model we impose the following structure on the covariance matrix

$$\text{Var}\begin{bmatrix}\boldsymbol{\phi}\\ \mathbf{s_{w,0}}\\ \Delta\mathbf{s_w}\end{bmatrix} = \begin{bmatrix} 1\boldsymbol{\Sigma}_{\boldsymbol{r}}^{\boldsymbol{\nu}} & -0.3\boldsymbol{\Sigma}_{\boldsymbol{r}}^{\boldsymbol{\nu}} & 0\mathbf{I}_T \\ -0.3\boldsymbol{\Sigma}_{\boldsymbol{r}}^{\boldsymbol{\nu}} & 1\boldsymbol{\Sigma}_{\boldsymbol{r}}^{\boldsymbol{\nu}} & 0\mathbf{I}_T \\ 0\mathbf{I}_T & 0\mathbf{I}_T & 0.2\boldsymbol{\Sigma}_{\boldsymbol{r}}^{\boldsymbol{\nu}} \end{bmatrix}. \tag{4.7}$$

The numerical values in the covariance matrix are with respect to a logit transformation on the porosity and water saturation. The marginal prior models and the inversion results for the Gaussian prior case are shown in Figure 4.3, 4.4 and 4.5. We observe that the prior model distribution for the porosity is skewed and that the distribution for the water saturation has heavier tails than the standard Gaussian distribution. The reason that the prior models display non-Gaussian behavior is that the prior models are defined with respect to the logit transformed variables, while it is the untransformed variables that are depicted. A test run with $SNR = 10^4$ in the synthetic and inversion model is shown in Figure 4.3. This setup is referred to as Case I. The figure shows that in the presence of negligible error, the synthetic earth profile is estimated almost perfectly by the predictor with corresponding narrow confidence intervals.

In Figure 4.4 and 4.5, more error is added to the synthetic seismogram to mimic a real seismic survey. The accuracy for the porosity and change in water saturation predictor is similar to in Case I. The confidence intervals for the porosity and change in water saturation also remain fairly stable with increasing error. The predictor for the water saturation on the other hand regress increasingly towards the mode of the prior as the signal-noise ratio decreases. From the $s_{w,0}$ profile in Figure 4.4 and 4.5 it is clear that under realistic error levels the posterior predictor for the water saturation is less informative. The confidence bounds for the water saturation are also very wide compared to the confidence bounds for the porosity and change in water saturation. We see that the uncertainty in the water saturation profile increases drastically from Case I to Case II, and it seems like all the error in the model is contributed to the water saturation variable.

In Table 4.2 we list the root-mean squared error and in Table 4.3 the relative decrease in mean variance from the prior to the posterior model is displayed. From both the tables we deduce that the water saturation is very sensitive to a decrease in the signal-noise ratio, while the inversion results for the porosity

and change in water saturation remain relatively stable with increasing model error.

SNR	$\boldsymbol{\phi}$	$\mathbf{s_{w,0}}$	$\boldsymbol{\Delta}\mathbf{s_w}$	$\mathbf{s_{w,1}}$
10^4	0.01	0.02	0.02	0.02
5	0.01	0.17	0.05	0.17
2	0.02	0.17	0.09	0.15

Table 4.2: Root mean square error

SNR	$\boldsymbol{\phi}$	$\mathbf{s_{w,0}}$	$\boldsymbol{\Delta}\mathbf{s_w}$
10^4	0.95	0.95	0.95
5	0.89	0.40	0.94
2	0.86	0.27	0.90

Table 4.3: Relative decrease in mean variance from prior model to posterior model

The benefit of using a Gaussian prior model is that the inversion is done jointly for all dimensions of $\mathbf{r}$. The methodology can therefore be applied to large data sets without having to use extensive amounts of computational effort. The disadvantage of using the Gaussian prior model setup is that the predictor does not acknowledge the bimodal nature of $s_{w,0}$ and when the signal-noise ratio decrease, the predictor for this variable will tend to regress towards the mode of the prior. When evaluating the posterior distribution, we also have to find $\boldsymbol{\Sigma}_{\mathbf{d}}^{-1} \in \mathbb{R}^{3T\times 3T}$. This operation is costly if T is very large and the matrix also has to be positive definite. However, as the Gaussian prior model is a very common setting for inverse problems, the issues mentioned above have been thoughtfully studied.

GAUSSIAN PRIOR CASE

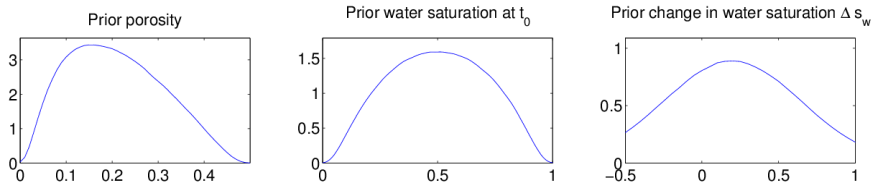

Synthetic earth profile made with SNR=10^4
Inversion model with SNR=10^4

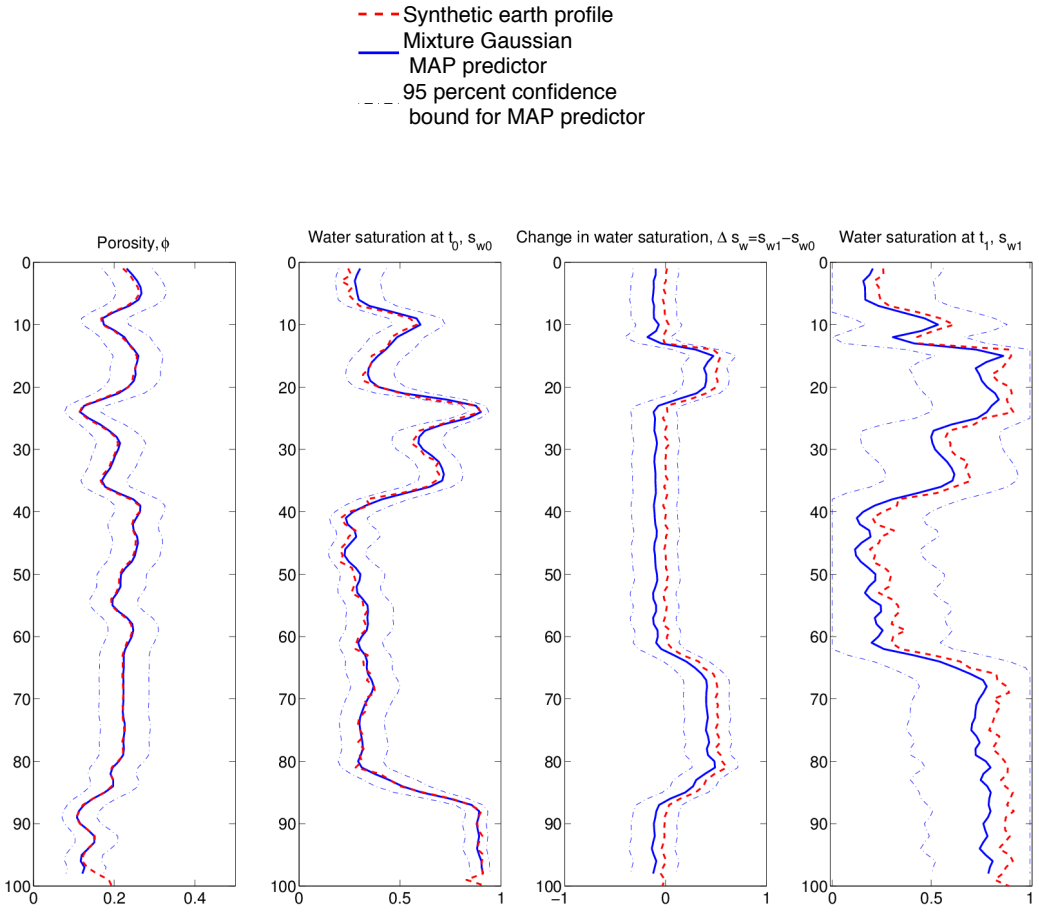

Figure 4.3: Gaussian prior model, Case I

GAUSSIAN PRIOR CASE

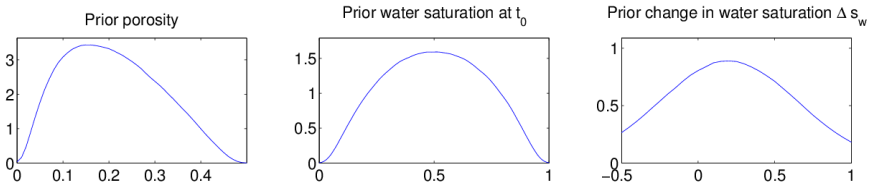

Synthetic earth profile made with SNR=5
Inversion model with SNR=5

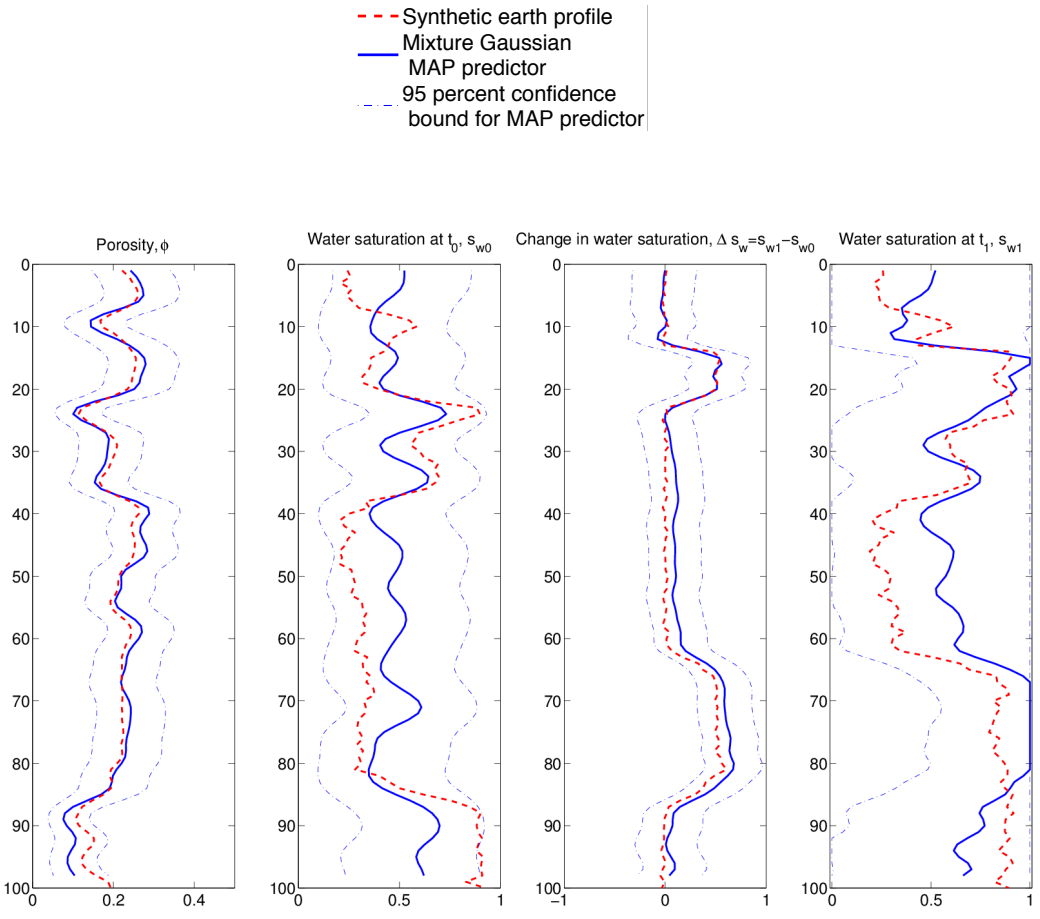

Figure 4.4: Gaussian prior model, Case II

GAUSSIAN PRIOR CASE

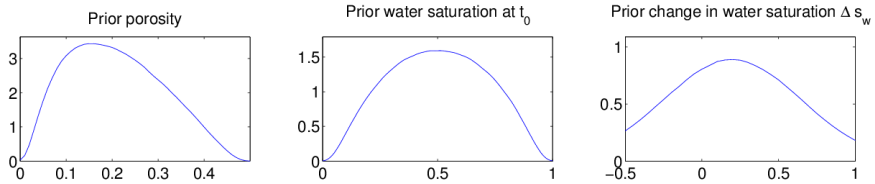

Synthetic earth profile made with SNR=2
Inversion model with SNR=2

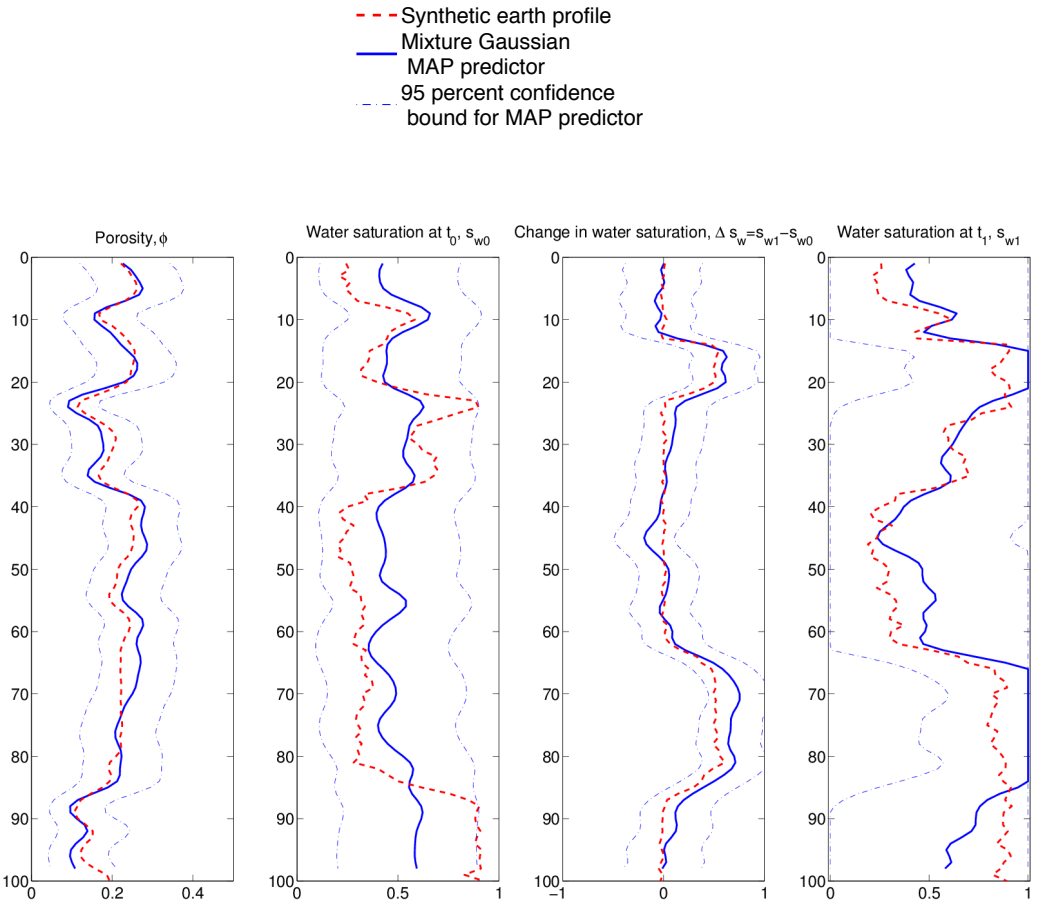

Figure 4.5: Gaussian prior model, Case III

4.3 Mixture Gaussian prior case

We let $\pi \in \Omega_\pi = \{0, 1\}$ with $p(0) = p(1) = 0.5$ and

$$\boldsymbol{\mu}_{\mathbf{r}|\boldsymbol{\pi}=0\mathbf{i}_\mathbf{T}} = \begin{bmatrix} 0.2\mathbf{i}_T \\ 0.2\mathbf{i}_T \\ 0\mathbf{i}_T \end{bmatrix}, \quad \boldsymbol{\mu}_{\mathbf{r}|\boldsymbol{\pi}=1\mathbf{i}_\mathbf{T}} = \begin{bmatrix} 0.2\mathbf{i}_T \\ 0.8\mathbf{i}_T \\ 0.5\mathbf{i}_T \end{bmatrix},$$

$$\boldsymbol{\Sigma}_{\mathbf{r}|\boldsymbol{\pi}=0\mathbf{i}_\mathbf{T}} = \boldsymbol{\Sigma}_{\mathbf{r}|\boldsymbol{\pi}=1\mathbf{i}_\mathbf{T}} = \begin{bmatrix} 1\boldsymbol{\Sigma}_{\boldsymbol{r}}^{\boldsymbol{\nu}} & -0.3\boldsymbol{\Sigma}_{\boldsymbol{r}}^{\boldsymbol{\nu}} & 0\mathbf{I}_T \\ -0.3\boldsymbol{\Sigma}_{\boldsymbol{r}}^{\boldsymbol{\nu}} & 3\boldsymbol{\Sigma}_{\boldsymbol{r}}^{\boldsymbol{\nu}} & 0\mathbf{I}_T \\ 0\mathbf{I}_T & 0\mathbf{I}_T & 0.2\boldsymbol{\Sigma}_{\boldsymbol{r}}^{\boldsymbol{\nu}} \end{bmatrix}. \tag{4.8}$$

The marginal prior models and the inversion results for the mixture Gaussian prior case is shown in Figure 4.6, 4.7 and 4.8. The two modes in the bimodal prior for the water saturation are very close to the boundaries of 0 and 1 because of the inverse logit transformation. The change in water saturation is also modeled with two local modes in the prior model. However, since the variance for the change in water saturation is high compared to the distance between the two modes, the prior model density function appear unimodal with heavy tails.

The inversion results for Case I with SNR=10^4 in the synthetic and inversion model is displayed in Figure 4.6. We see that the predictor is not able to perfectly predict the synthetic earth profile even when the error is negligible. This is not surprising as we have imposed an approximate likelihood model.

The inversion results for model setups with the realistic signal-noise ratios of 5 and 2 are shown in Figure 4.7 and 4.8 respectively. We see that the predictor identify the general trend in the profiles even when the amount of error added to the synthetic seismogram is large. Since the prior is bimodal, the predictor for $s_{w,0}$ does not tend towards the median of the prior model like in the Gaussian case. Instead, the predictor will tends to flip between the two modes as the error in the model increases. In the current prior model setup we inhibit this effect by imposing a strong spatial correlation in the prior model.

For $s_{w,0}$, especially, the confidence intervals are very wide under the mixture Gaussian prior assumption. This is because the posterior model is bimodal and the posterior probabilities for the local maximum that is not the global max is in the range 0.25 to 0.49 for all the variables. The predictor for $[\mathbf{r}|\mathbf{d}]$

is therefore highly uncertain, even when we have a negligible amount of error in the likelihood model as illustrated in Case I. By adding the posterior predictors for $s_{w,0}$ and Δs_w, we get a prediction of the water saturation at t_1. The confidence bounds for $s_{w,1}$ are very wide as we inherit uncertainty from both the prediction of $s_{w,0}$ and Δs_w.

In Table 4.4 we list the root-mean squared error and in Table 4.5 the relative decrease in mean variance from the prior to the posterior model is displayed. We see that the RMSE is fairly stable with decreased signal-noise ratio, which coincide with the conclusion from the discussion above.

SNR	$\boldsymbol{\phi}$	$\mathbf{s_{w,0}}$	$\mathbf{\Delta s_w}$	$\mathbf{s_{w,1}}$
10^4	0.01	0.08	0.04	0.10
5	0.02	0.10	0.06	0.12
2	0.02	0.14	0.11	0.22

Table 4.4: Root-mean-square error

SNR	$\boldsymbol{\phi}$	$\mathbf{s_{w,0}}$	$\mathbf{\Delta s_w}$
10^4	0.95	0.46	0.76
5	0.91	0.33	0.75
2	0.85	0.21	0.72

Table 4.5: Relative decrease in mean variance from prior model to posterior model

When assessing the posterior distribution, we have to find $\Sigma^{-1}_{\mathbf{d}|\pi} \in \mathbb{R}^{3T\times 3T}$ for $j = 1, \ldots, T$. This operation is costly if T is very large. When implementing the method in higher dimensions we should therefore investigate the possibility of making some simplifying assumptions in order to reduce the computational time of the inversion step. We also have to evaluate $p(\mathbf{d}|\pi)$ for $j = 1, \ldots, T$ which requires that $\Sigma_{\mathbf{d}|\pi}$ is positive definite. In the current simulation study, the inversion is done very efficiently and the methodology is very fast compared to algorithms which relies on sampling.

MIXTURE GAUSSIAN PRIOR CASE

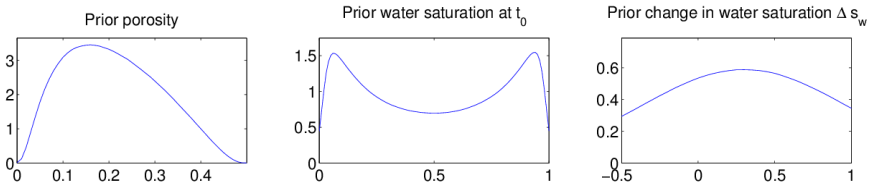

Synthetic earth profile made with SNR=10^4
Inversion model with SNR=10^4

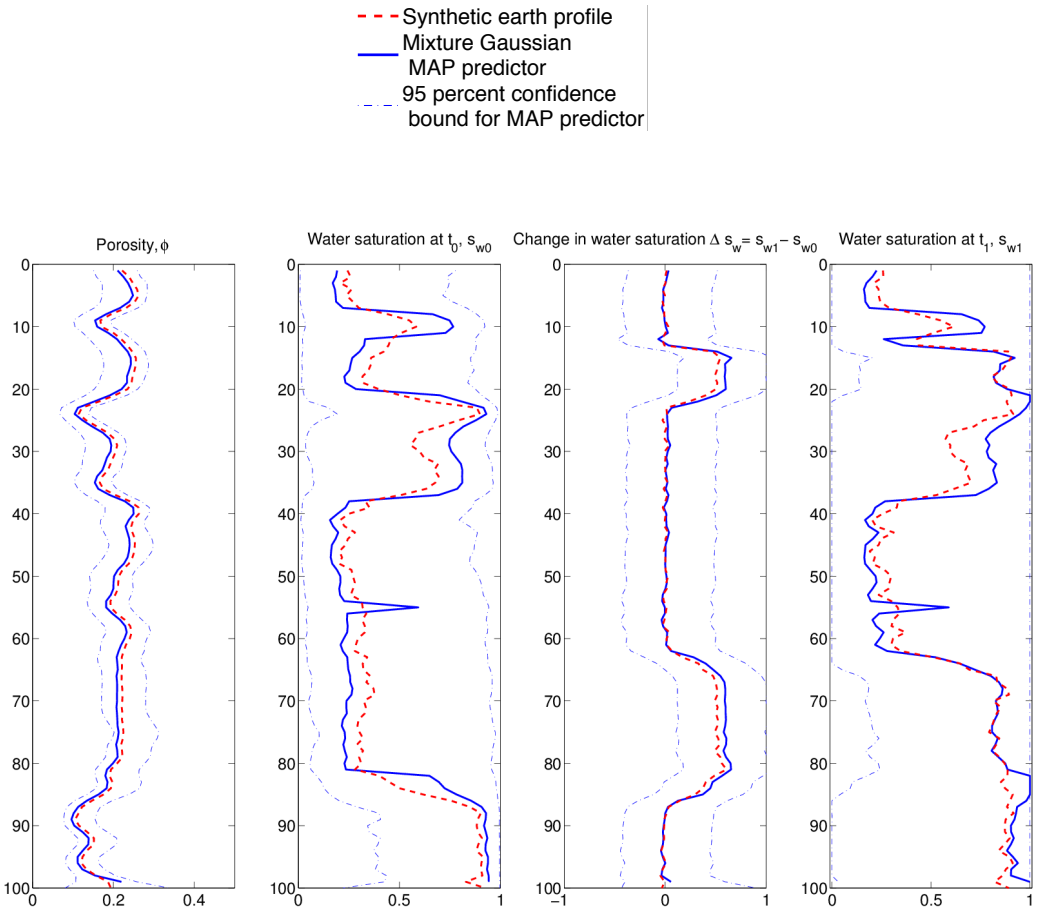

Figure 4.6: Mixture Gaussian prior model, Case I

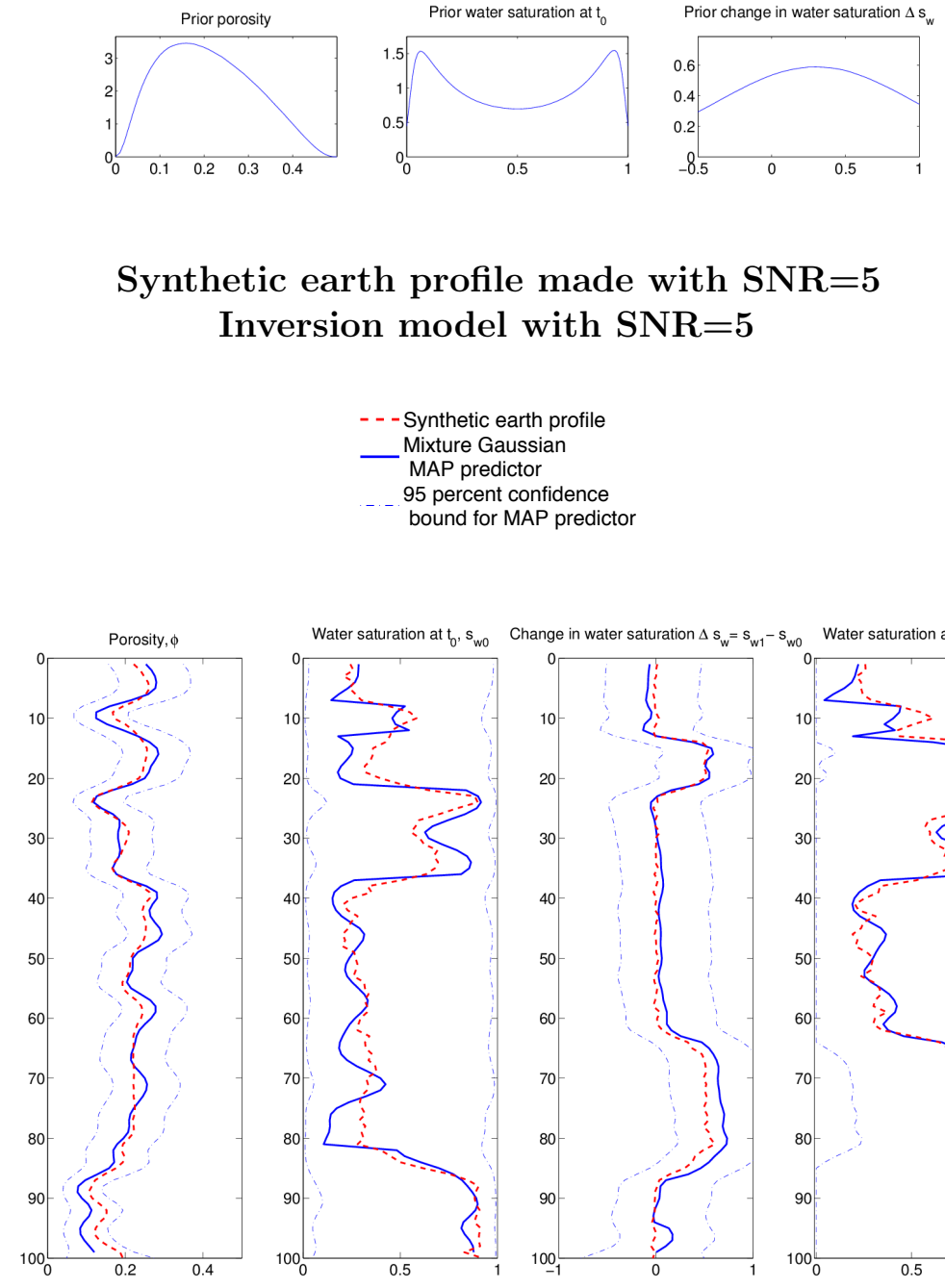

Figure 4.7: Mixture Gaussian prior model, Case II

MIXTURE GAUSSIAN PRIOR CASE

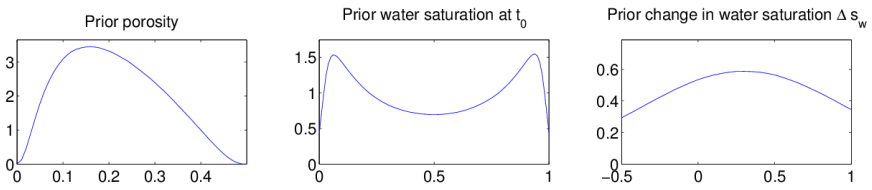

Synthetic earth profile made with SNR=2
Inversion model with SNR=2

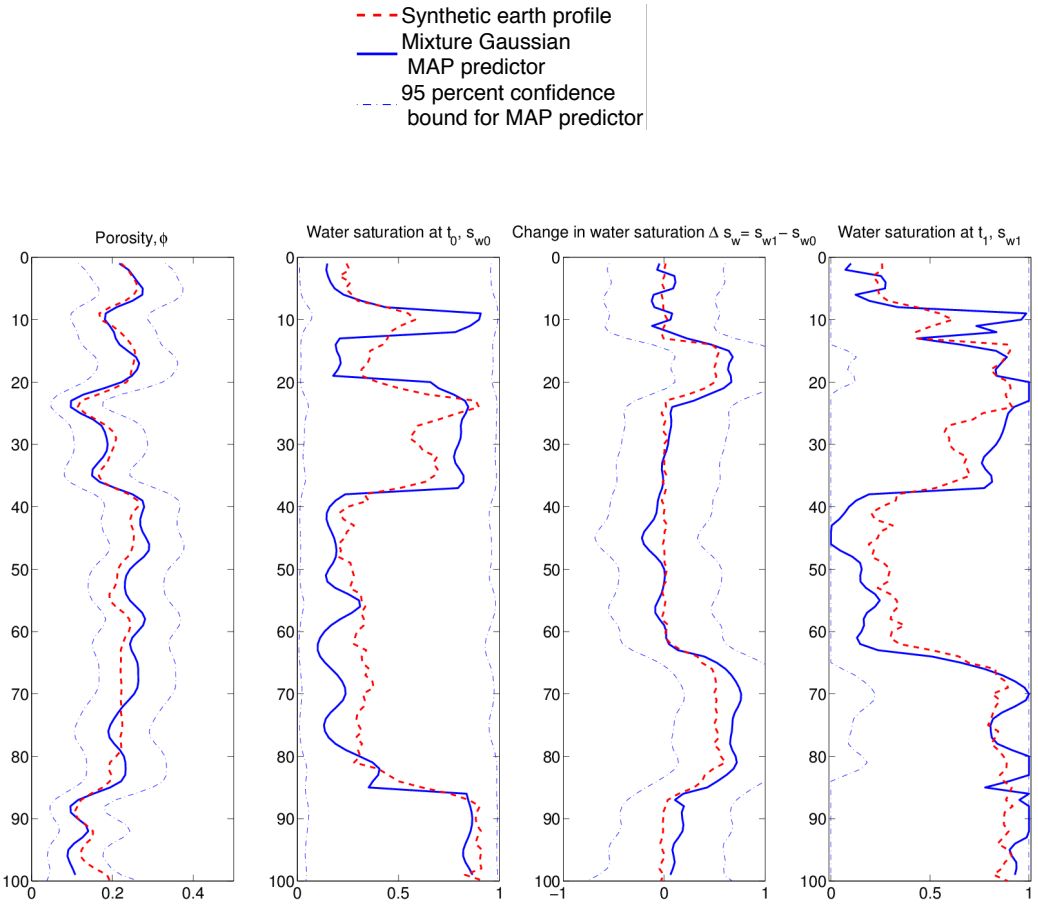

Figure 4.8: Mixture Gaussian prior model, Case III

4.4 Generalized Gaussian prior case

In the generalized Gaussian prior model we assign the following structure on the covariance matrix for $\tilde{\mathbf{r}}$

$$\mathbf{\Sigma}_{\tilde{\mathbf{r}}} = \begin{bmatrix} 1\mathbf{\Sigma}_{\boldsymbol{r}}^{\boldsymbol{\nu}} & -0.3\mathbf{\Sigma}_{\boldsymbol{r}}^{\boldsymbol{\nu}} & 0\mathbf{I}_T \\ -0.3\mathbf{\Sigma}_{\boldsymbol{r}}^{\boldsymbol{\nu}} & 3\mathbf{\Sigma}_{\boldsymbol{r}}^{\boldsymbol{\nu}} & 0\mathbf{I}_T \\ 0\mathbf{I}_T & 0\mathbf{I}_T & 0.2\mathbf{\Sigma}_{\boldsymbol{r}}^{\boldsymbol{\nu}} \end{bmatrix}. \tag{4.9}$$

and the coupling coefficients and selection sets are listed in Table 4.6.

	γ	A_i
ϕ	0.45	$(-\infty, \infty)$
s_w	0.45	$(0.2 - \mu_{s_{w,0}}, 0.4 - \mu_{s_{w,0}}) \cup (0.6 - \mu_{s_{w,0}}, 0.8 - \mu_{s_{w,0}})$
Δs_w	0.45	$(-0.05 - \mu_{\Delta s_w}, 0.05 - \mu_{\Delta s_w}) \cup (0.45 - \mu_{\Delta s_w}, 0.55 - \mu_{\Delta s_w})$

Table 4.6: Model parameters for the generalized Gaussian prior model

The marginal prior models and the inversion results for the generalized Gaussian prior case is depicted in Figure 4.9, 4.10 and 4.11. We see that the prior model for the porosity is skewed and that the prior model for the water saturation is bimodal. The prior model density for the change in water saturation is unimodal even though we have defined two selection sets. This is caused by the relatively high variance in the prior model compared to the distance between the two selection sets.

The inversion results for a test run with SNR=10^4 in the synthetic and inversion model is displayed in Figure 4.9. The figure shows that in the presence of negligible error, the reservoir variables are estimated almost perfectly with corresponding narrow confidence intervals. The model error is increased to realistic levels in Figure 4.10 and 4.11. The predictor captures the general trend in the profiles for both signal-noise ratios. By comparing the $s_{w,0}$ profiles in Figure 4.11 and 4.10, we see that the predictors ability to predict the details in the reference profile diminish as the error level in the likelihood model increase. The inversion results for the porosity is not as good as in the Gaussian prior case. This is due to correlation with the water saturation. Another coupling effect is seen in the water saturation profile at $\tau = 55$. Here a rapid change in ϕ induce a spike in $\mathbf{d}$ which then is predicted to originate from s_w.

In Table 4.7 the RMSE is listed and in Table 4.8 we show the relative decrease in mean variance from the prior model. It is apparent that the RMSE and the change in the variances are very stable for the porosity and change in water saturation, while it increases fast for the water saturation at t_0 with decreasing signal-noise ratio.

SNR	$\boldsymbol{\phi}$	$\mathbf{s_{w,0}}$	$\mathbf{\Delta s_w}$	$\mathbf{s_{w,1}}$
10^4	0.02	0.02	0.04	0.03
5	0.02	0.18	0.04	0.21
2	0.02	0.18	0.06	0.20

Table 4.7: Relative decrease in variance from prior model to posterior model

SNR	$\boldsymbol{\phi}$	$\mathbf{s_{w,0}}$	$\mathbf{\Delta s_w}$
10^4	0.94	0.68	0.94
5	0.93	0.54	0.93
2	0.89	0.24	0.92

Table 4.8: Table of relative decrease in variance from prior to posterior model

In order to obtain the posterior predictor we have to go sequentially trough all $r_j \in \mathbf{r}$. However, the optimization we perform in each step require very little computational effort, so the inversion is performed efficiently for our choice of T. Another benefit of using the generalized Gaussian prior model is that the distribution is very flexible, as we can model both skewness, multimodality and heavy tails. We are therefore free to design fairly informative priors without having to resort to MCMC methods.

GENERALIZED GAUSSIAN PRIOR CASE

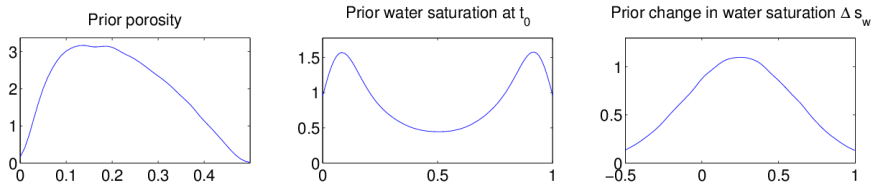

Synthetic earth profile made with SNR=10^4
Inversion model with SNR=10^4

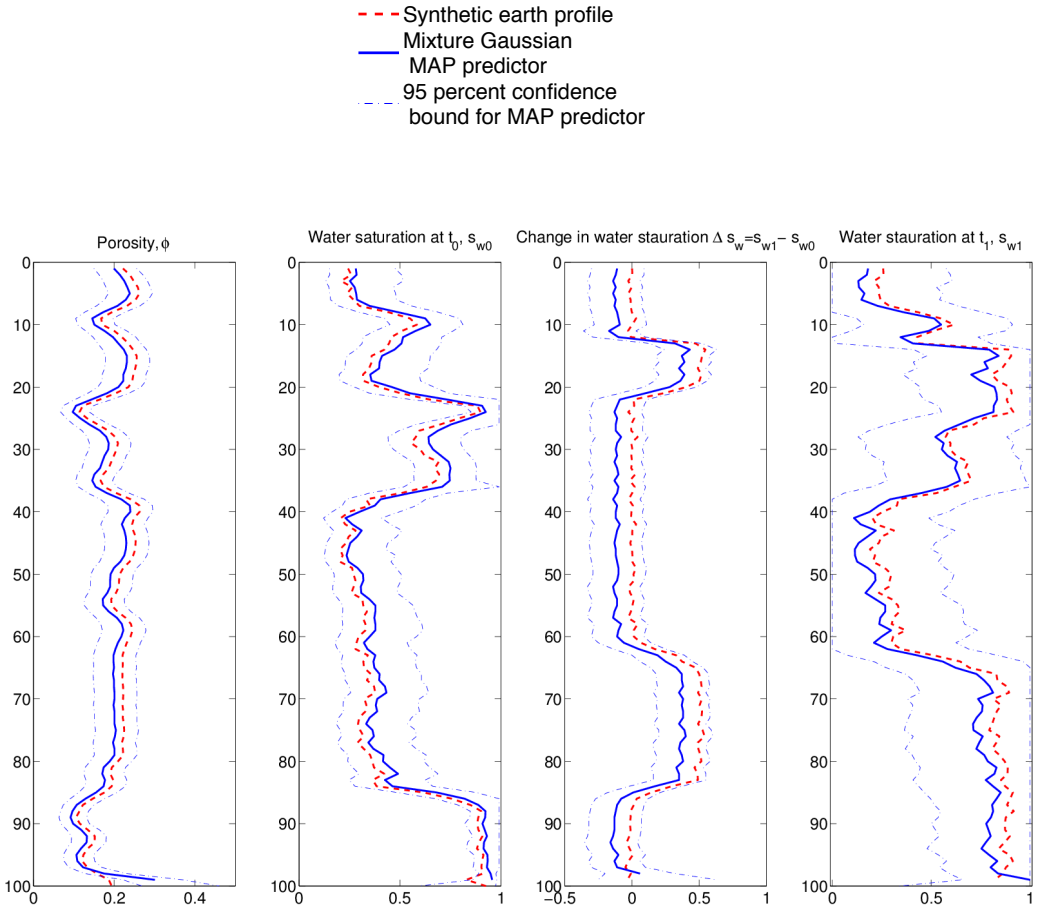

Figure 4.9: Generalized Gaussian prior model, Case I

GENERALIZED GAUSSIAN PRIOR CASE

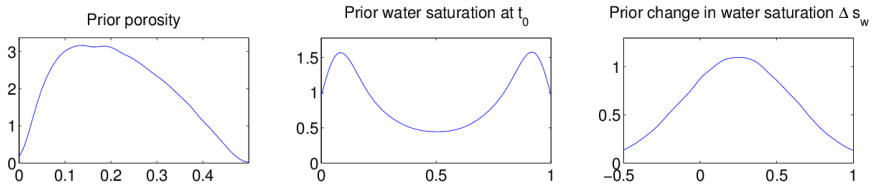

Synthetic earth profile made with SNR=5
Inversion model with SNR=5

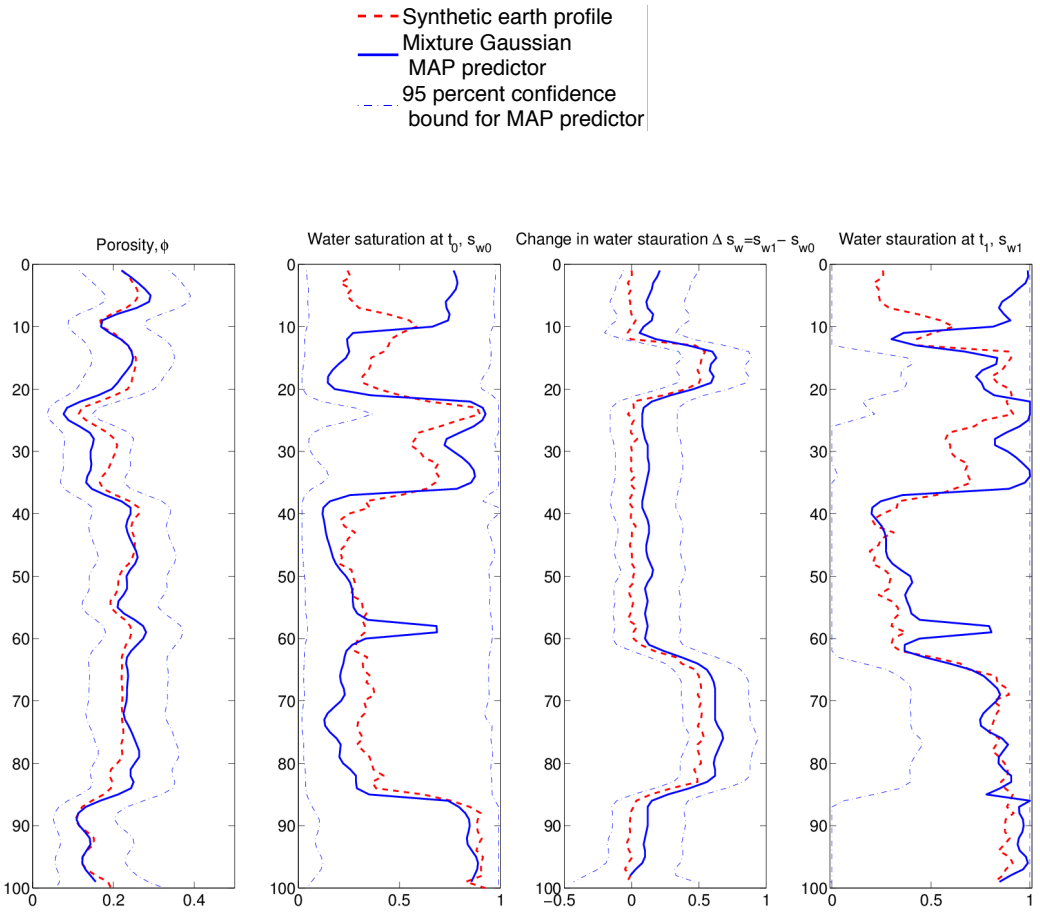

Figure 4.10: Generalized Gaussian prior model, Case II

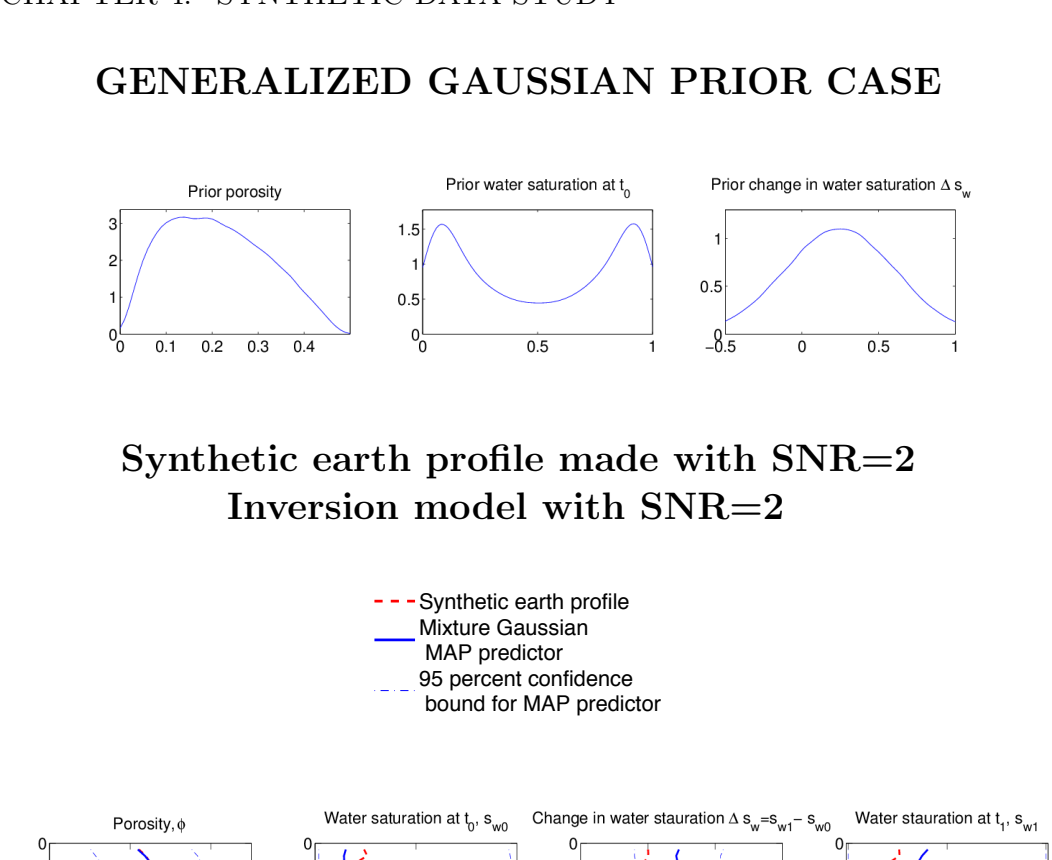

Figure 4.11: Generalized Gaussian prior model, Case III

4.5 Sensitivity study

In the model design we have to specify the model parameters in the prior model and the likelihood model. In this section, we examine to what extent these parameter choices influence the posterior model.

4.5.1 Model sensitivity: Likelihood error

The likelihood model is defined by a deterministic relationship and an error term that describe the structure of the uncertainty in the model. As discussed in Subsection 3.1.1, it is important to impose a realistic error level in the inversion model. If the error is underspecified in the likelihood model, the posterior predictor will often give misleading predictions as the fluctuation caused by error in the data is accredited to the underlying variable. We will not know the error level in a real data case. Therefore it is of interest to know how sensitive the posterior models are to a wrongly specified error level in the likelihood model.

We examine the effect in Figure 4.12, 4.13 and 4.14. Here we have imposed an inversion model with SNR=20, while the synthetic data set is created with SNR=5. We expect that the posterior predictor exaggerate the variability in the reference profile. We assess the effect by comparing Figure 4.12, 4.13 and 4.14 to the inversion model setup with a correct error level in Figure 4.4, 4.7 and 4.10. We observe that the predictor is smoother in the mixture Gaussian and generalized Gaussian prior case. The effect is especially apparent in the $s_{w,0}$ profiles. However, the wrongly specified likelihood models does not make the predictor extensively vague and it still captures the general trend in the profile. The result for the Gaussian posterior model actually shows an improvement in the prediction of $s_{w,0}$ from Figure 4.4 to 4.12. This is because the exaggeration effect draws the predictor away from the prior median.

As an overspecification of the error in the likelihood model will typically not be as large as the one assumed in this simulation study, we conclude that the methods are not extensively sensitive to a wrongly specified error level, which is encouraging. Figures where the amount of error in the inversion model has been overspecified is displayed in Appendix A. In this case, we will lose the inherent accuracy in the predictor.

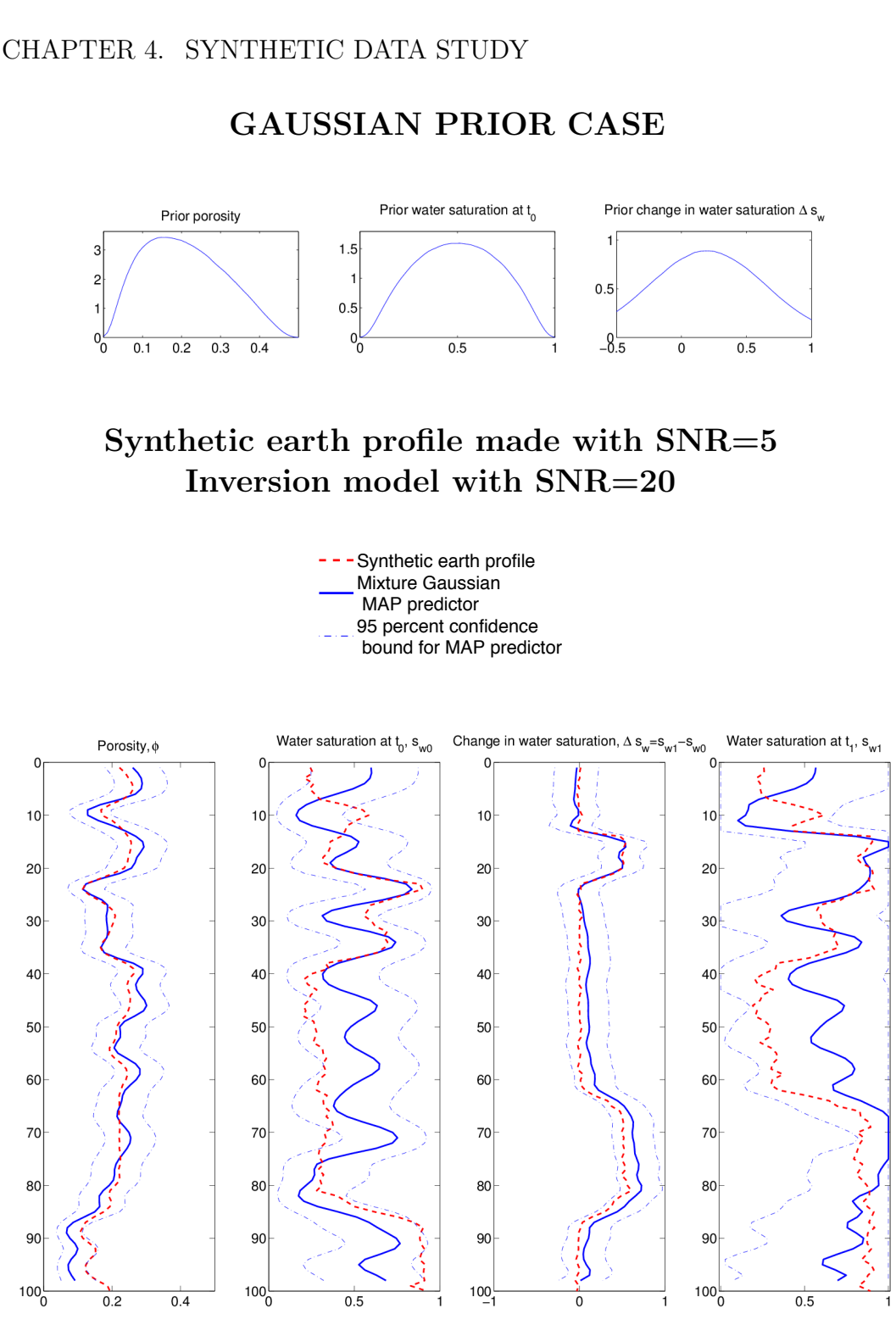

Figure 4.12: Gaussian posterior model sensitivity to underspecification of likelihood model error

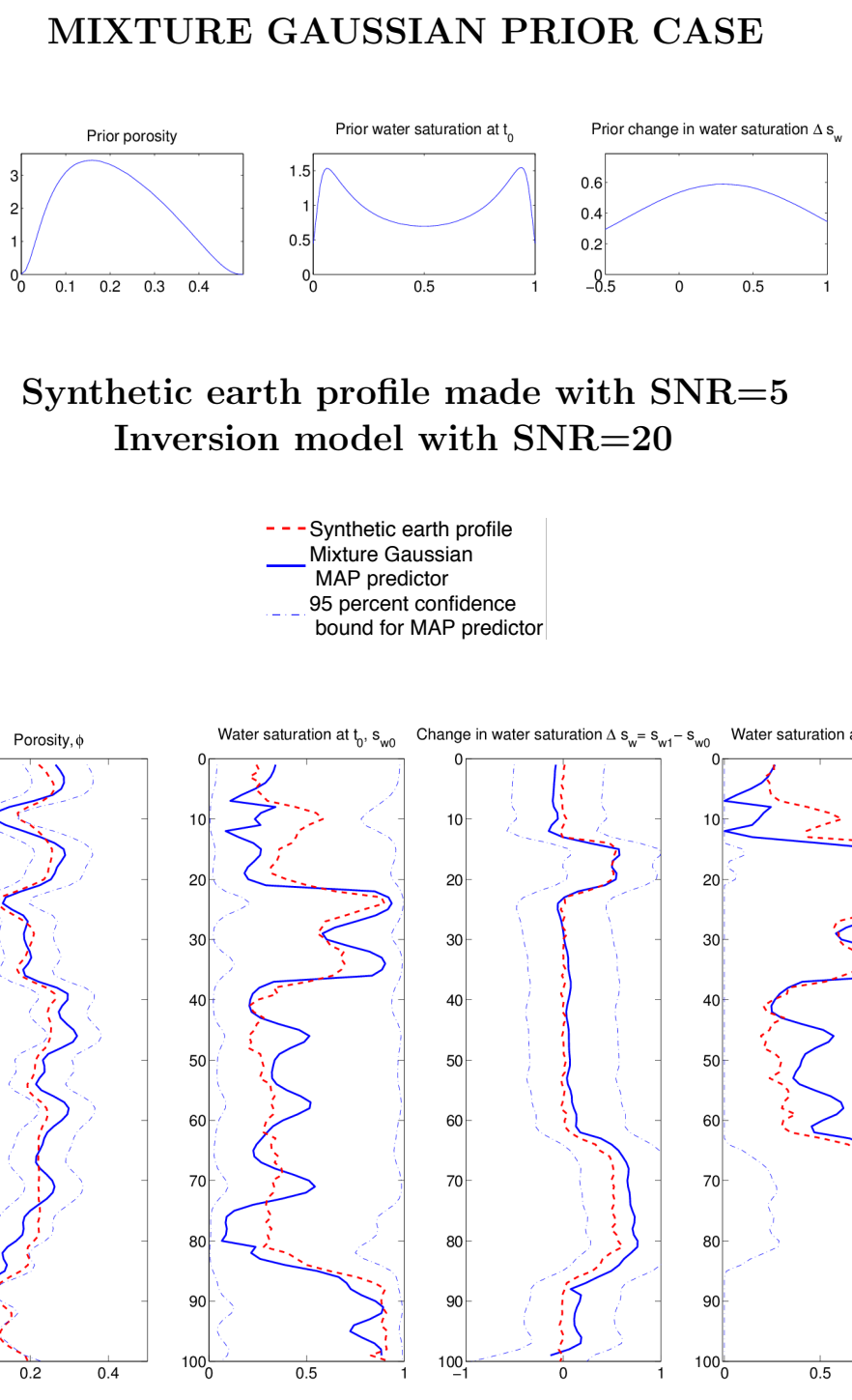

Figure 4.13: Mixture Gaussian posterior model sensitivity to underspecification of likelihood model error

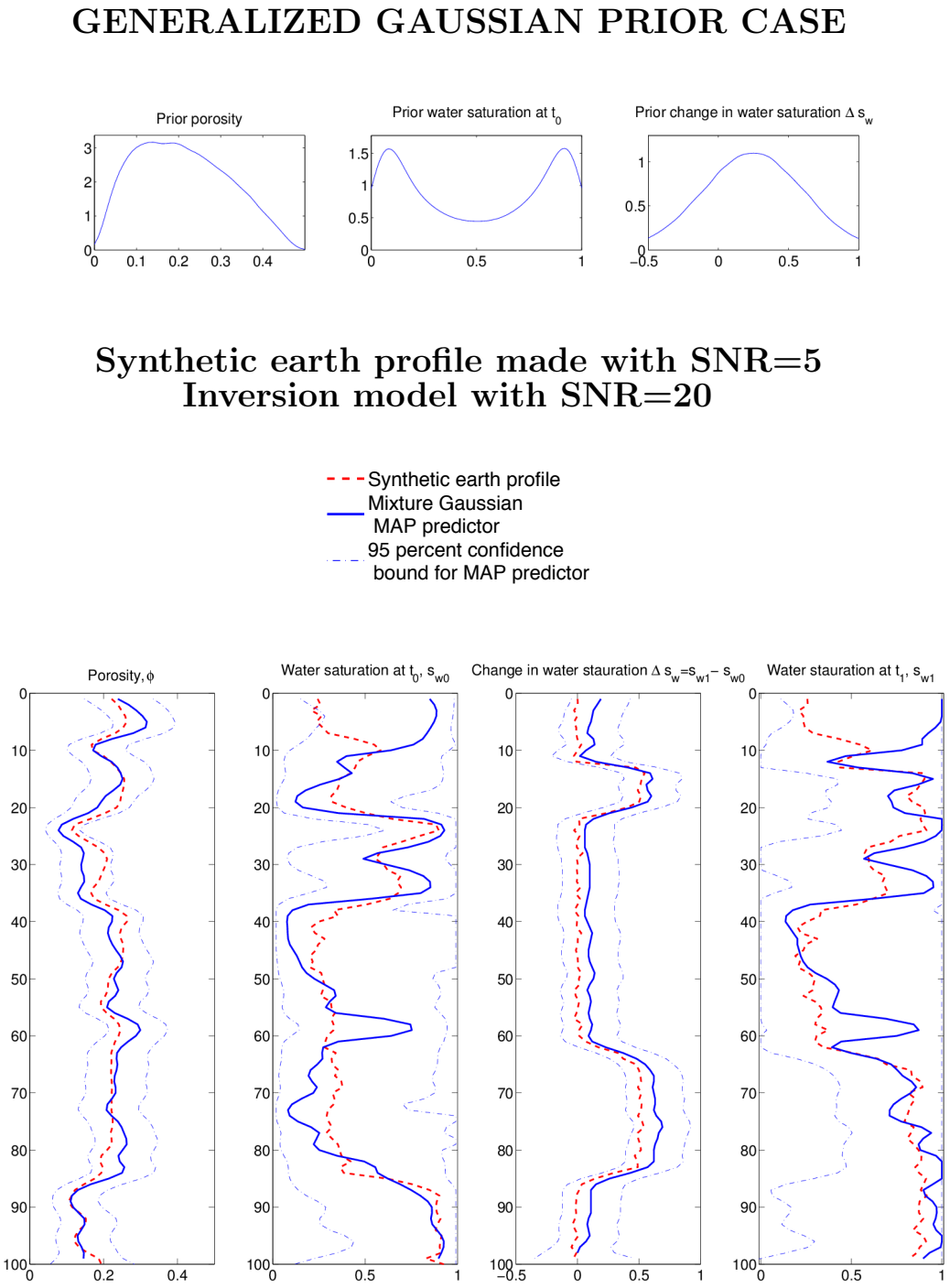

Figure 4.14: Generalized Gaussian posterior model sensitivity to underspecification of likelihood model error

4.5.2 Model sensitivity: Prior correlation length

In the prior models defined in Section 3, we have assigned a spatial correlation structure that is a function of a length scale parameter δ. The parameter is a measure of how rapid the dependency between locations decline and in low signal-noise scenarios, the spatial correlation will indirectly control fluctuations in the predictor. The choice of δ is therefore of importance. The most sensitive variable is the water saturation $s_{w,0}$, so we will focus on the predictors performance for this variable.

In Figure 4.15, 4.17 and 4.19 we have imposed a high spatial dependency in the prior models. The predictor is then a slowly varying smooth function which in the mixture and generalized Gaussian prior case captures the general trend in all the profiles. We then examine to what extent the assumption of small spatial dependence in the prior models influence the predictor. The inversion results are shown in Figure 4.16, 4.18 and 4.20. With small spatial dependency the predictor will vary more rapidly and appear less smooth. By comparing Figure 4.18 and 4.20 we see that it is the predictor for $s_{w,0}$ in the generalized Gaussian posterior model that suffers most with declining δ, but the effect is present for all three models.

It is not easy to know which δ to choose in the prior model. In this study it appears that we get the most accurate results when δ is high. However we can also lose details in the predictor if we impose a very high spatial dependency in the prior model. When performing an inversion study one should therefore test to what extent the length scale influences the inversion result. It is also possible to explore other correlation structures as for example the exponential correlation function. The variance σ_r^2 in the prior model also impacts the posterior model. As with the likelihood model an underspecification of the error in the prior model should be avoided. However, the effect on the predictor caused by a wrongly specified variance in the prior model will usually not be as large as the effect of a wrongly specified variance in the likelihood model. The choice of σ_r^2 is therefore not discussed further in this section.

GAUSSIAN PRIOR CASE

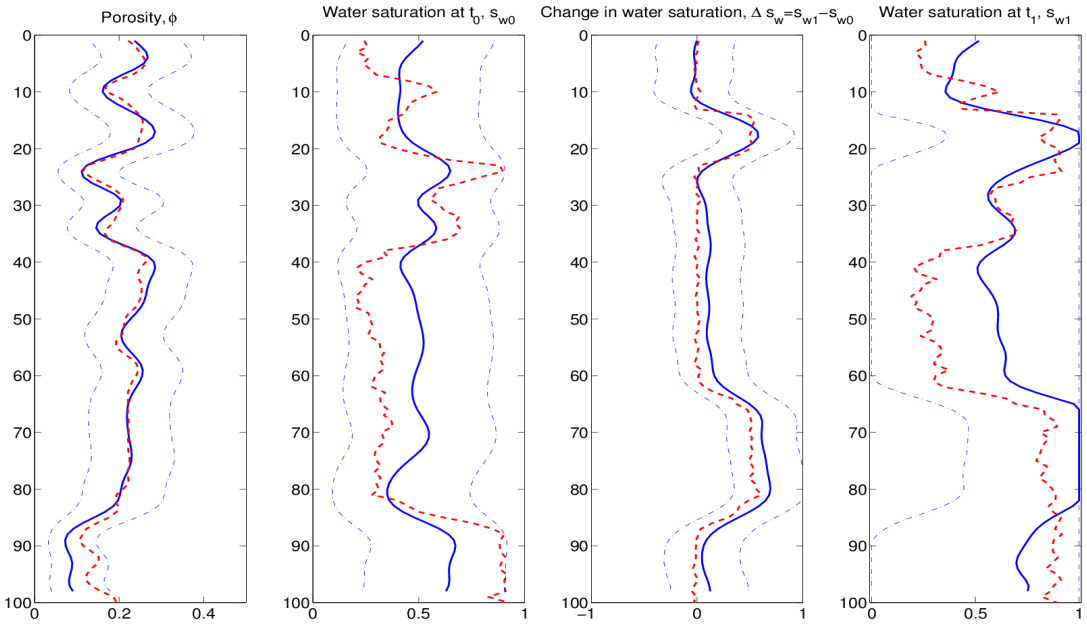

Figure 4.15: $\delta = 7$, Inversion and synthetic model with SNR=5

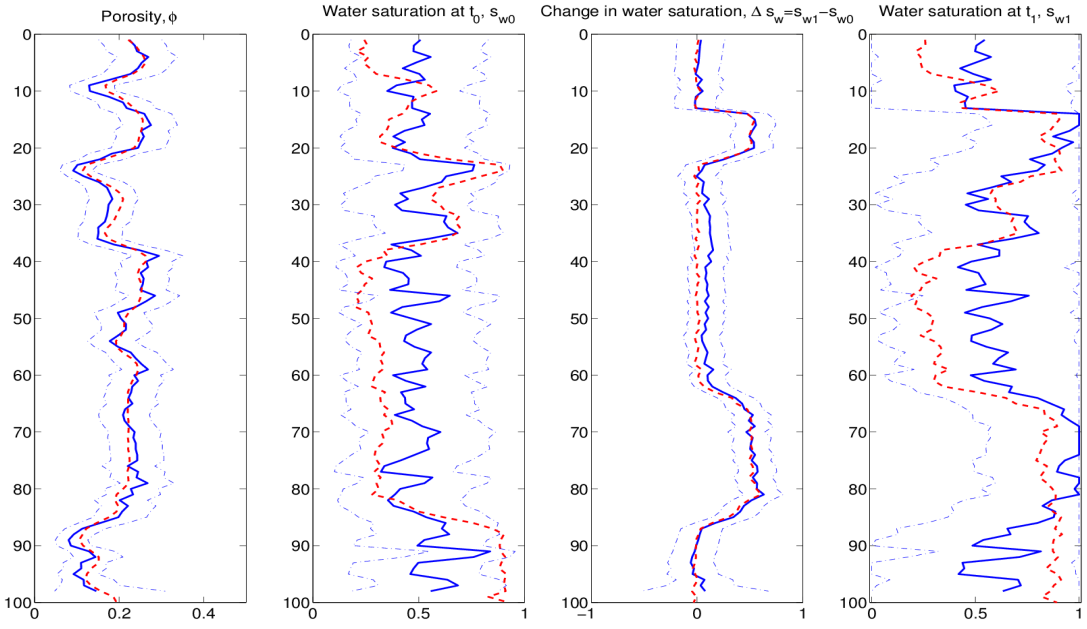

Figure 4.16: $\delta = 1$, Inversion and synthetic model with SNR=5

MIXTURE GAUSSIAN PRIOR CASE

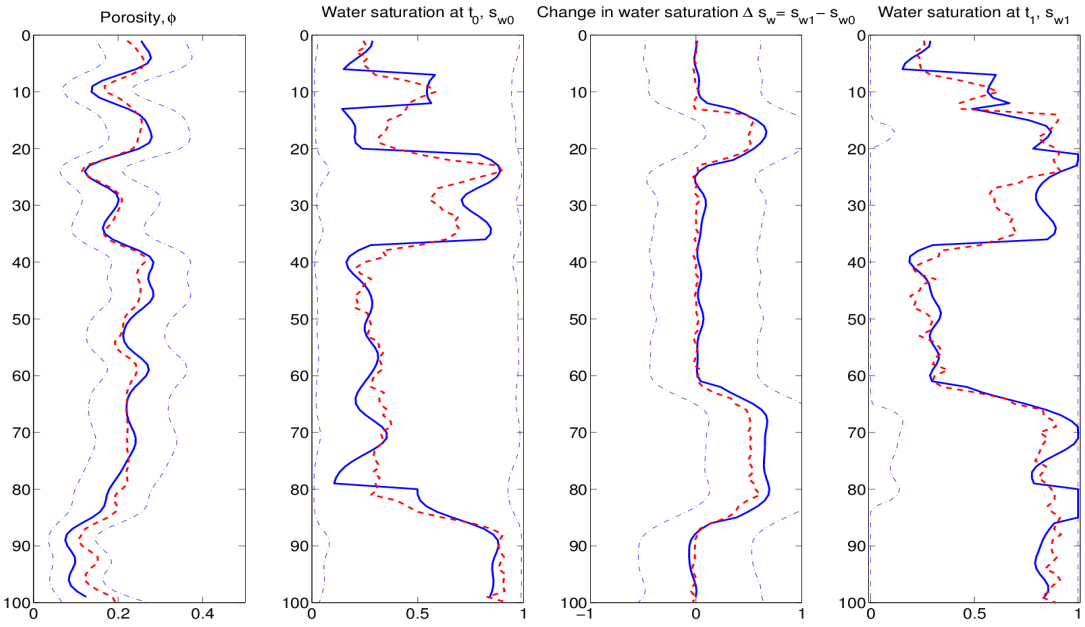

Figure 4.17: $\delta = 7$, Inversion and synthetic model with SNR=5

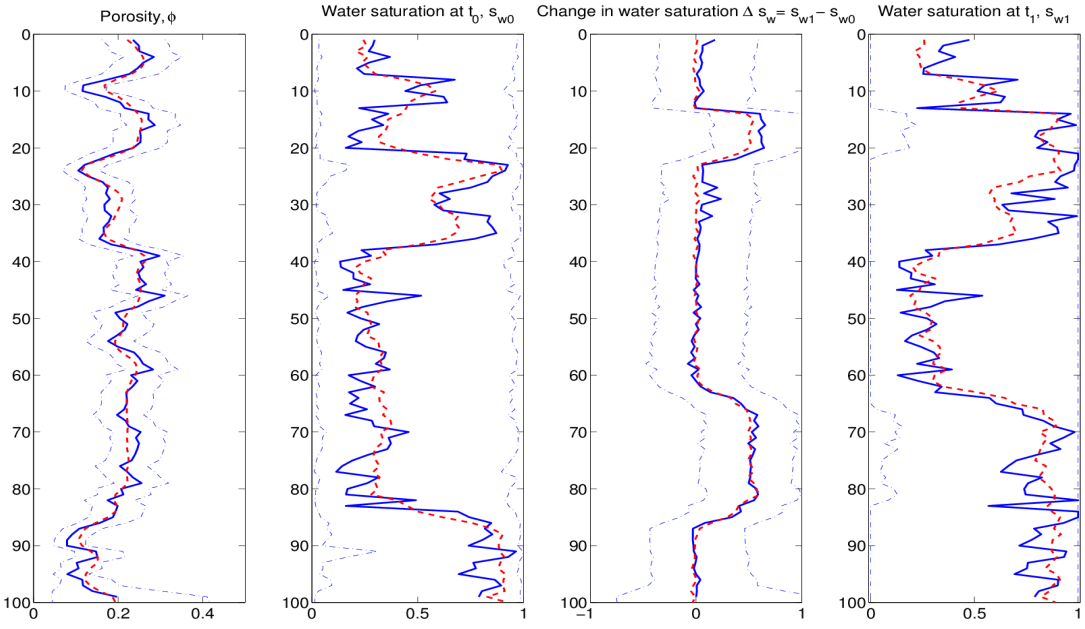

Figure 4.18: $\delta = 1$, Inversion and synthetic model with SNR=5

GENERALIZED GAUSSIAN PRIOR CASE

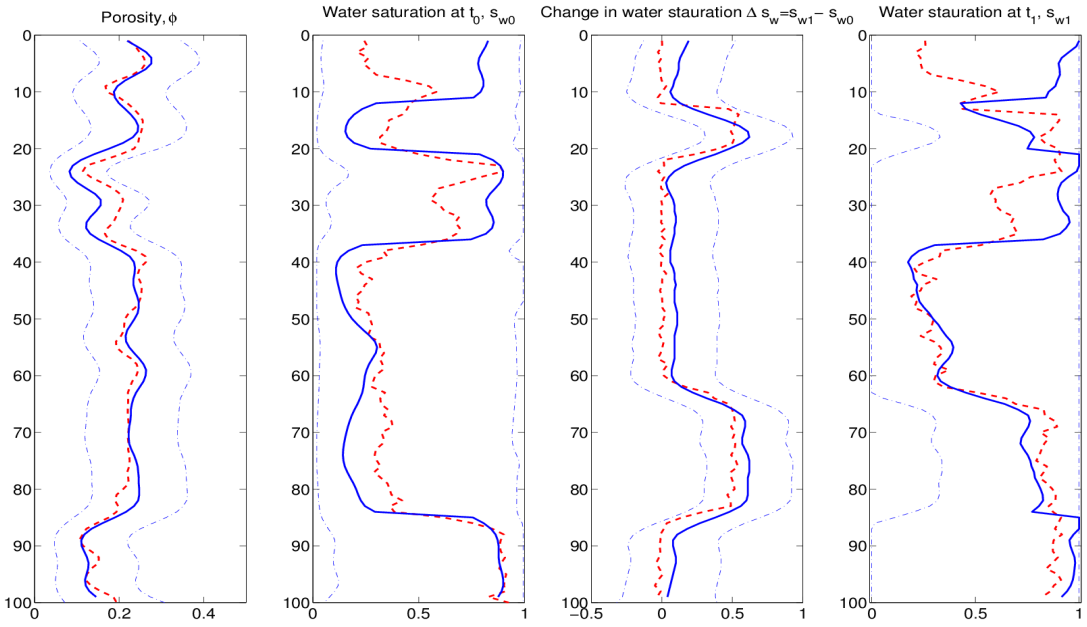

Figure 4.19: $\delta = 7$, Inversion and synthetic model with SNR=5

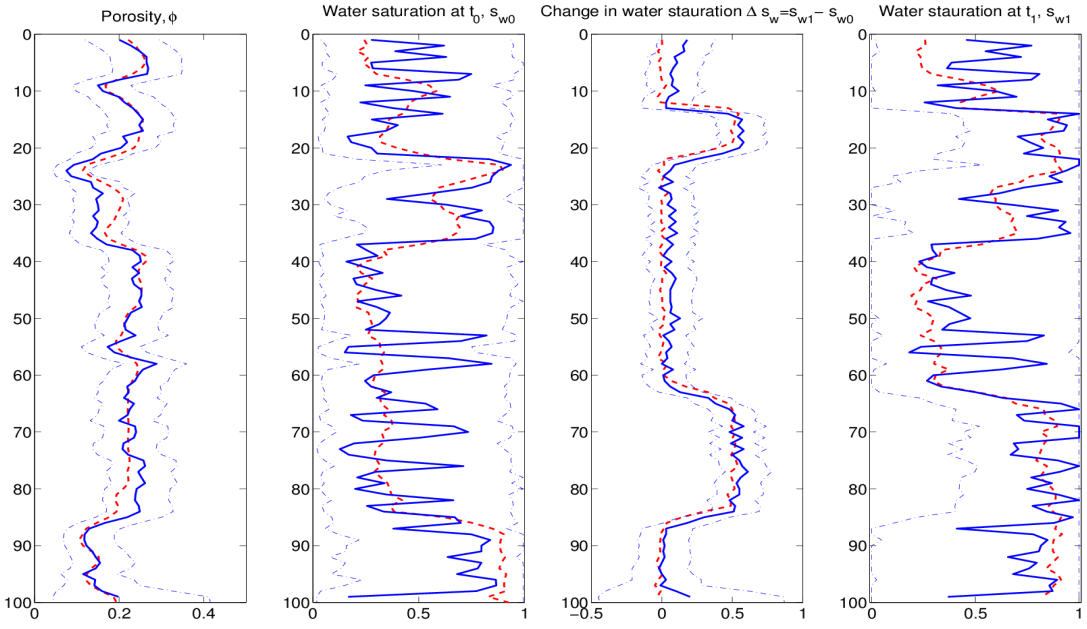

Figure 4.20: $\delta = 1$, Inversion and synthetic model with SNR=5

4.6 Discussion of the posterior models

In Section 3 we introduced a Gauss-linear likelihood model and we developed the posterior models for three prior model settings; a Gaussian prior, a mixture Gaussian prior and a generalized Gaussian prior. In the current section the three prior model setups have been tested on a synthetic data set with respect to the porosity, water saturation, and the change in water saturation between two time steps.

In Case I we imposed negligible error in the synthetic and inversion model. By examining the predictor performance under high signal-noise ratios, we mean to assess the posterior model accuracy. The predictor for the Gaussian and generalized Gaussian model estimate the reference profile almost perfectly. This is also demonstrated by the low root-mean-square error in Table 4.2 and 4.7. Since we have used an approximate likelihood model in the mixture Gaussian prior case, the mixture Gaussian posterior model predictor is not able to replicate the reference profile, even when the model error approaches zero. We also see that confidence intervals are very wide in Case I under the mixture Gaussian setup. The confidence bounds for the Gaussian and generalized Gaussian prior on the other hand, are very narrow. The small uncertainty in these predictors is also demonstrated by the result in Table 4.3 and 4.8. Here we see that the mean variance for the Gaussian and generalized Gaussian posterior models is reduced by over 90 percent compared to the variance in the prior model. There is a small difference between the width of the confidence bounds for the water saturation at t_0. This is because we have imposed a somewhat higher variance in the prior model for the generalized Gaussian prior model compared to the Gaussian prior model.

Since the method is developed with application to seismic data in mind, we are interested in the performance at high error levels which are represented by SNR=5 and SNR=2 in the current study. The predictors for all three posterior models estimate the porosity and the change in water saturation fairly accurately. The main difference between the models is found in the water saturation profiles. The reason that the water saturation predictor suffer with increasing error levels is traced back to the slope of the curves in Figure 3.2 to 3.7. Since the regression coefficients for the porosity is 5 to 70 times greater in magnitude than the regression coefficients for the water saturation, the signal in the synthetic seismogram will be most sensitive to the porosity. An increase in uncertainty will therefore affect the water saturation to a much greater extent than the porosity. This is also the reason

why we use the change in the water saturation as our model variable instead of water saturation at time t_1. When comparing the different models, the focus should therefore be on the statistics for the water saturation at t_0.

A comparison of the inversion results under realistic signal-noise ratios shows that the reference profile is reconstructed best in the mixture Gaussian and generalized Gaussian prior model case. The Gaussian posterior model predictor gives little information about the water saturation profile while the posterior predictor in the mixture Gaussian and generalized Gaussian prior model case provides good predictions that captures the general trend in the profile. Common for the mixture Gaussian and generalized Gaussian prior is that we model the water saturation with a bimodal distribution. We conclude that the bimodal prior assumption for the water saturation is the reason for the good inversion results for these two prior models. The bimodality ensures that the predictor does not regress towards the posterior median with decreasing signal-noise ratio.

By comparing Table 4.2, 4.4 and 4.7 we deduce that the root-mean square error is similar for the three different prior model cases. The main difference is the drop in the water saturation RMSE from Case II to Case I under the Gaussian and generalized Gaussian model, compared to the stable water saturation RMSE in the mixture Gaussian prior model setting. The fact that the RMSE is marginally lower in the Gaussian prior model case compared to the generalized Gaussian setup shows us that the RMSE is not an absolute measurement of accuracy and should be used in combination with graphical inspection.

While the confidence bounds remain fairly narrow for the porosity and change in water saturation under all three prior model setups, we see a dramatic increase in the confidence bounds for the water saturation with decreasing signal-noise ratio. This is traced back to the relative size of the regression coefficient for $s_{w,0}$ compared to ϕ. We see that the confidence bounds for the reservoir variables are slightly narrower for the generalized Gaussian setup than in the mixture Gaussian case, however both confidence intervals span almost the entire range of $s_{w,0}$. This is because the posterior model for $s_{w,0}$ also is bimodal as it inherits the general shape of the prior model with two areas of high probability. The predictions are therefore associated with a fair amount of uncertainty in Case II and Case III.

All three inversion methodologies are very computationally efficient and can be used to make inference about the reservoir variables on large seismic data

sets. In the mixture Gaussian and generalized Gaussian prior model case we find the posterior predictor for each $r_j \in \mathbf{r}$ separately, which means that we sequentially go through all the nodes when performing the inversion. We experienced that the mixture Gaussian prior methodology is slightly more computational demanding on its current form as we have to evaluate an inverse for each $j = 1, \ldots, T$. Most of the inversion methodologies found in literature use MCMC approaches which are computer demanding. Seen in this perspective, the results in the current study are encouraging. The analytical form of the posterior models provides computationally efficient inversion methodologies that is very suitable for 2D and 3D seismic data. The extensions of the models to a 2D and 3D setting is straight forward for all three models, although numerical methods may be required to obtain numerical values.

A major simplification used in the current study is the linear likelihood model which is found by linearizing the relationship between the reservoir variables and the seismic variables. Since the rock physics and geophysics models listed in Chapter 2 are empirical models, we get error both from the model and from the regression. In addition, we have inserted numerical values for the static variables in the rock physic model. What is considered as reasonable values for these variables will vary from reservoir to reservoir. If core measurements from the field are available, more accurate regression coefficients could be found empirically as described in Landrø (2001).

In the inversion model we surmise that the regression error and model error is included in the Gaussian error terms. The scope of the error should be evaluated further to decide if this is a reasonable simplification. Also, we assume that the error term is on the form $\mathbf{W}\boldsymbol{\epsilon}_{\mathbf{c}|\mathbf{m}} + \boldsymbol{\epsilon}_{\mathbf{d}|\mathbf{r}}$. A more accurate model is given by $\mathbf{WAD}\epsilon_{\mathbf{m}|\mathbf{r}} + \mathbf{W}\boldsymbol{\epsilon}_{\mathbf{c}|\mathbf{m}} + \boldsymbol{\epsilon}_{\mathbf{d}|\mathbf{r}}$. In this report we conclude that the magnitude of the latter can be seen as insignificant compared to the overall uncertainty in the model.

In a real seismic survey the variation in the amplitude will also be caused by all the reservoir variables, and not just the porosity and the water saturation. The model can however, easily be extended to include additional model variables, but the accuracy in the posterior model will suffer as the number of variables increase. In the current study we have imposed very general prior models. As the mixture Gaussian and generalized Gaussian distribution are flexible distributions that can model several local modes with different weights, we recommend that the parameters in the model should be selected with great care and in collaboration with a skilled geoscientist.

As discussed in Section 4.1, we will not know the exact signal-noise ratio in a real data study. The confidence bounds should therefore be used more as a guide for the range of the variables. For this purpose, a 80% confidence interval might be more illustrative. The uncertainty the posterior models can be reduced by for example conditioning on actual observations. In the mixture and generalized Gaussian prior models we have also used a very high variance for the water saturation variable. Assuming a smaller variance term in the models could be justified, and such an assumption would decrease the variance in the posterior model.

Chapter 5

Conclusion

In the current thesis, inversion methodologies for assessing reservoir properties from time-lapse seismic data are presented. The inversion problem is cast in a Bayesian framework, and we compare and contrast three prior model settings; a Gaussian prior, a mixture Gaussian prior and a generalized Gaussian prior. By combining the priors with the Gauss-linear likelihood model, we obtain the explicit expressions for the posterior models. Since the posterior models, or reliable approximations of the posterior models, are on analytical form, they provide very computationally efficient inversion methodologies. The three methods are tested on a synthetic data set with respect to porosity, water saturation, and change in water saturation between two time steps.

In the presence of negligible error, the predictor for the Gaussian and generalized Gaussian model estimate the reference profile almost perfectly. Since we have used an approximate likelihood model in the mixture Gaussian prior case, the mixture Gaussian predictor does not replicate the reference profile with this kind of precision, even when the model error approaches zero. When error is added to the synthetic seismogram, the Gaussian predictor gives very little information about the water saturation variable while the mixture Gaussian and generalized Gaussian predictor provides good estimates that captures the general trend for all the variables.

We conclude that the test study shows encouraging results for the mixture Gaussian and generalized Gaussian prior model setups. The posterior models provides computationally efficient inversion methodologies that are very suitable for 2D and 3D seismic data. The extensions of the models to a 2D or 3D setting is straight forward for all three models, although numerical methods may be required to obtain numerical values for the statistics.

We hope the work in the current thesis will inspire further work on the subject. Since the methodologies are constructed with the application to real seismic data in mind, a natural extension is to do a parameter estimation study. If well observations from the area of examination are available, the

unknown parameters in the prior and likelihood model should be estimated by for example a maximum likelihood approach. This is not a trivial problem when the posterior distribution is multimodal. In Rimstad and Omre (2012) an MCMC approximate maximum likelihood method for estimating the parameters in the generalized Gaussian model is presented, which could also be applied to the current generalized Gaussian setup.

In the mixture Gaussian prior case we find the expression for the variance in the approximate Gaussian prior by assuming that $\boldsymbol{\pi} = \pi \mathbf{i}_T$. This assumption enforces a very high correlation between the nodes. The exact variance of Expression 3.15 together with a hidden Markov chain model on $\boldsymbol{\pi}$ will decrease the confidence intervals in the mixture Gaussian prior setup. We would then have to use the Forward-Backward algorithm to assess the posterior model.

Another extension is to include controlled-source electromagnetic (CSEM) data in the model. CSEM is still a developing technology, but it has recently been introduced for commercial purposes. As the electrical conductivity is highly dependent on the pore fluid, we should be able to obtain a more accurate prediction of the water saturation by utilizing the CEMS data together with the seismic data.

Bibliography

K. Aki and P. G. Richards. *Quantitative Seismology: Theory and Methods*. Geology (University Science Books): Seismology. W. H. Freeman Co., 1980. ISBN 9780935702965.

P. Avseth, T. Mukerji, G. Mavko, and J. Dvorkin. Rock-physics diagnostics of depositional texture, diagenetic alterations, and reservoir heterogeneity in high-porosity siliciclastic sediments and rocks — a review of selected models and suggested work flows. *Geophysics*, 75(5):75A31–75A47, 2010.

R. Bachrach. Joint estimation of porosity and saturation using stochastic rock-physics modeling. *Geophysics*, 71(5):O53–O63, 2006.

A. Buland and H. Omre. Bayesian linearized avo inversion. *Geophysics*, 68 (1):185–198, 2003.

J. Dvorkin, G. Mavko, and B. Gurevich. Fluid substitution in shaley sediment using effective porosity. *Geophysics*, 72(3):O1–O8, 2007.

D. Grana. *Bayesian inversion methods for seismic reservoir characterization and time-lapse studies*. PhD thesis, Stanford University, August 2013.

D. Grana, T. Mukerji, L. Dovera, and E. Della Rossa. Sequential Simulations of Mixed Discrete-Continuous Properties: Sequential Gaussian Mixture Simulation. In *Geostatistics Oslo 2012*, pages 239–250. Springer Netherlands, 2012.

M. Landrø. Discrimination between pressure and fluid saturation changes from time-lapse seismic data. *Geophysics*, 66(3):836–844, 2001.

M. Landrø. Uncertainties in quantitative time-lapse seismic analysis. *Geophysical Prospecting*, 50(5):527–538, 2002.

G. Mavko, T. Mukerji, and J. Dvorkin. *The Rock Physics Handbook: Tools for Seismic Analysis in Porous Media*. Cambridge University Press, 2003. ISBN 9780521543446.

BIBLIOGRAPHY

K. Rimstad and H. Omre. Generalized Gaussian Random Fields using hidden sections, 2012. Norwegian University of Science and Technology, Department of Mathematical Sciences.

H. Veire, H. Borgos, and M. Landrø. Stochastic inversion of pressure and saturation changes from time-lapse avo data. *Geophysics*, 71(5):C81–C92, 2006.

H. H. Veire, H. G. Borgos, and M. Landrø. Stochastic inversion of pressure and saturation changes from time-lapse multi component data. *Geophysical Prospecting*, 55(6):805–818, 2007.

Appendix A

Cross study

In this appendix we display the inversion results for a cross study of varying signal-noise ratio in the inversion and synthetic model, see Table A.1 for the model setups. Further analysis is left to the reader.

		Inversion Model			
	SNR	2	5	20	10^4
Synthetic Model	2	x	x	x	
	5	x	x	x	
	20	x	x	x	
	10^4				x

Table A.1: x = Inversion result for model setup is displayed in Appendix A

GAUSSIAN PRIOR CASE

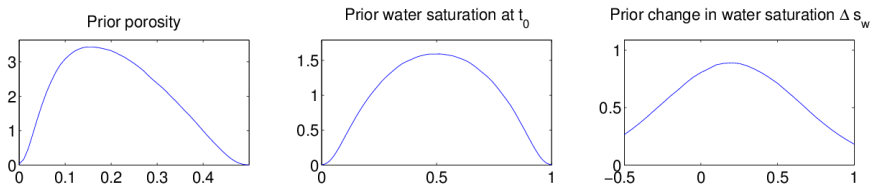

Synthetic earth profile made with SNR=10^4
Inversion model with SNR=10^4

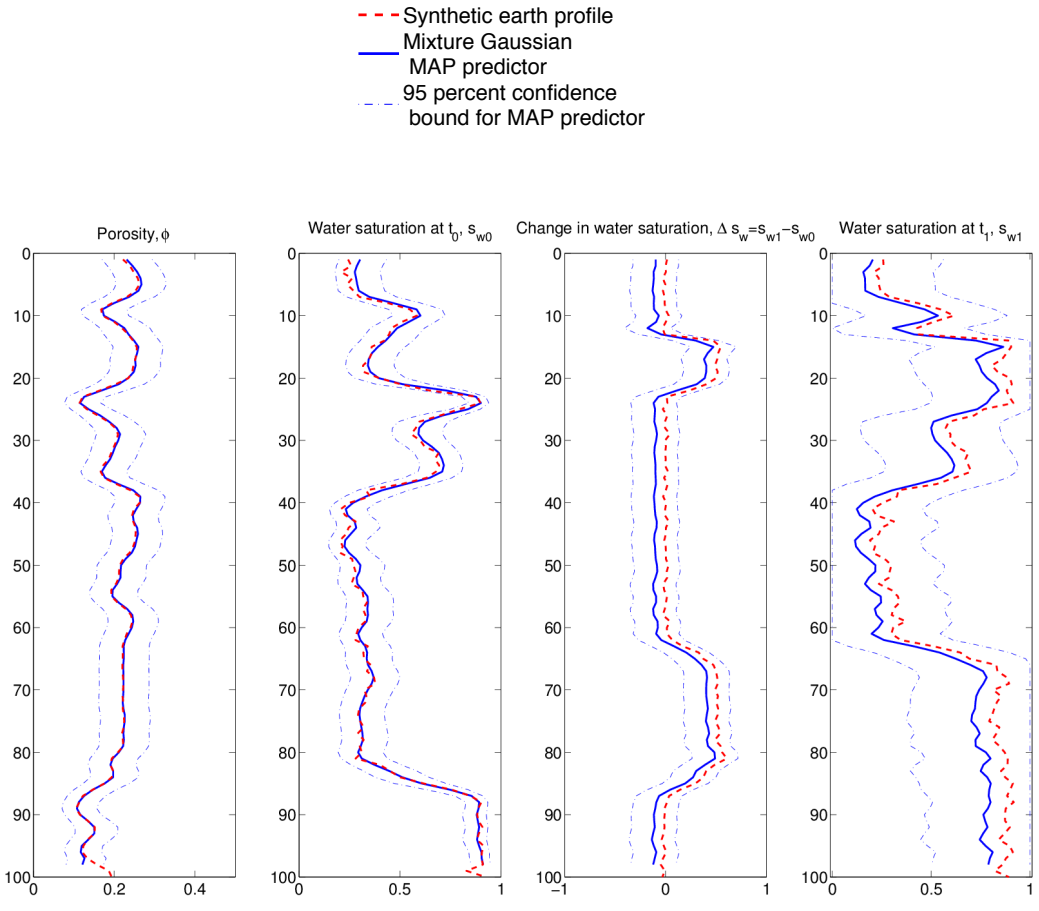

Figure A.1: Synthetic model with SNR=10^4 and SNR=10^4 in the inversion model

GAUSSIAN PRIOR CASE

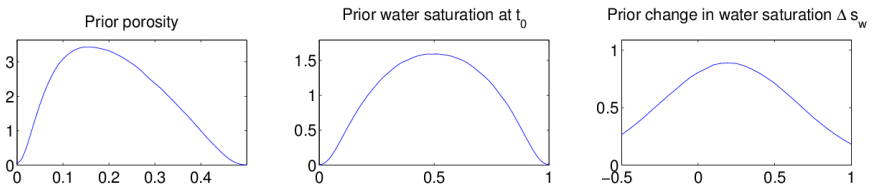

Synthetic earth profile made with SNR=20
Inversion model with SNR=20

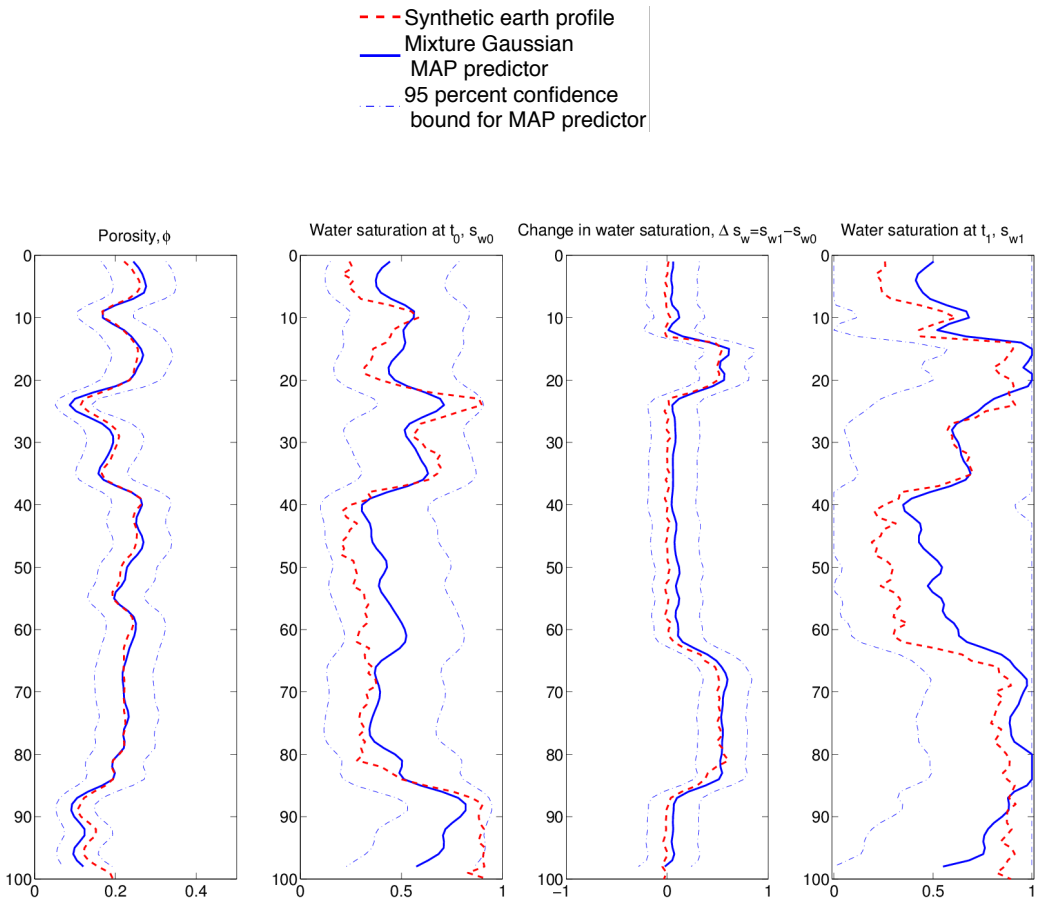

Figure A.2: Synthetic model with SNR=20 and SNR=20 in the inversion model

GAUSSIAN PRIOR CASE

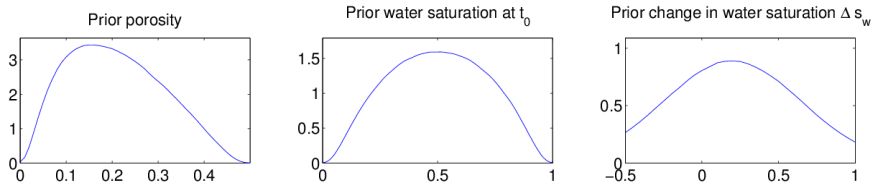

Synthetic earth profile made with SNR=5
Inversion model with SNR=5

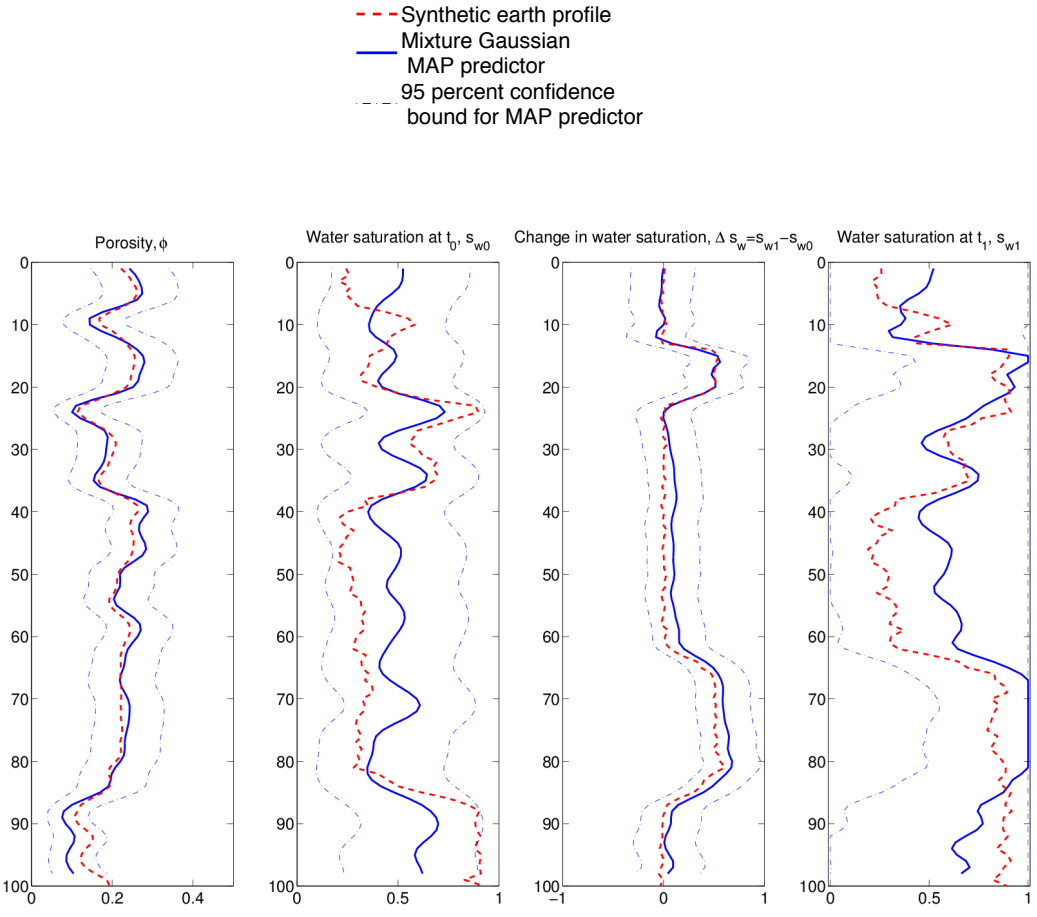

Figure A.3: Synthetic model with SNR=5 and SNR=5 in the inversion model

GAUSSIAN PRIOR CASE

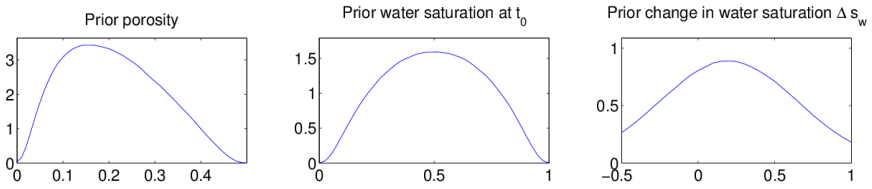

Synthetic earth profile made with SNR=2
Inversion model with SNR=2

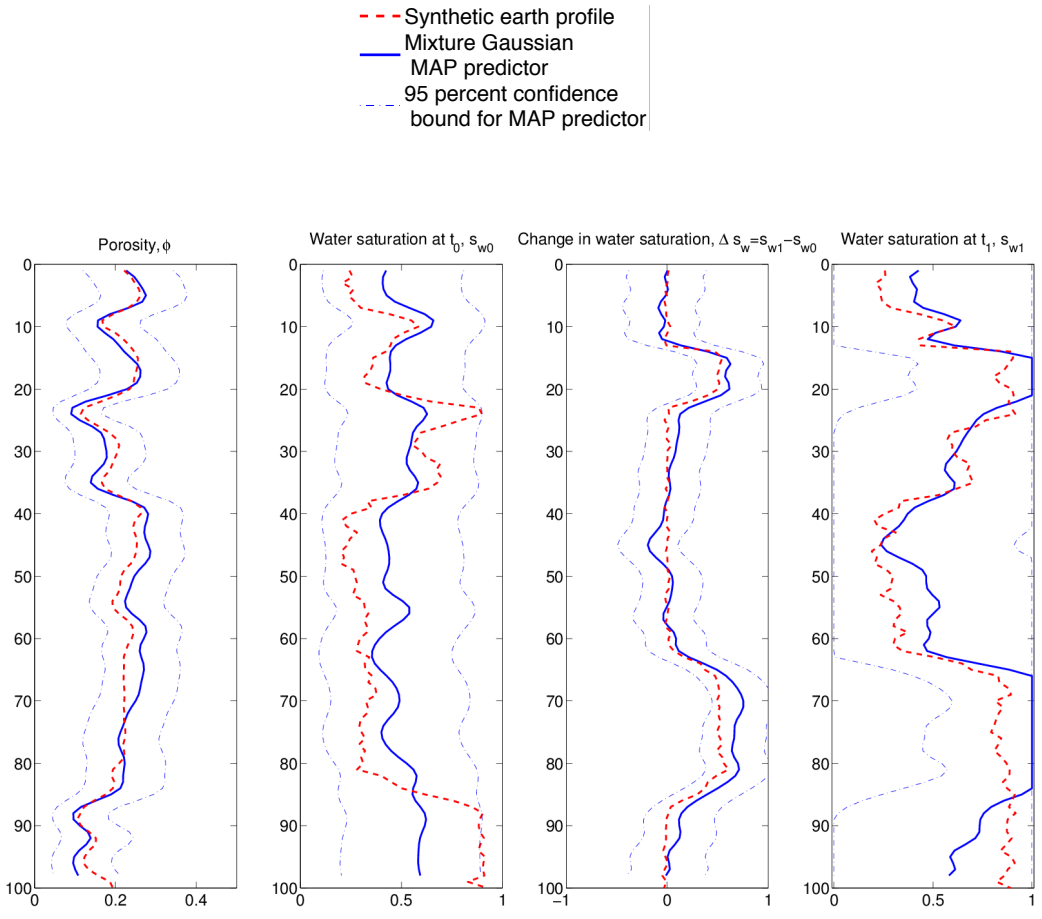

Figure A.4: Synthetic model with SNR=2 and SNR=2 in the inversion model

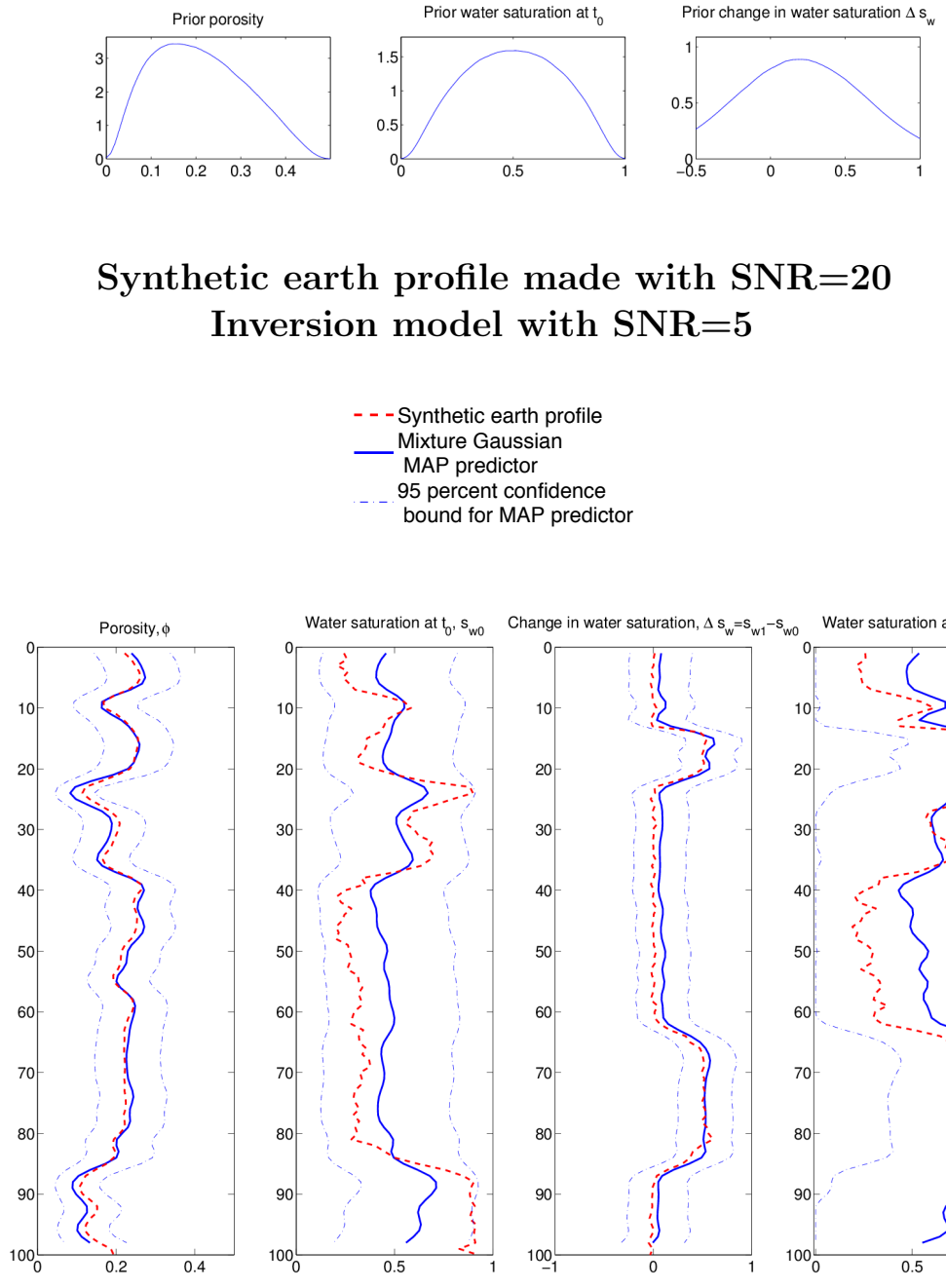

Figure A.5: Synthetic model with SNR=20 and SNR=5 in the inversion model

GAUSSIAN PRIOR CASE

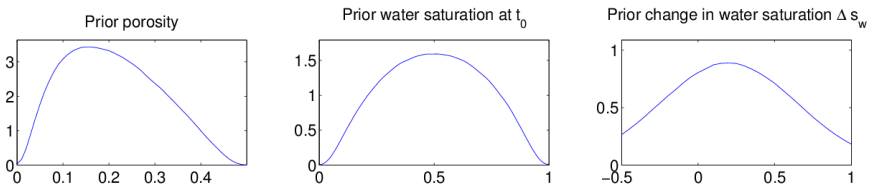

Synthetic earth profile made with SNR=20
Inversion model with SNR=2

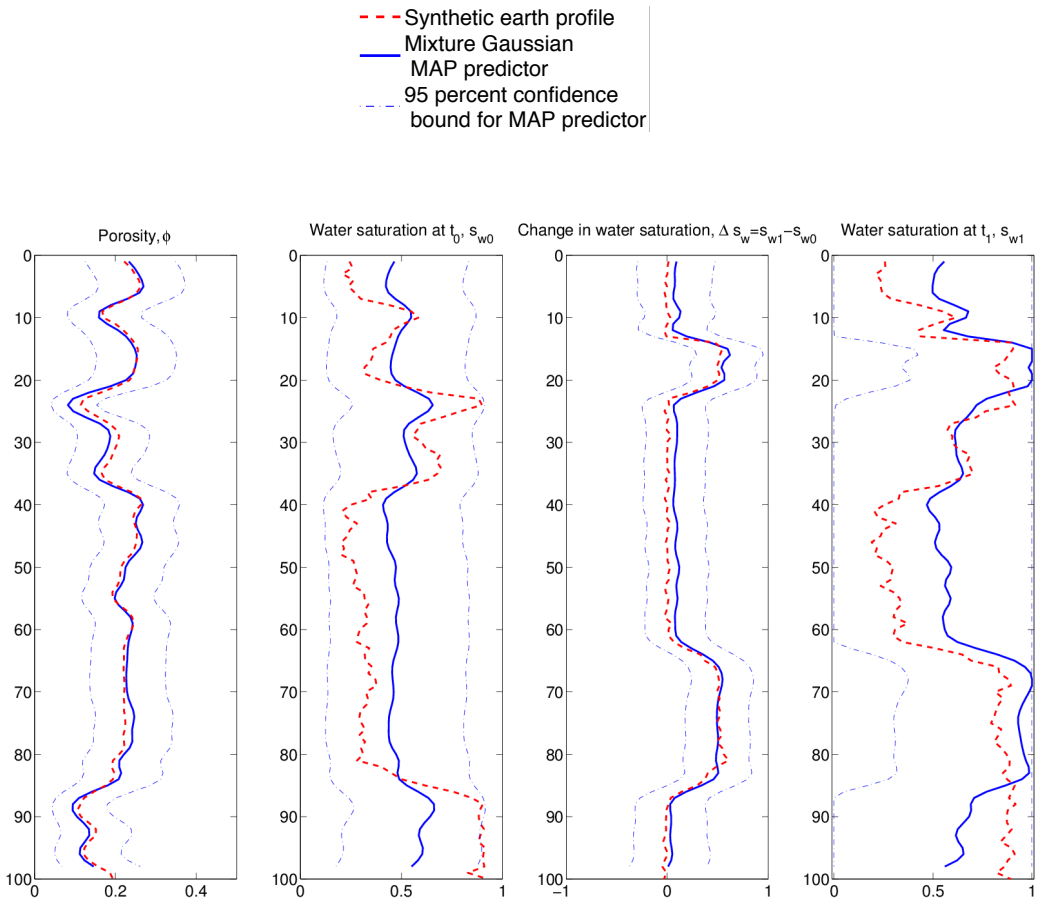

Figure A.6: Synthetic model with SNR=20 and SNR=2 in the inversion model

GAUSSIAN PRIOR CASE

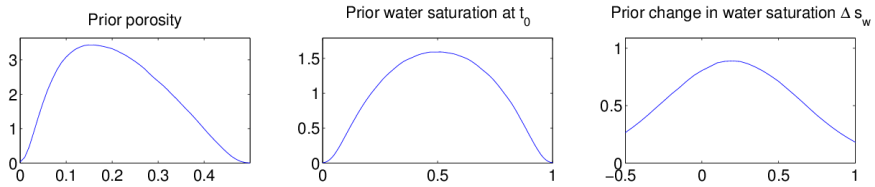

Synthetic earth profile made with SNR=5
Inversion model with SNR=20

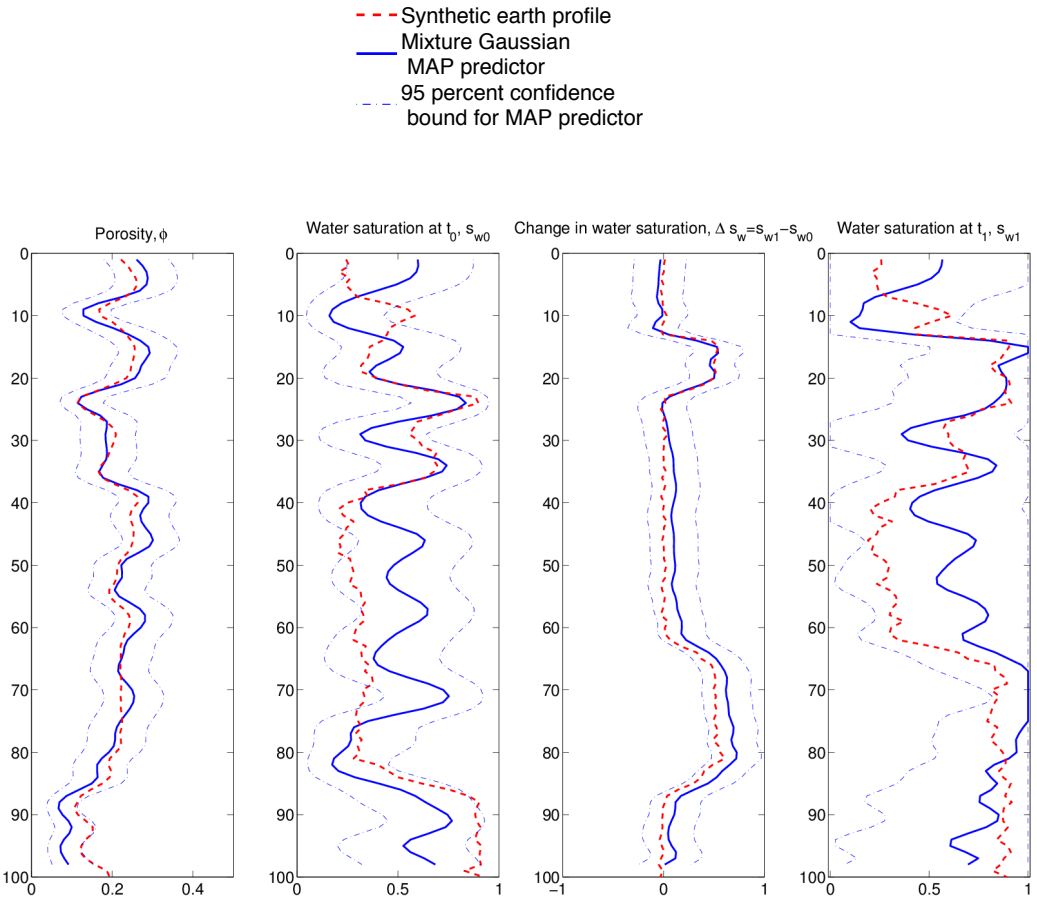

Figure A.7: Synthetic model with SNR=5 and SNR=20 in the inversion model

GAUSSIAN PRIOR CASE

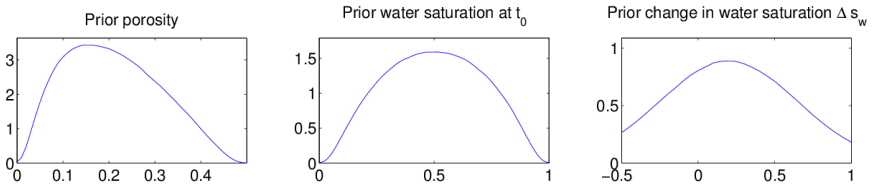

Synthetic earth profile made with SNR=5
Inversion model with SNR=2

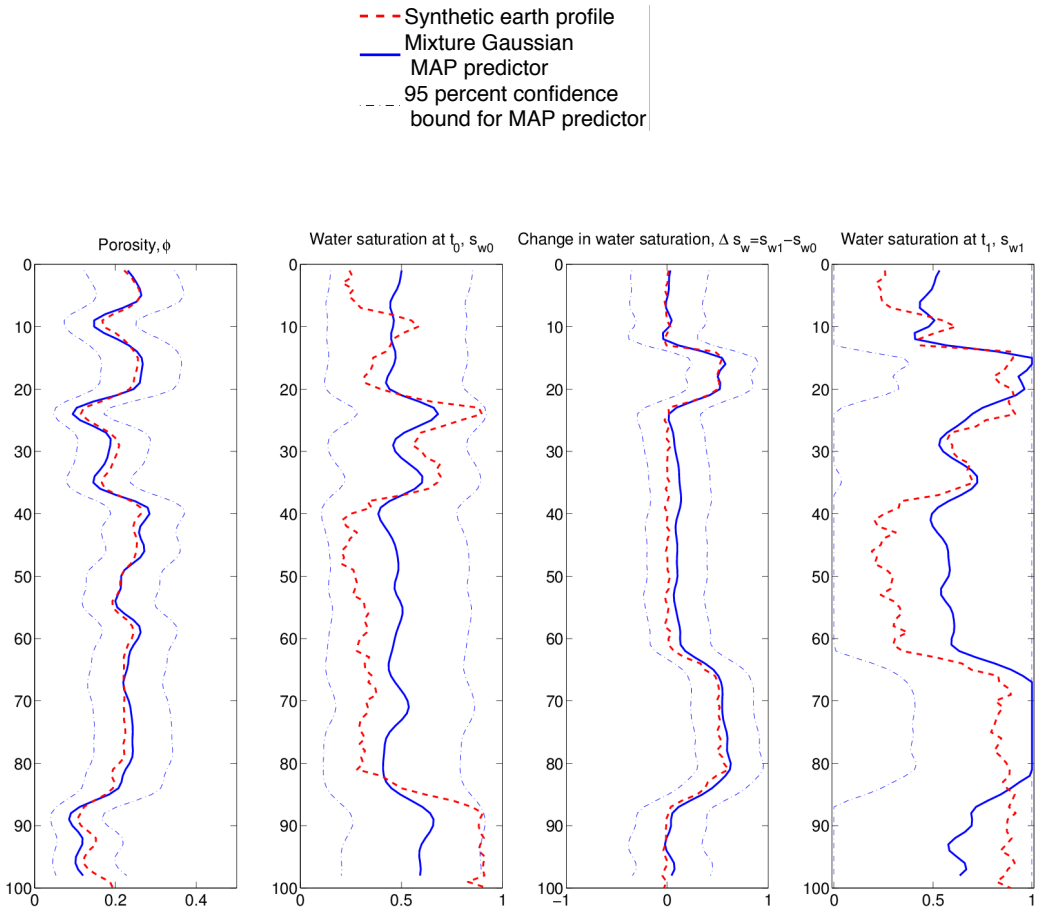

Figure A.8: Synthetic model with SNR=5 and SNR=2 in the inversion model

GAUSSIAN PRIOR CASE

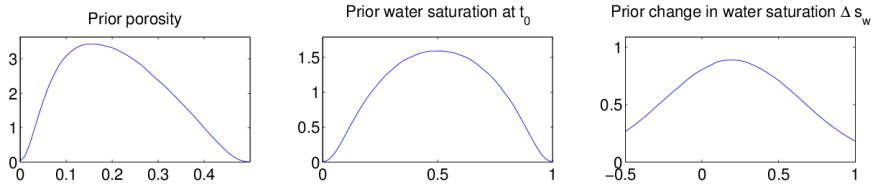

Synthetic earth profile made with SNR=2
Inversion model with SNR=20

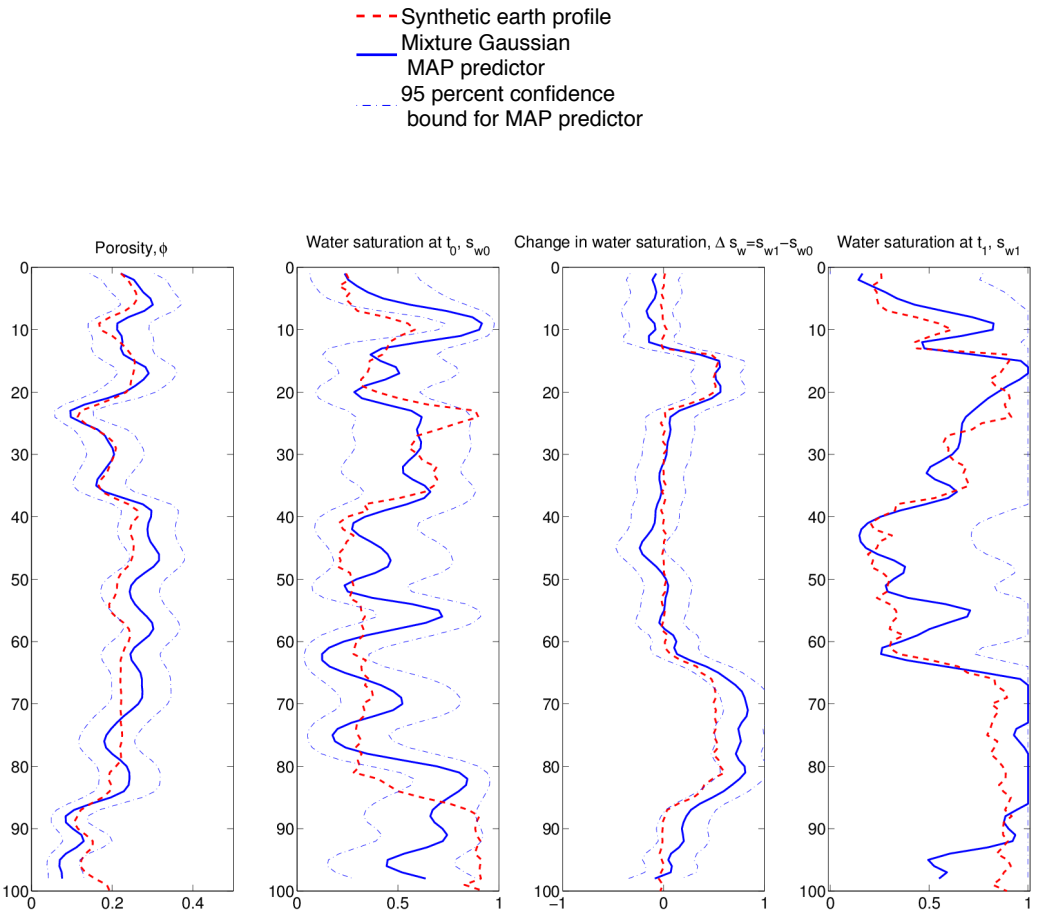

Figure A.9: Synthetic model with SNR=2 and SNR=20 in the inversion model

GAUSSIAN PRIOR CASE

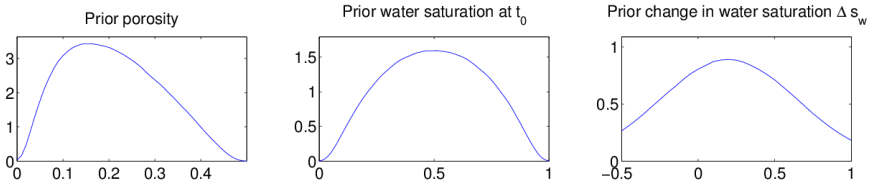

Synthetic earth profile made with SNR=2
Inversion model with SNR=5

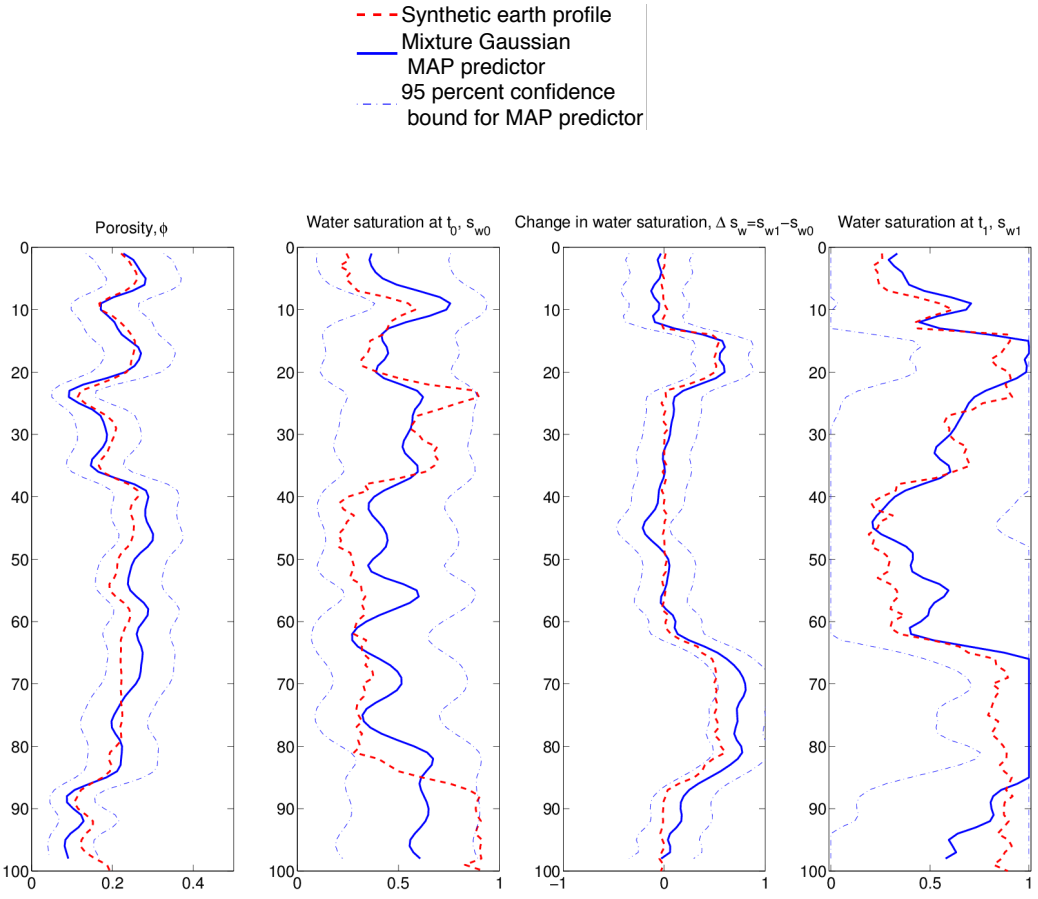

Figure A.10: Synthetic model with SNR=2 and SNR=5 in the inversion model

MIXTURE GAUSSIAN PRIOR CASE

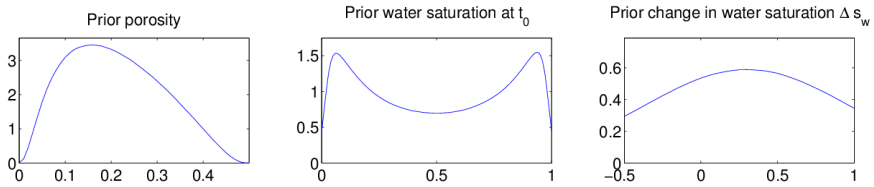

Synthetic earth profile made with SNR=10^4
Inversion model with SNR=10^4

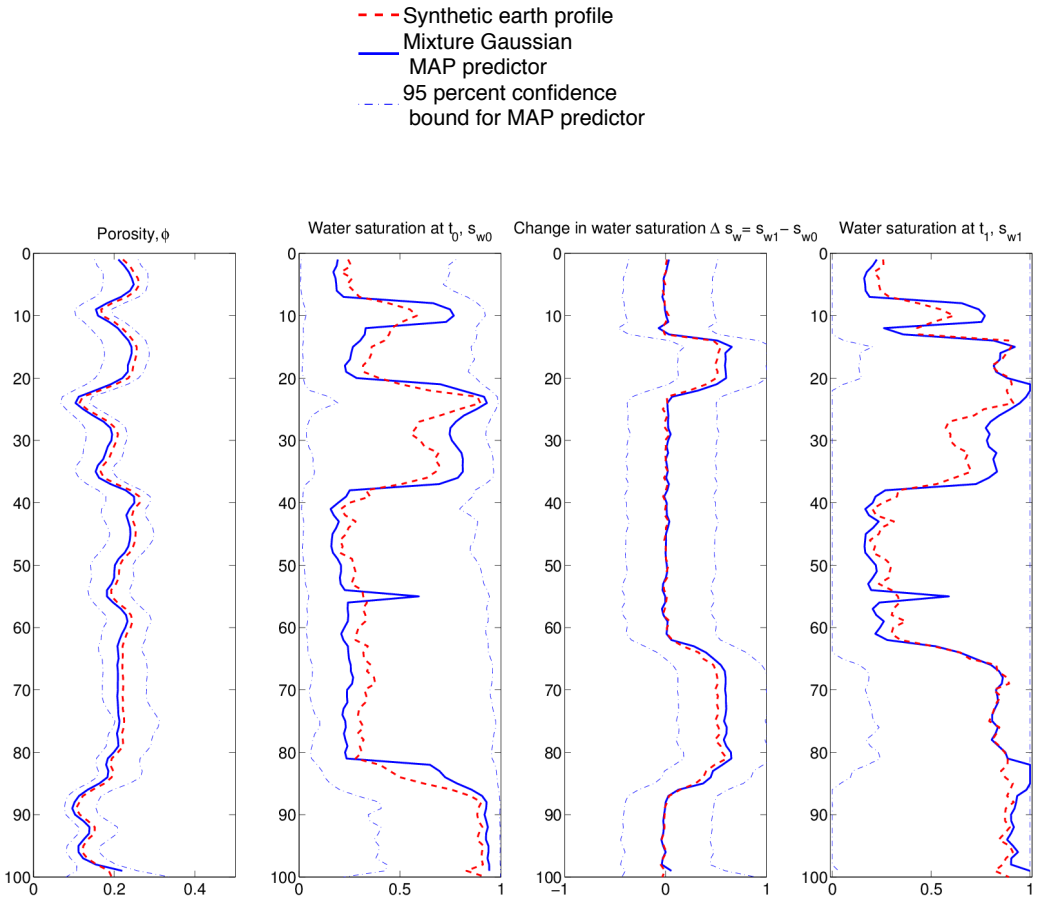

Figure A.11: Synthetic model with SNR=10^4 and SNR=10^4 in the inversion model

MIXTURE GAUSSIAN PRIOR CASE

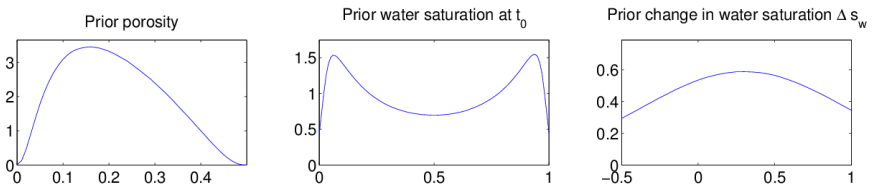

Synthetic earth profile made with SNR=20
Inversion model with SNR=20

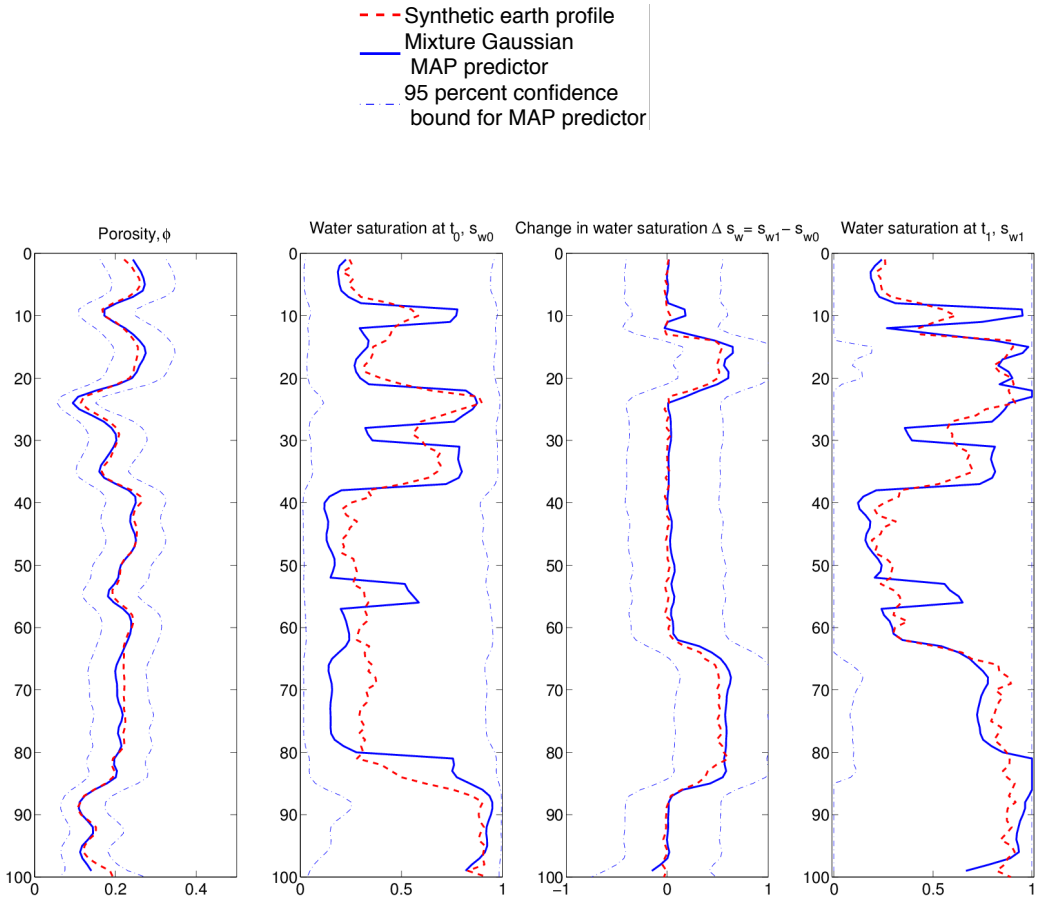

Figure A.12: Synthetic model with SNR=20 and SNR=20 in the inversion model

MIXTURE GAUSSIAN PRIOR CASE

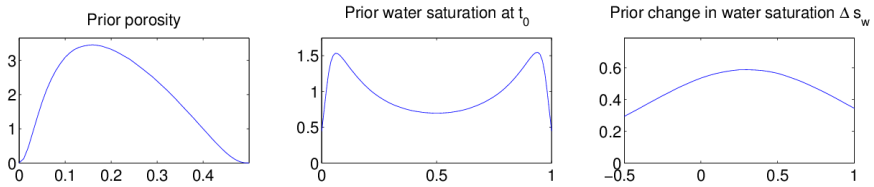

Synthetic earth profile made with SNR=5
Inversion model with SNR=5

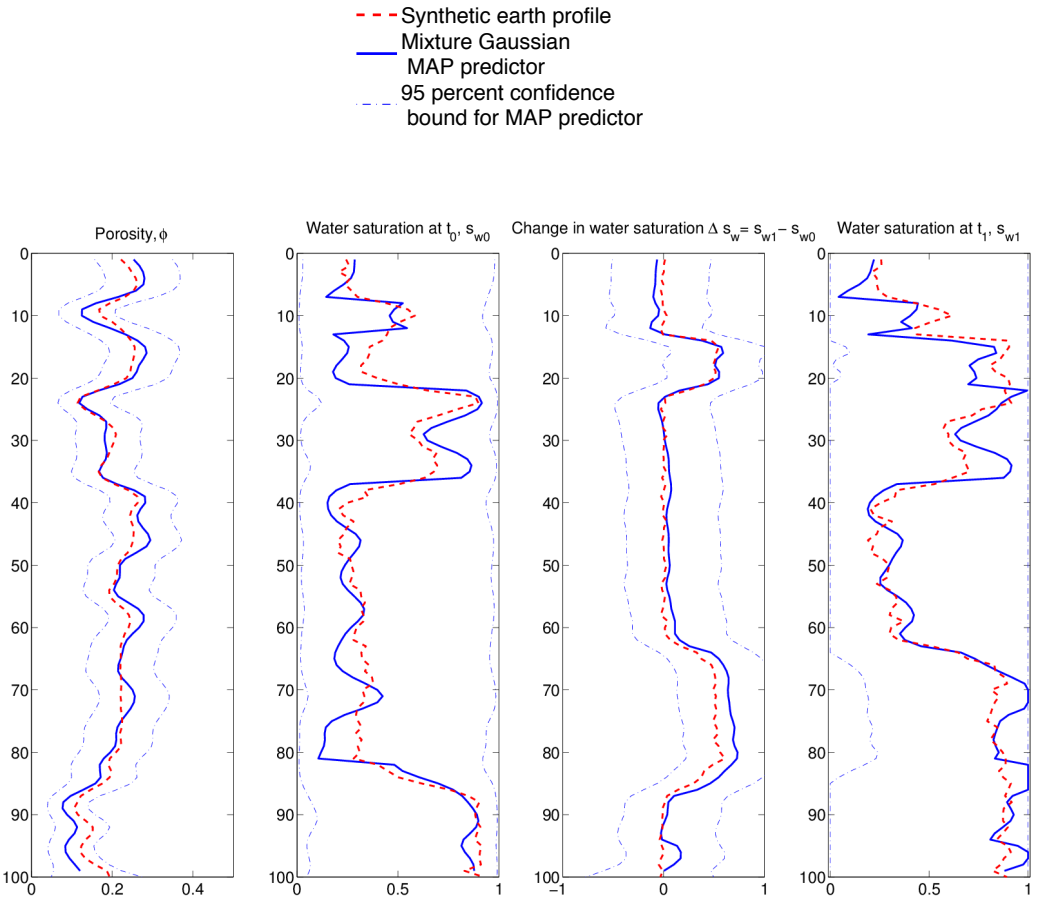

Figure A.13: Synthetic model with SNR=5 and SNR=5 in the inversion model

MIXTURE GAUSSIAN PRIOR CASE

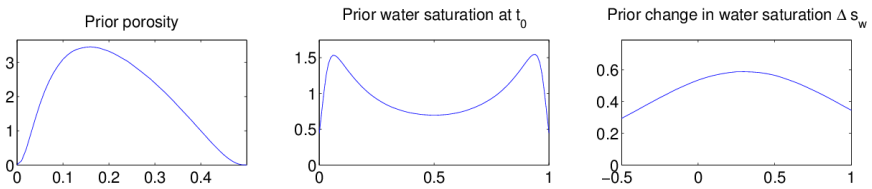

Synthetic earth profile made with SNR=2
Inversion model with SNR=2

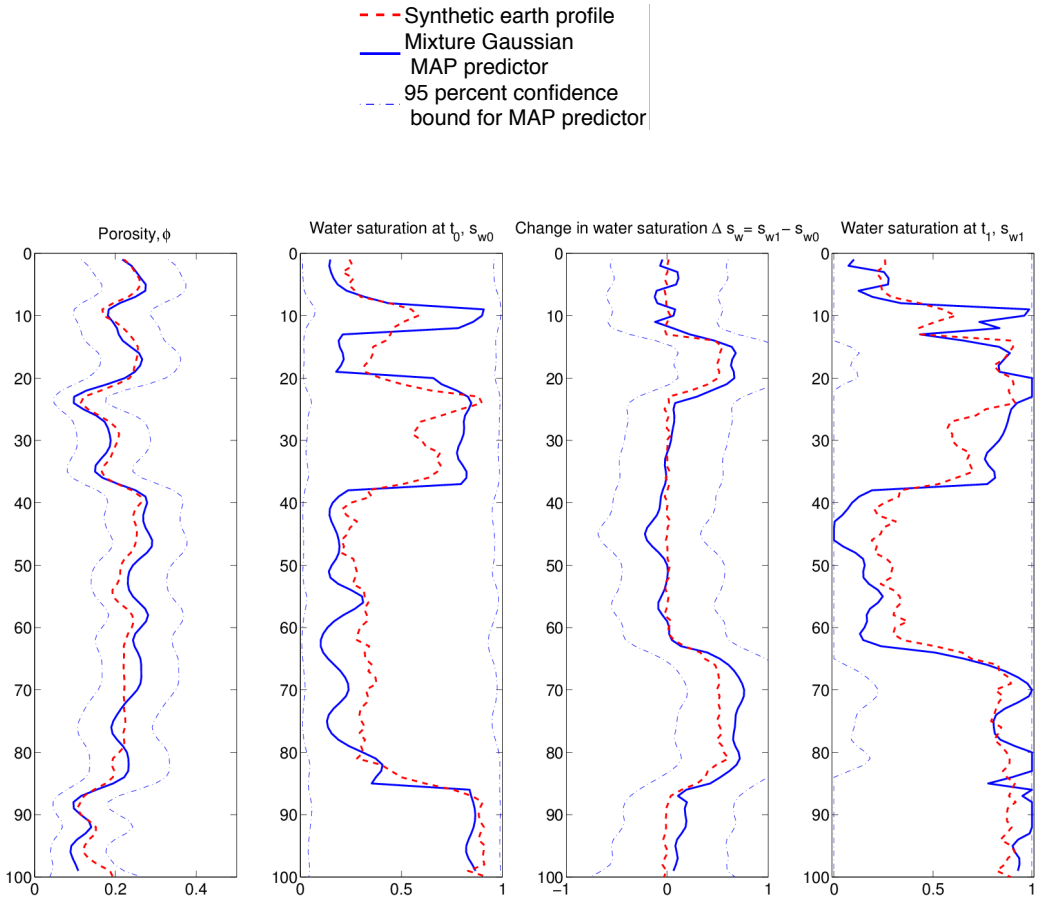

Figure A.14: Synthetic model with SNR=2 and SNR=2 in the inversion model

MIXTURE GAUSSIAN PRIOR CASE

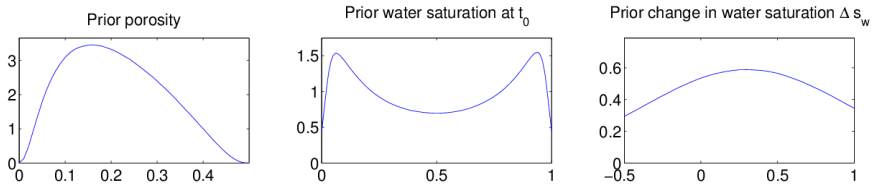

Synthetic earth profile made with SNR=20
Inversion model with SNR=5

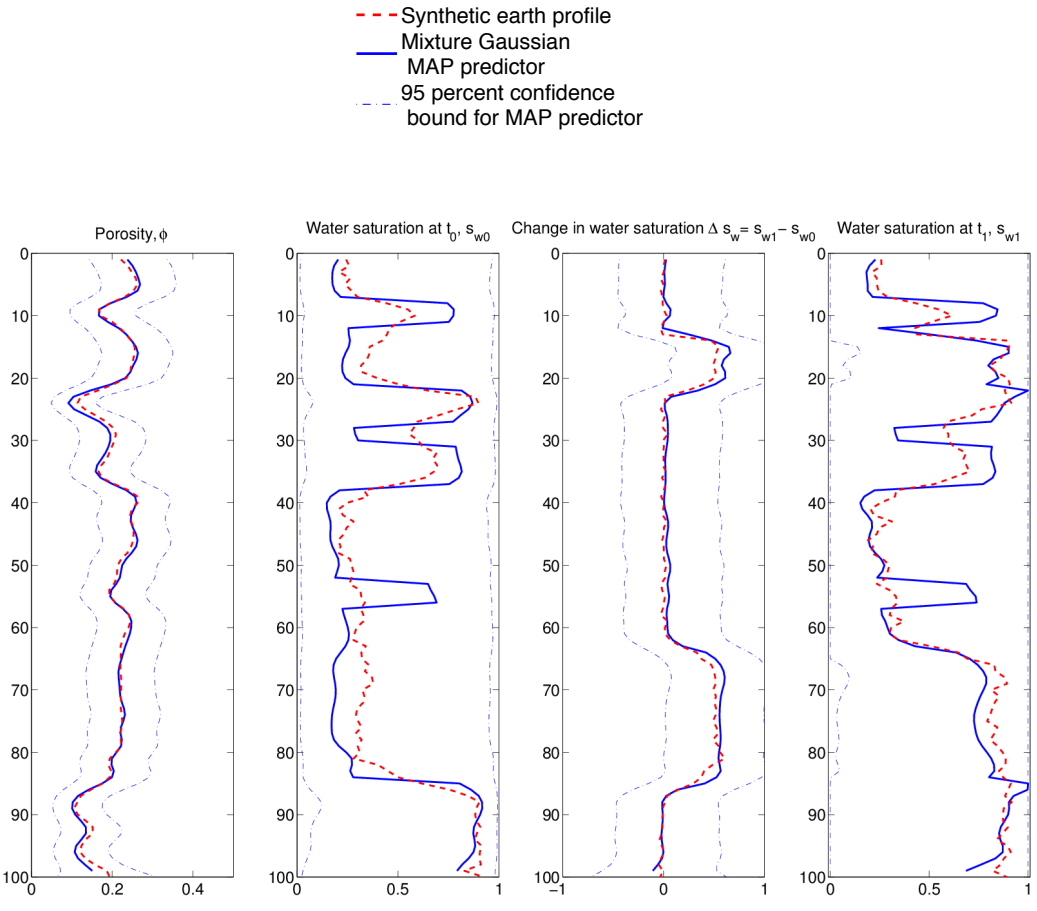

Figure A.15: Synthetic model with SNR=20 and SNR=5 in the inversion model

MIXTURE GAUSSIAN PRIOR CASE

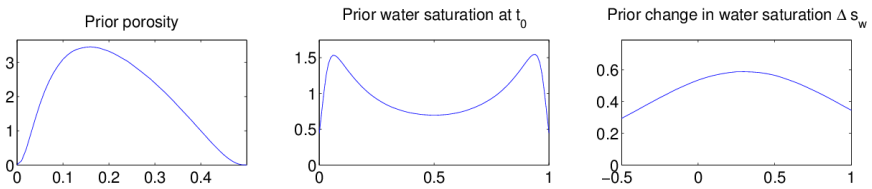

Synthetic earth profile made with SNR=20
Inversion model with SNR=2

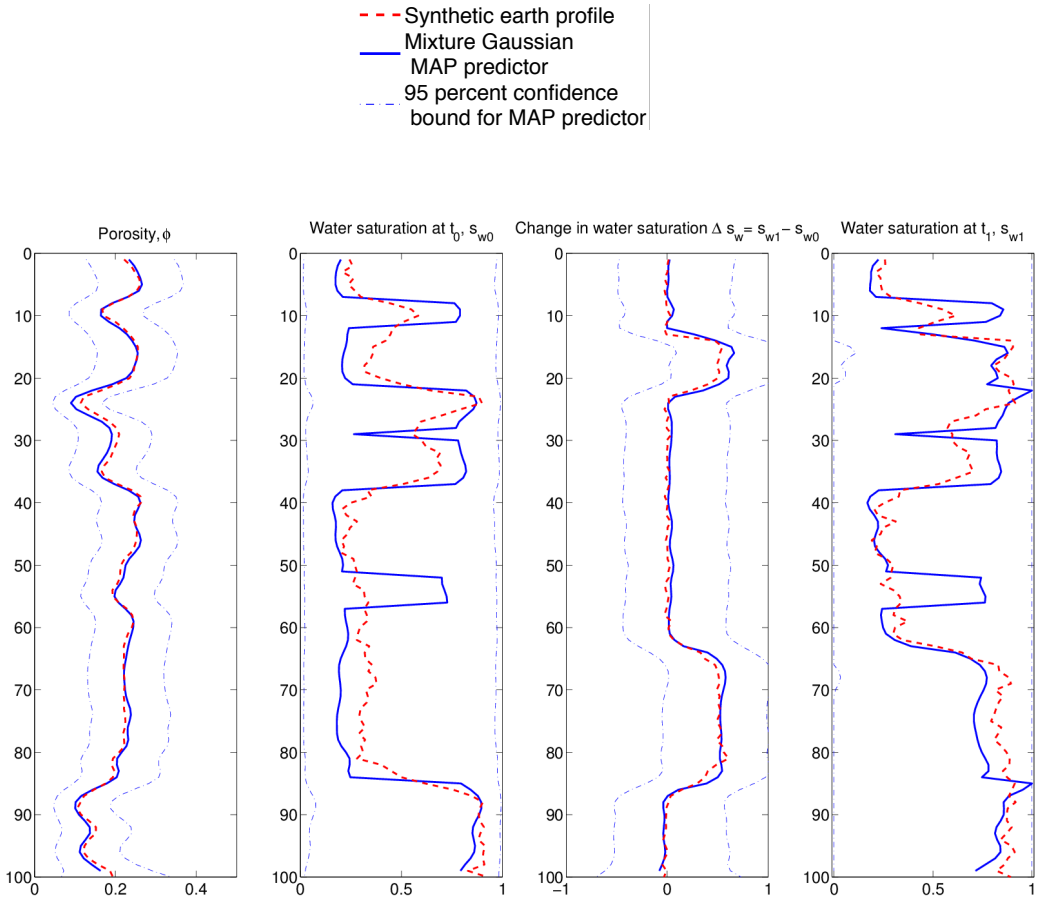

Figure A.16: Synthetic model with SNR=20 and SNR=2 in the inversion model

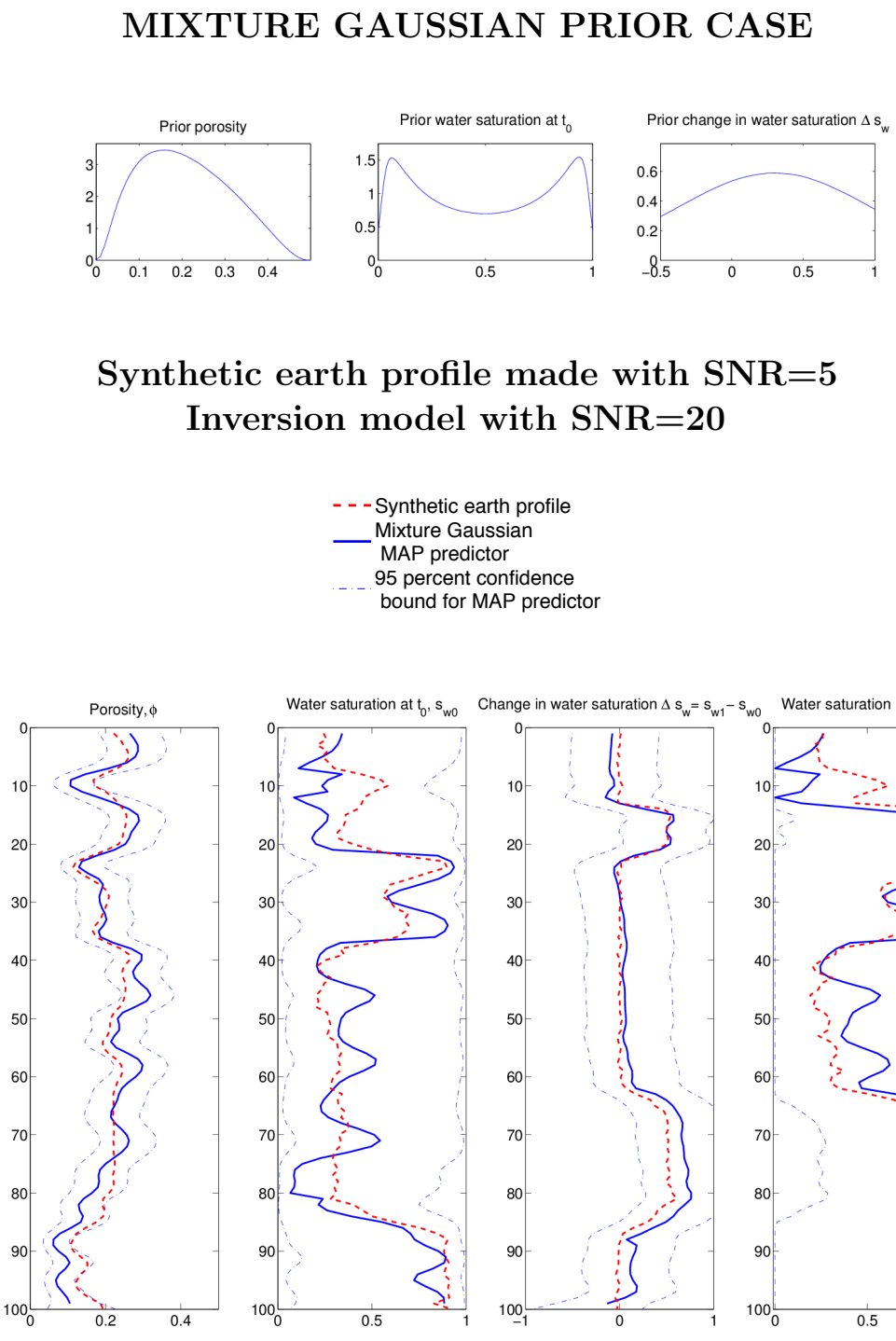

Figure A.17: Synthetic model with SNR=5 and SNR=20 in the inversion model

MIXTURE GAUSSIAN PRIOR CASE

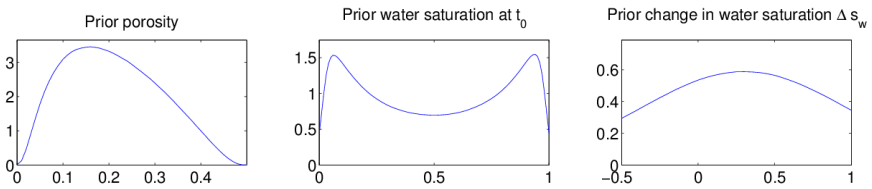

Synthetic earth profile made with SNR=5
Inversion model with SNR=2

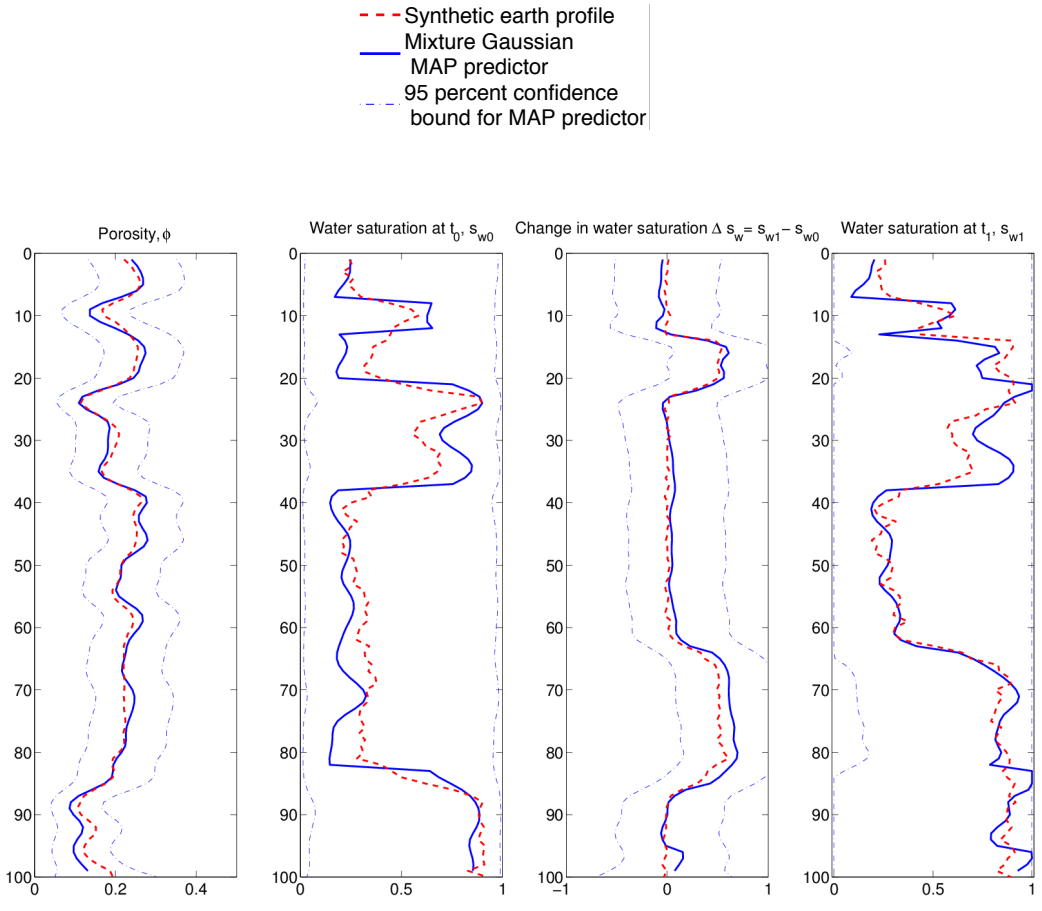

Figure A.18: Synthetic model with SNR=5 and SNR=2 in the inversion model

MIXTURE GAUSSIAN PRIOR CASE

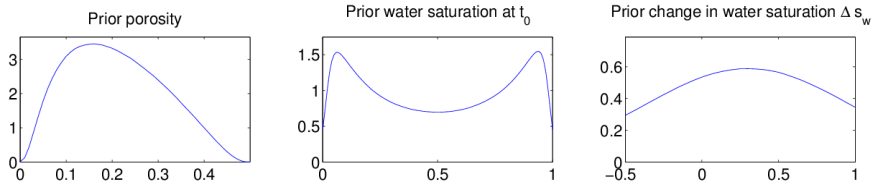

Synthetic earth profile made with SNR=2
Inversion model with SNR=20

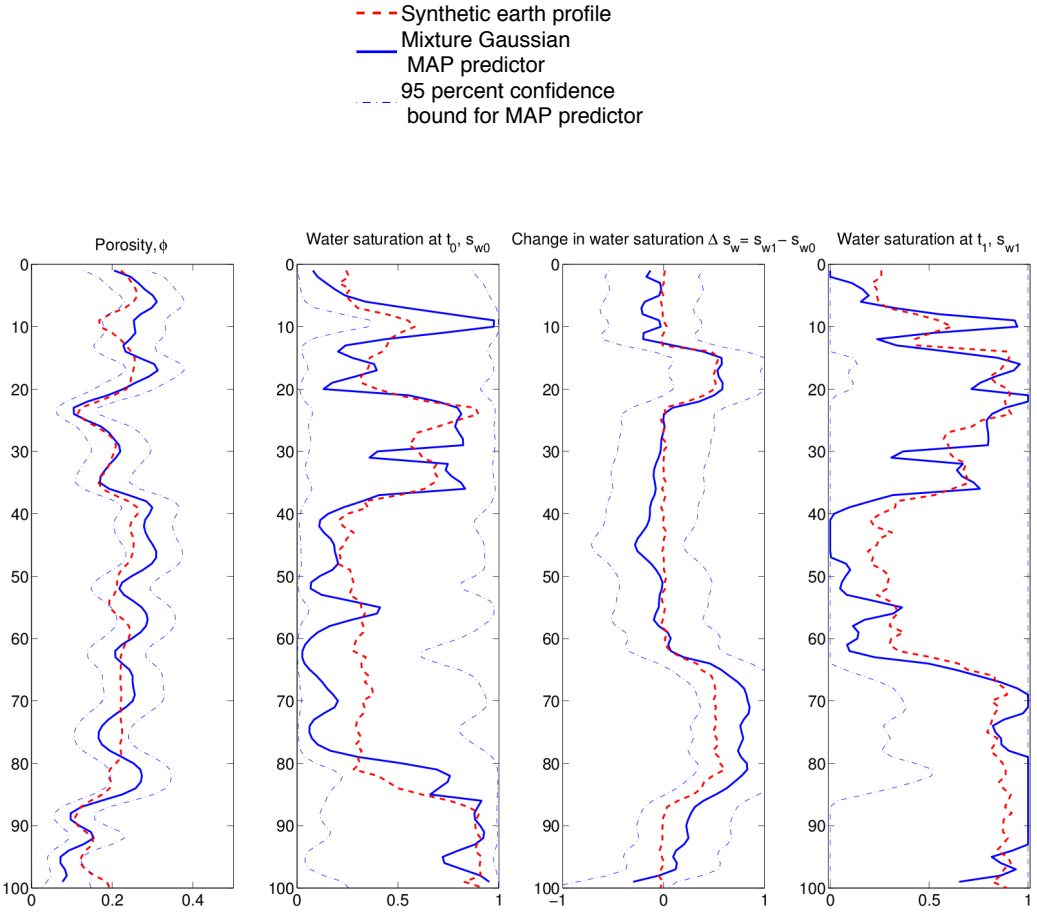

Figure A.19: Synthetic model with SNR=2 and SNR=20 in the inversion model

MIXTURE GAUSSIAN PRIOR CASE

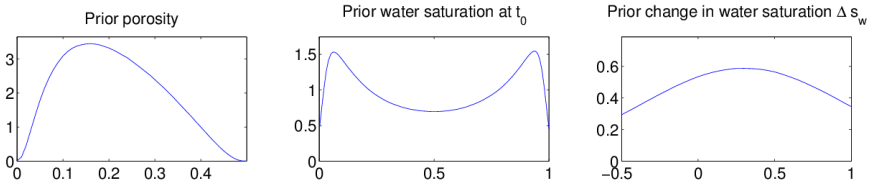

Synthetic earth profile made with SNR=2
Inversion model with SNR=5

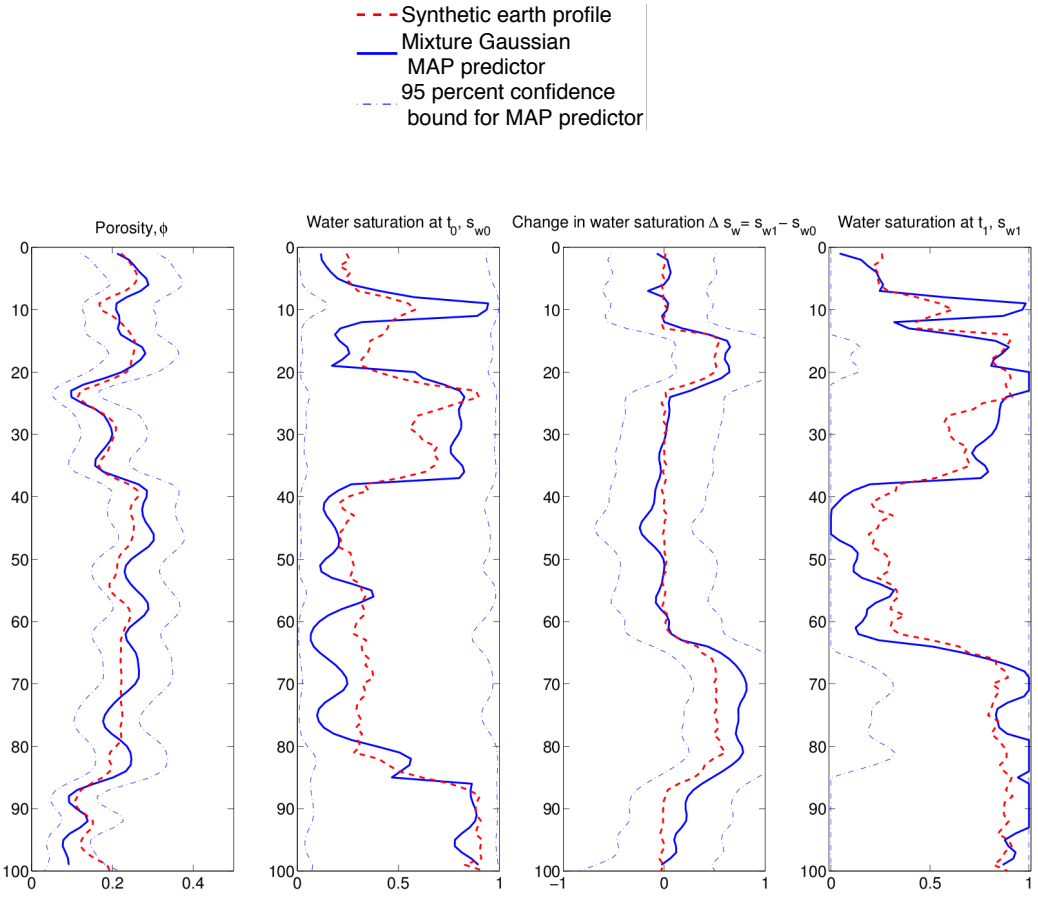

Figure A.20: Synthetic model with SNR=2 and SNR=5 in the inversion model

GENERALIZED GAUSSIAN PRIOR CASE

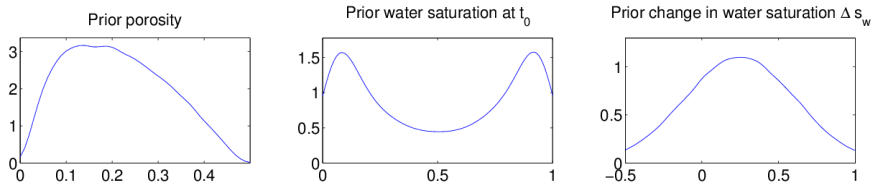

Synthetic earth profile made with SNR=10^4
Inversion model with SNR=10^4

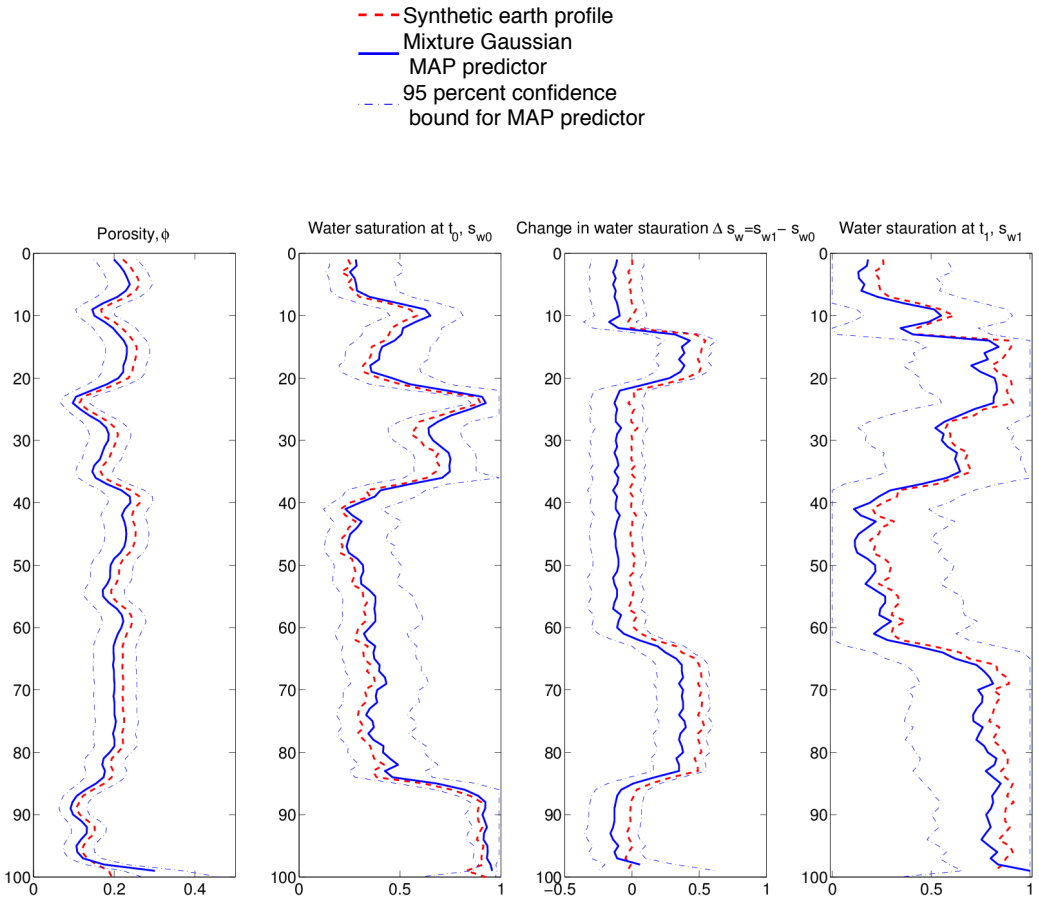

Figure A.21: Synthetic model with SNR=10^4 and SNR=10^4 in the inversion model

GENERALIZED GAUSSIAN PRIOR CASE

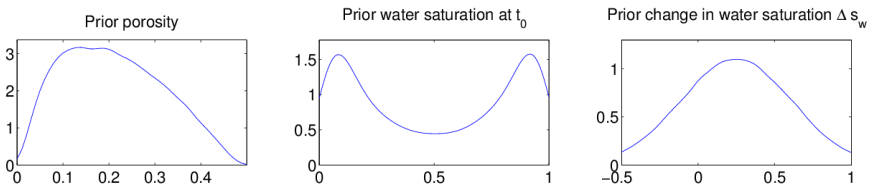

Synthetic earth profile made with SNR=20
Inversion model with SNR=20

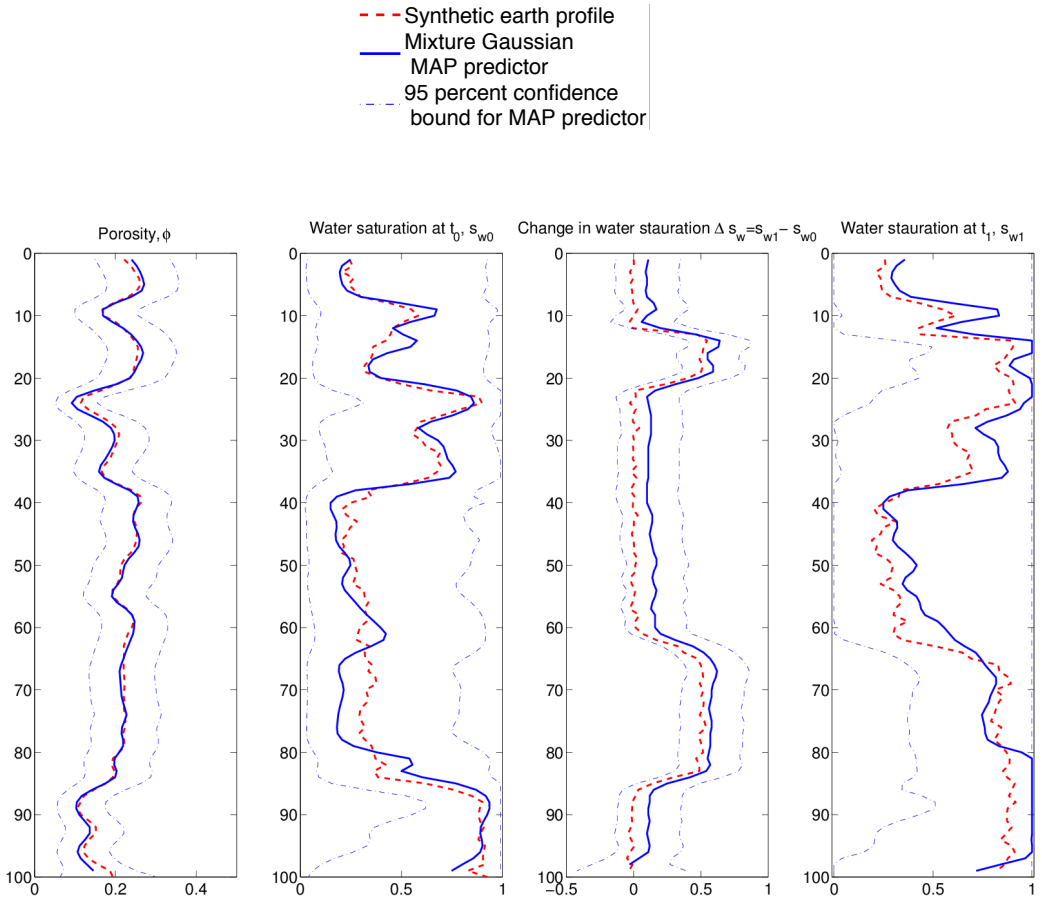

Figure A.22: Synthetic model with SNR=20 and SNR=20 in the inversion model

GENERALIZED GAUSSIAN PRIOR CASE

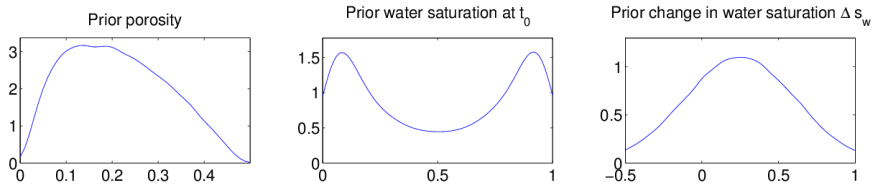

Synthetic earth profile made with SNR=5
Inversion model with SNR=5

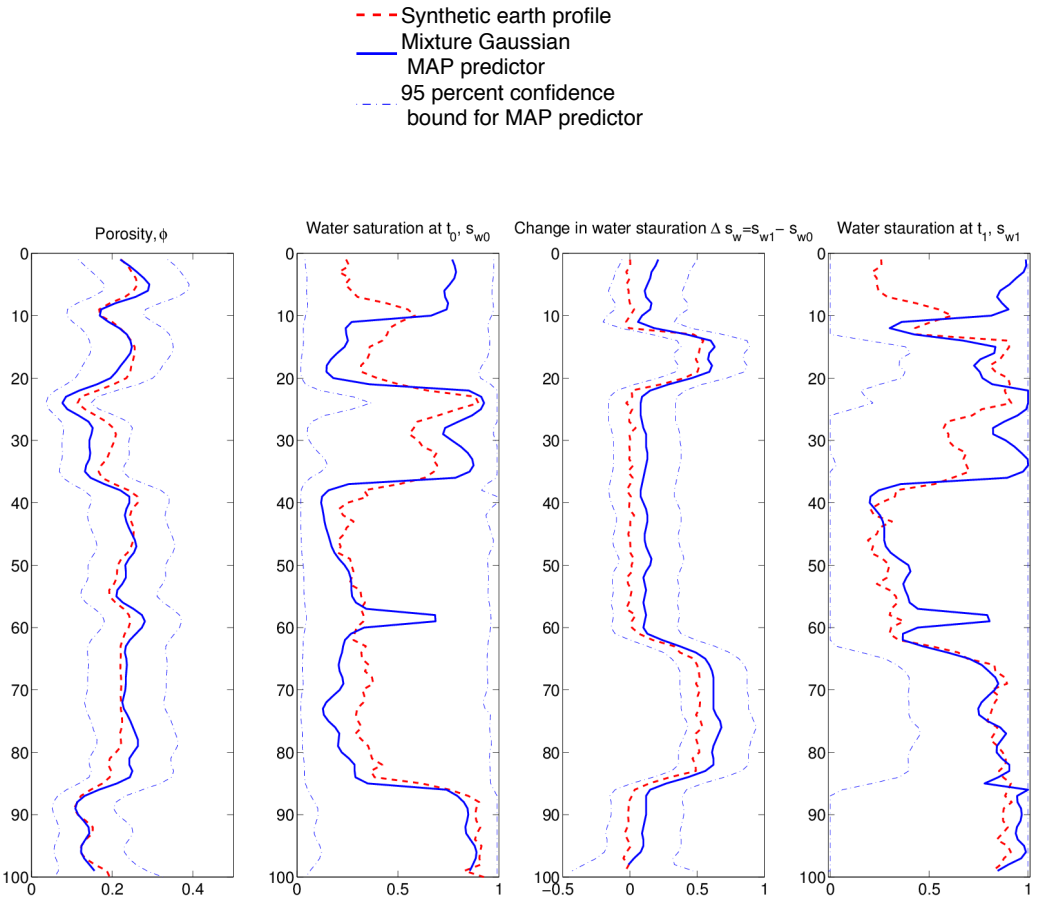

Figure A.23: Synthetic model with SNR=5 and SNR=5 in the inversion model

GENERALIZED GAUSSIAN PRIOR CASE

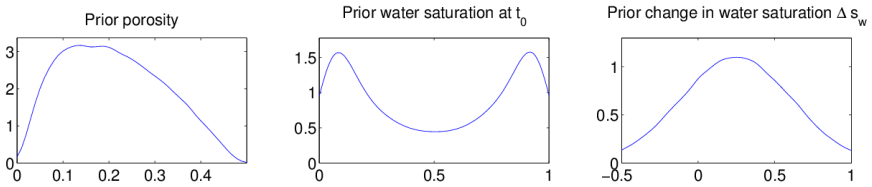

Synthetic earth profile made with SNR=2
Inversion model with SNR=2

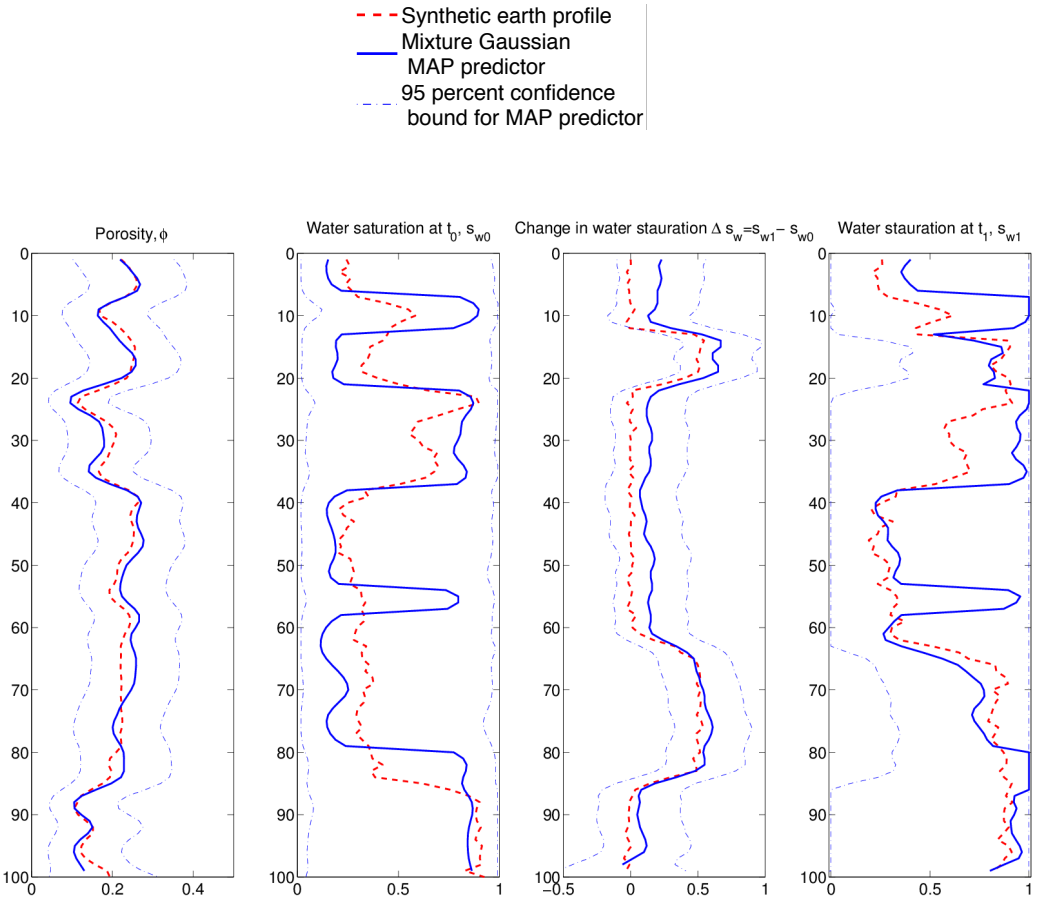

Figure A.24: Synthetic model with SNR=2 and SNR=2 in the inversion model

GENERALIZED GAUSSIAN PRIOR CASE

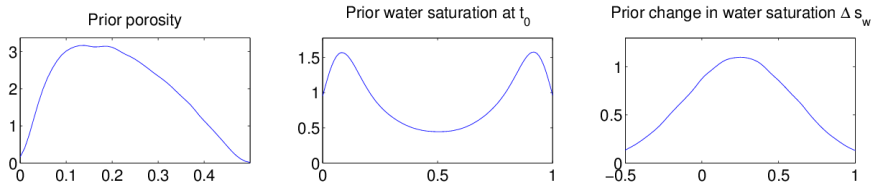

Synthetic earth profile made with SNR=20
Inversion model with SNR=5

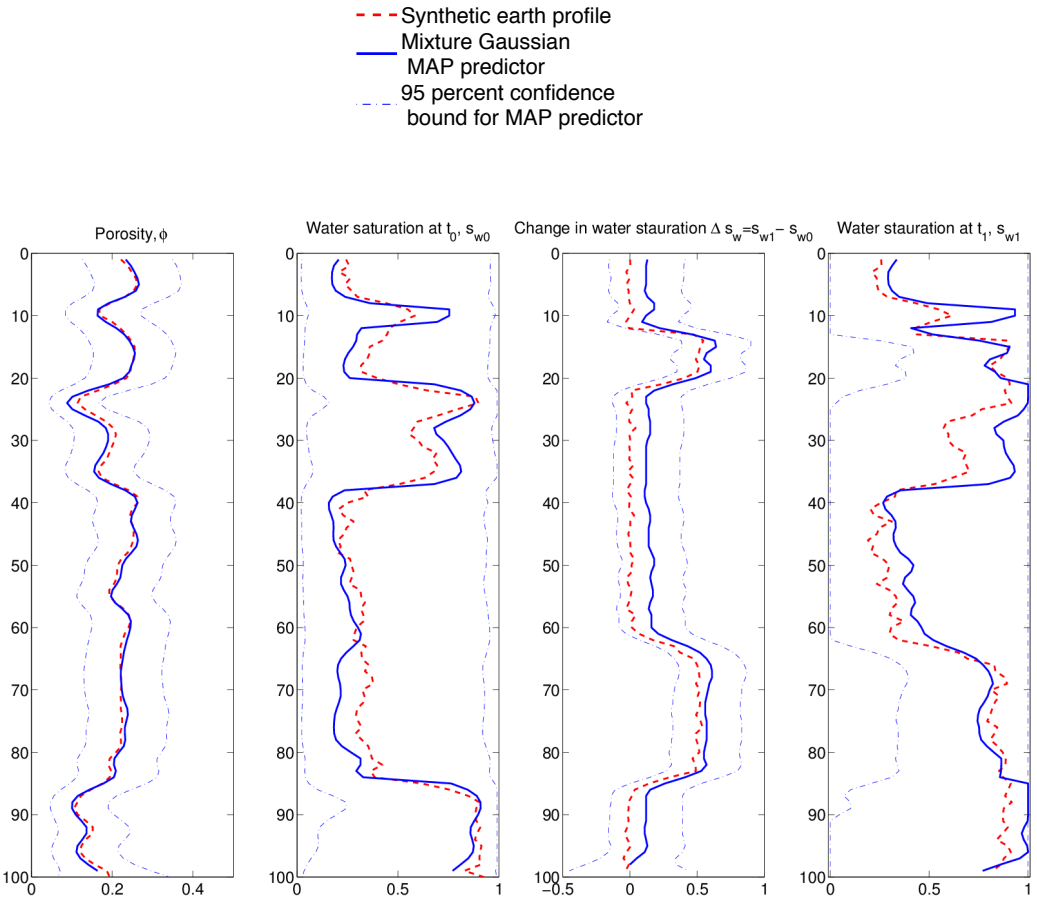

Figure A.25: Synthetic model with SNR=20 and SNR=5 in the inversion model

GENERALIZED GAUSSIAN PRIOR CASE

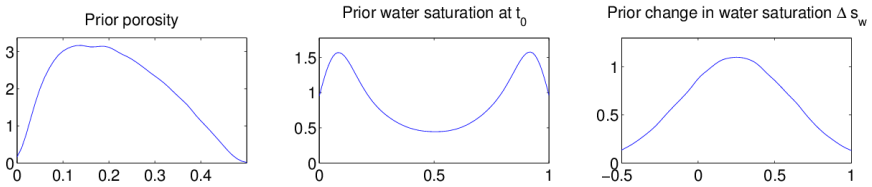

Synthetic earth profile made with SNR=20
Inversion model with SNR=2

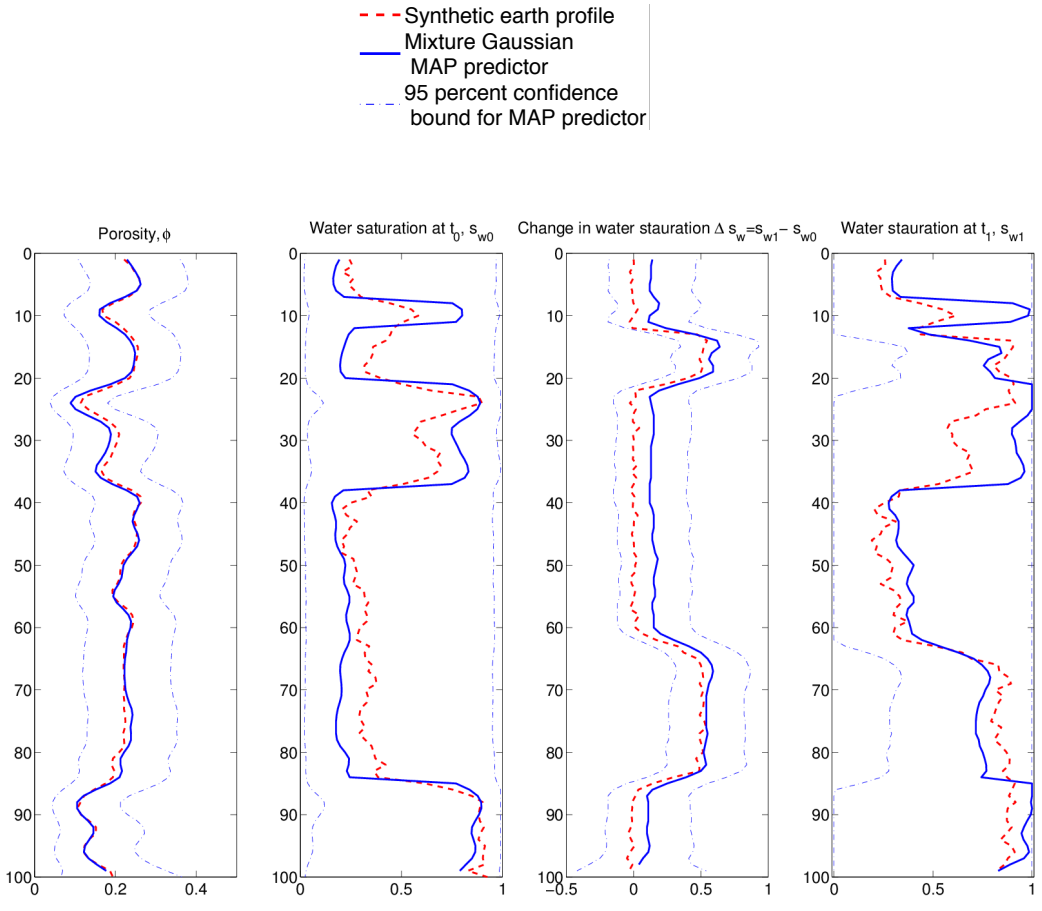

Figure A.26: Synthetic model with SNR=20 and SNR=2 in the inversion model

GENERALIZED GAUSSIAN PRIOR CASE

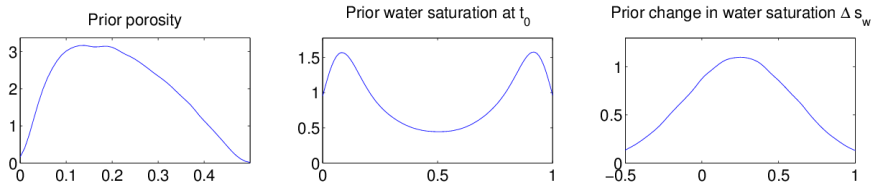

Synthetic earth profile made with SNR=5
Inversion model with SNR=20

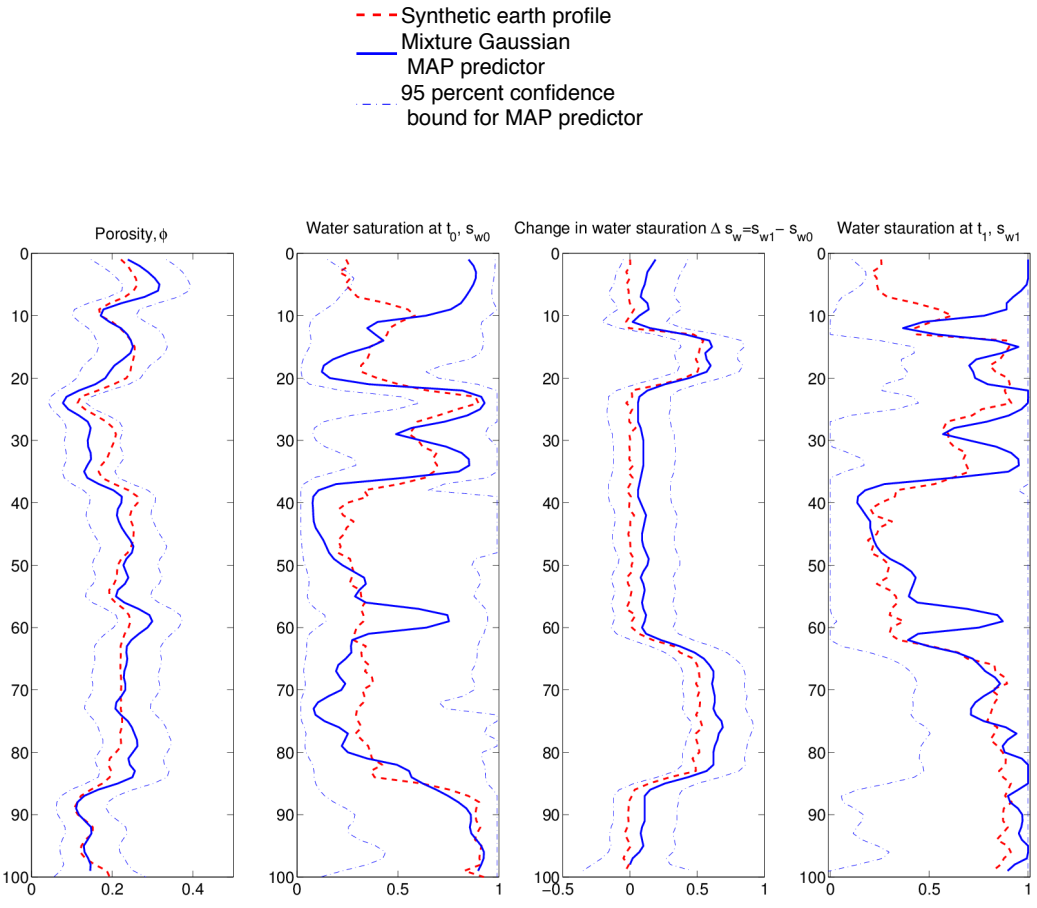

Figure A.27: Synthetic model with SNR=5 and SNR=20 in the inversion model

GENERALIZED GAUSSIAN PRIOR CASE

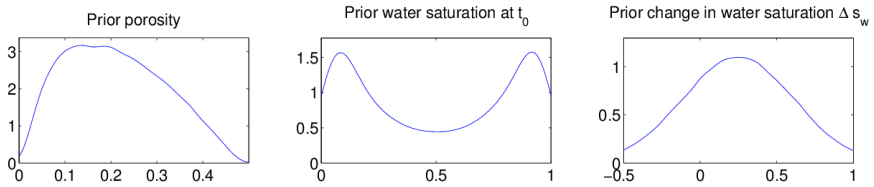

Synthetic earth profile made with SNR=5
Inversion model with SNR=2

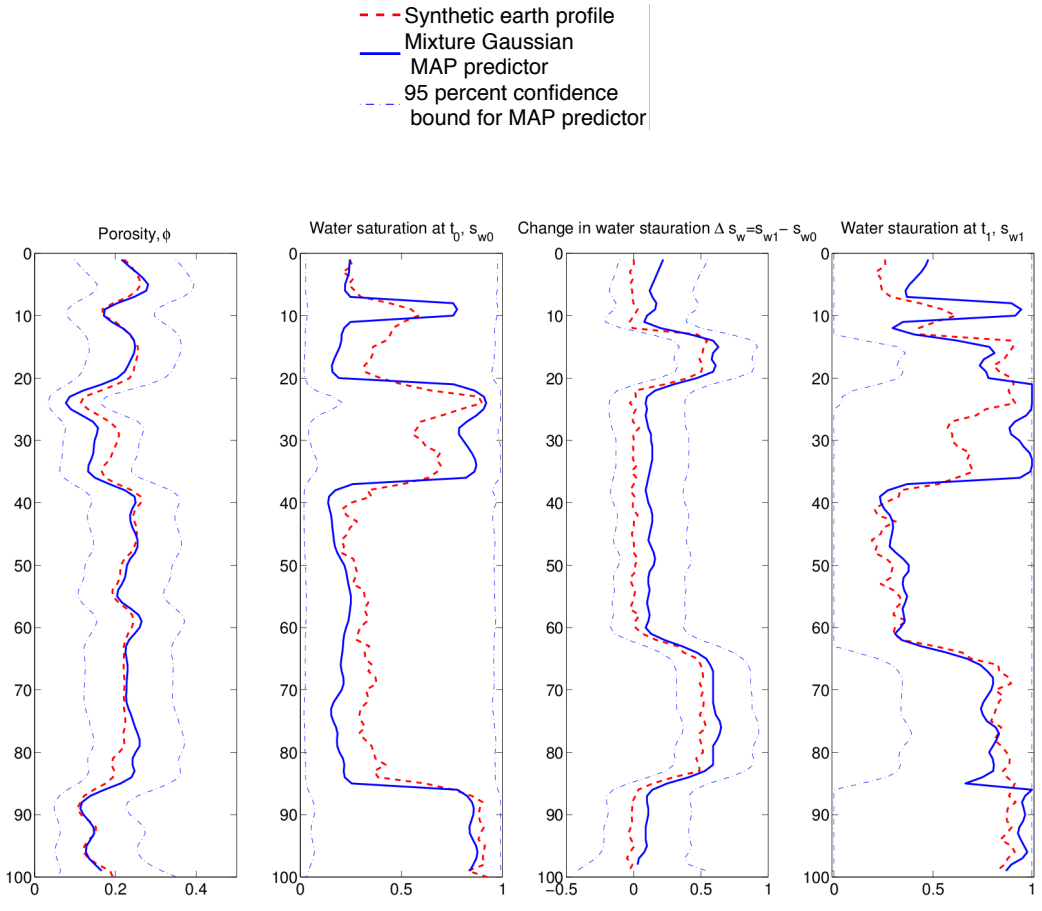

Figure A.28: Synthetic model with SNR=5 and SNR=2 in the inversion model

GENERALIZED GAUSSIAN PRIOR CASE

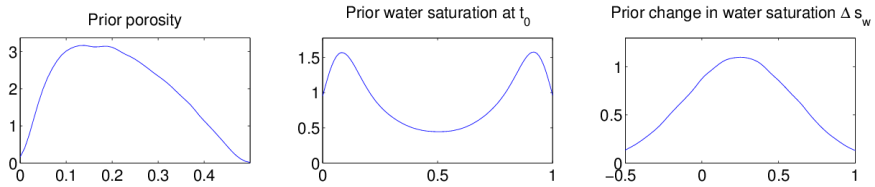

Synthetic earth profile made with SNR=2
Inversion model with SNR=20

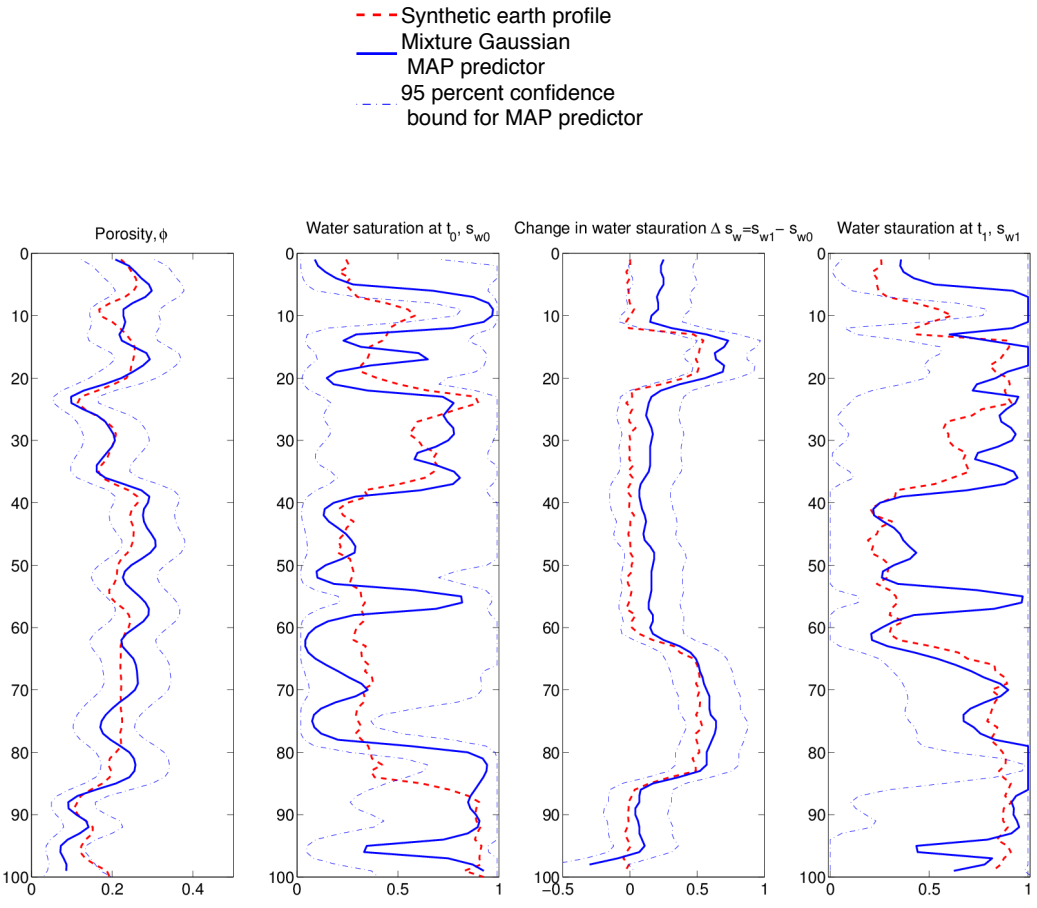

Figure A.29: Synthetic model with SNR=2 and SNR=20 in the inversion model

GENERALIZED GAUSSIAN PRIOR CASE

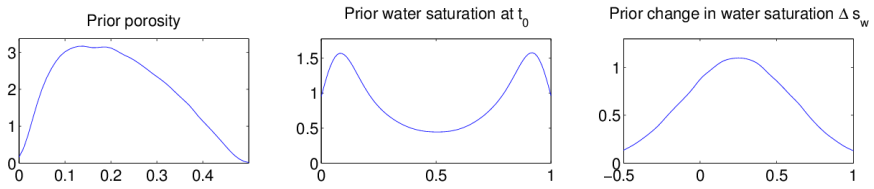

Synthetic earth profile made with SNR=2
Inversion model with SNR=5

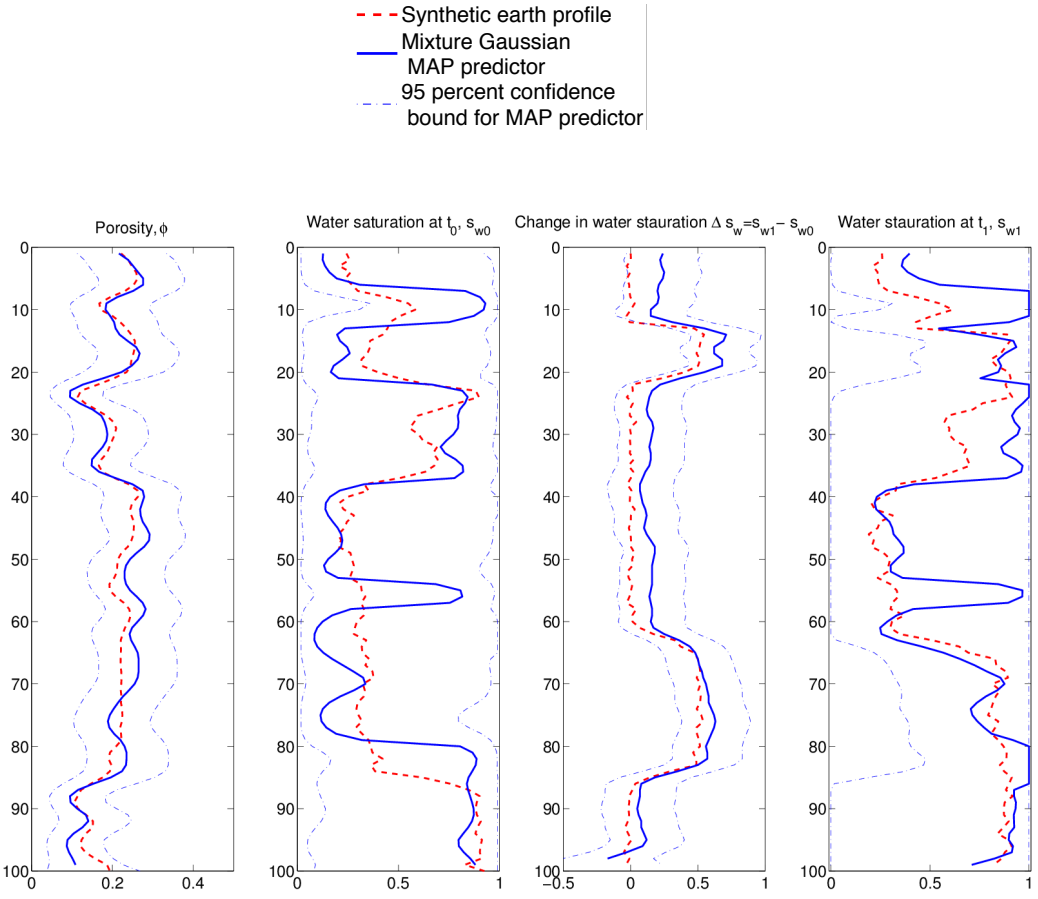

Figure A.30: Synthetic model with SNR=2 and SNR=5 in the inversion model